Dhouha Bouchaala

Investigation of Current Excitation for Personal Health and Biological Tissues Monitoring

Scientific Reports on Measurement and Sensor Technology

Volume 1

Prof. Dr.-Ing. Olfa Kanoun (Editor)

Dhouha Bouchaala

Investigation of Current Excitation for Personal Health and Biological Tissues Monitoring

TECHNISCHE UNIVERSITÄT
CHEMNITZ

Universitätsverlag Chemnitz

2016

Impressum

Bibliographische Information der Deutschen Nationalbibliothek

Die Deutsche Nationalbibliothek verzeichnet diese Publikation in der Deutschen Nationalbibliografie; detaillierte bibliografische Angaben sind im Internet über http://dnb.d-nb.de abrufbar.

Titelgrafik: Chemnitz School of Metrology

Satz/Layout: Dhouha Bouchaala

Technische Universität Chemnitz/Universitätsbibliothek

Universitätsverlag Chemnitz

09107 Chemnitz

http://www.tu-chemnitz.de/ub/univerlag

Herstellung und Auslieferung

Verlagshaus Monsenstein und Vannerdat OHG

Am Hawerkamp 31

48155 Münster

http://www.mv-verlag.de

ISSN 2509−5102 print−ISSN 2509−5110 online

ISBN 978−3−944640−96−9

http://nbn-resolving.de/urn:nbn:de:bsz:ch1-qucosa-204801

Investigation of Current Excitation for Personal Health and Biological Tissues Monitoring

DISSERTATION

zur Erlangung des akademischen Grades

DOKTOR-INGENIEUR
(Dr.-Ing.)

vorgelegt
der Fakultät für Elektrotechnik und Informationstechnik der Technischen Universität Chemnitz

von Dipl.-Ing. Dhouha Bouchaala, MSc
geboren am 05.06.1984 in Sfax, Tunesien

eingereicht am 24.02.2016

Gutachter: Prof.Dr.-Ing. Olfa Kanoun
Prof.Dr.-Ing. Nabil Derbal

Tag der Verleihung: 19.05.2016

Abstract

Bioimpedance spectroscopy is very useful in biomedical field as a safe and non-invasive technique. A stable and safe excitation current below than 0.5 mA for load impedances changing from 100 Ω to 10 kΩ in the full β-dispersion range from kHz up to 1 MHz is a big challenge for the design of the current source addressed by this thesis. For a good stability and high accuracy, the source should have a high output impedance.

Different current source types in "current-mode approach" and "voltage-mode approach" were investigated and compared for usability in bioimpedance measurement systems. The "voltage-mode approach" with grounded load was proven to be more suitable and stable for biomedical measurements. Thereby the Tietze and the Howland circuit in dual configuration with negative feedback have shown the lowest error of the output current and the highest output impedance, where the improved Howland circuit in dual configuration with negative feedback is preferred because it has a simple structure, high accuracy and good stability.

We suggest to improve the stability of the Howland circuit in dual configuration with negative feedback by introducing compensated operational amplifiers and to reduce stray capacitances at higher frequencies by adding gain compensation capacitor. We reach thereby an accuracy of 0.5% at low frequency and 0.9% at 1 MHz. With the realized accuracy of the designed voltage controlled current source, one decisive prerequisite for portable bioimpedance measurement system is achieved.

In order to select the appropriate excitation signals for short measurement time, a comparative study of signals and their parameters was carried out. It leads to the selection of binary chirp signal as a suitable excitation signal due to its short measurement time about 100 μs, low crest factor lower than 2.8 and an energy efficiency higher than 54% in a very noisy signal. Simulation results show that the designed enhanced Howland current source excited by the binary chirp signal has low error and flatness in the whole range.

Kurzfassung

Die Bioimpedanzspektroskopie gewinnt aufgrund ihrer besonderen Eigenschaften als nicht-invasive, schonende Messmethode zunehmend an Bedeutung im biomedizinischen Bereich. Dabei ergeben sich besondere Herausforderungen für den Entwurf der Stromquelle zur Realisierung eines stabilen und sicheren Anregungsstroms. Gefordert ist eine hohe Genauigkeit bis zu einem Maximalstrom von 0.5 mA in einem Frequenzbereich, der der β-Dispersion entspricht, von wenigen kHz bis hin zu 1 MHz. Die Stabilität muss bei variablen Lastimpedanzen im Bereich von 100 Ω bis 10 kΩ gewährleistet sein. Dafür muss die Stromquelle eine hohe Ausgangsimpedanz aufweisen.

Diese Arbeit fokussiert auf den Entwurf von spannungsgesteuerten Stromquellen. Verschiedene Arten von Stromquellen wurden untersucht und verglichen. Der "Voltage-Modus-Ansatz" mit Masse-referenzierter Last hat sich als besser geeignet und stabiler für biomedizinische Messungen erwiesen. Die Tietze-Schaltung und diese Howland-Schaltung zeigen dabei die niedrigsten Fehler des Ausgangsstroms und die höchste Ausgangsimpedanz. Im direkten Vergleich besitzt die verbesserte Howland-Schaltung doch eine einfachere Struktur, höhere Genauigkeit und bessere Stabilität und wird daher gegenüber der Tietze-Schaltung bevorzugt.

Um weitere Stabilitätsverbesserungen bei der Howland-Schaltung zu erreichen, werden zwei Maβnahmen vorgeschlagen. Zum einen werden kompensierte Operationsverstärker eingeführt und zum anderen wird der Einfluss von Streukapazitäten bei hohen Frequenzen minimiert indem die Verstärkung mit Kondensatoren kompensiert wird. Durch diese Maβnahmen wird eine Genauigkeit von 0.5% bei niedrigen Frequenzen und 0.9% bei 1 MHz ermöglicht. Mit dem neuen Entwurf der spannungsgesteuerten Stromquelle ist ein entscheidender Meilenstein für die Realisierung tragbarer Messsysteme der Bioimpedanz erreicht.

Um eine kurze Messzeit zu realisieren wurde eine vergleichende Studie von Anregungssignalen und deren Signalparameter durchgeführt. Die Ergebnisse zeigen, dass binäre Chirp-Signale aufgrund der reduzierten Messzeit, des niedrigen Crest-Faktors unter 2.8 und hohe Energieeffizienz von mehr als 54% bei hohem Rauschlevel

besonders geeignet sind. Simulationsergebnisse zeigen, dass die entwickelte Howland-Stromquelle zusammen mit einem binären Mehrfrequenzsignal den geringsten Amplitudenfehler im gesamten Frequenzbereich realisiert.

Contents

Abbreviations

Z_{out}	Output impedance
Z_{Load}	Load impedance
Z_{tissue}	Tissue's impedance
Z_{meas}	Measured impedance
$Z_{electrode-tissue}$	Electrode-tissue contact impedance
I_{source}	Current source
C_c	Capacitor
r_e	Input resistance
r_i	Output resistance
g_m	Transconductance
V_1	Input voltage
V_2	Output voltage
I_1	Input current
I_2	Output current
I_{Load}	Load current
$I_{Load\,min}$	Minimum load current
$I_{Load\,max}$	Maximum load current
I_{out}	Output current
I_{max}	Perception threshold
$Z_{Load\,min}$	Minimum load impedance
$Z_{Load\,\max}$	Maximum load impedance
V_{in+}, V_{in-}	Differential input voltage
ϵ	Error
I_{bias}	Input bias current
V_{off}	Input offset voltage
I_{off}	Input offset current
OTA	Operational Transconductance Amplifier
$CCII$	Current conveyor second generation

CCI	Current conveyor first generation
$VCCS$	Voltage controlled current source
ISC	Inverting single configuration
$NISC$	Non-inverting single configuration
IDC	Inverting dual configuration
$NIDC$	Non-inverting dual configuration
$DCNF$	Dual configuration with negative feedback
SNR	Signal to Noise Ratio
BIS	Bio-impedance Spectroscopy
CF	Crest Factor
TF	Time Factor
TUT	Tissue Under Test
E	Total Energy
P_{avg}	Average Power
PSD	Power Spectral Density
δ_E	Energy Efficiency
N	Number of Samples
F_s	Sampling Rate
ADC	Analog to Digital Converter
M	Number of Cycles
MLS	Maximum Length Sequence

In loving memory of my father

Habib Bouchaala

(1954-2010)

My role model, my inspiration and my motivation

My mother
Naourez

No words are sufficient to describe her sacrifices.
Her unconditional support and encouragement impelled me
to set high goals and the confidence to achieve them.

My sister and my brother
Olfa & Houcine

Thanks for understanding, supporting me all along
and always being by my side.

Dhouha Bouchaala

Acknowledgements

The work presented in this dissertation was carried out in the chair for Measurement and Sensor Technology (MST) at Chemnitz University of Technology.

First and foremost I would like to express my special appreciation and thanks to my supervisor, Professor Olfa Kanoun at Chemnitz University of Technology, Germany. I am really appreciating all her contributions of time, support, encouragement and invaluable guidance to make my Ph.D.

I would like to express my deep gratitude to my supervisor, Professor Nabil Derbel at National Engineering School of Sfax, Tunisia for his generous support and consistent kindness throughout the course of the work.

I would like to thank all my colleagues in the impedance spectroscopy working group at MST, especially Dr. Qinghai Shi, Paul Büschel, Thomas Günther and Frank Wendler for many fruitful discussions. Thanks are extended to Sonia Bradai and all colleagues at MST for their kind support during my part time work there and joyful time that we shared together.

I would like to extend my heartfelt appreciation to Ahmed Fendri, Xingue Chen, Abdelaziz Abbasi, Emna Mekki, Syrine Fellah and Ashish Shrivastava who have helped and supported me while I have been working on this project.

Very special thanks go to my best friends for their continous help and advice along the way.

Financial supports from DAAD and within the exchange program InProTUC are gratefully acknowledged.

Dhouha Bouchaala

1. Introduction

1.1 Motivation

Non-invasive regular patient monitoring in clinical and home environment presents a high interest of medicine today. Among many non-invasive techniques such as X-ray, ultrasound, magnetic resonance imaging (MRI), electrical impedance spectroscopy is gaining importance in the medical field. It performs real-time measurement and it is suitable for long time observation. This technique relies on measurements of the complex impedance over a certain frequency range. By a physical or mathematical modeling, information about biological tissues can be extracted in form of parameters or state parameters (Figure 1.1).

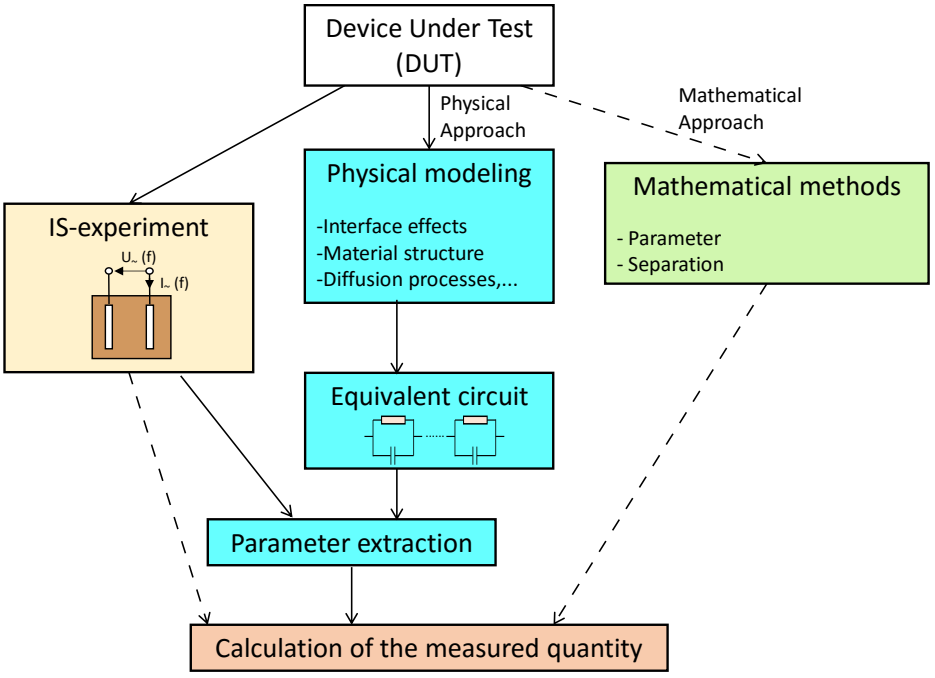

FIGURE 1.1: Impedance spectroscopy flow chart [1]

Generally, impedance measurement devices, such as impedance analyzers and LCR meter are used to perform the measurement. They are performant but they are bulky, not flexible for clinical environment and relatively expensive. To follow regularly the patient's health state and enhance the emergency of medical care,

healthcare organizations are increasing their reliance on mobile medical devices for non-invasive personal health and biological tissues monitoring.

The benefits from impedance measurements in medicine and biology are obviously significant. New applications are continuously under investigation and development. Over the last years, interesting new instruments have been introduced in several medical applications like body composition analysis, implantable pace maker [2], tissue diagnostic [3], wearable computing [4], ECG monitoring [5], ischemia [6], lung edema [7], skin cancer [8] and intramuscular tumor [9].

For medical research and health care, the portable patient monitoring system requires broadband accurate diagnosis and fast measurement, low energy consumption and low cost. The requirements for portable biomedical device are related directly to the requirements for excitation signals. Hence, the accuracy and compliance of the excitation current can greatly affect the quality and performance of the measurement results and also the safety of patients, since it is the source of all calculations.

The focus of this thesis is the design of a high accurate and wideband excitation subsystem for bioimpedance measurements, which fulfills both requirements for an accurate measurement for a big range of applications in the biomedical field and the requirements of patient safety.

1.2 Problem statement

In bioimpedance measurement system, the excitation subsystem includes in general the signal generation and a signal source. Because of patient safety, it is preferable that the generated signal is a voltage forwarded to a voltage controlled current source. Current sources are critical for the performance of bioimpedance health monitoring devices and should fulfill both technical and medical requirements. For wide use, a high accuracy and wide bandwidth is required. Their output should be stable and within safe current magnitudes.

To keep the output current stable over the working frequency range independently of load changes, the output impedance Z_{out} should be maintained much higher (> 1000) than the load impedance Z_{Load}, so that the major part of the current is given to the output and the inner losses of the source are reduced.

The load impedance does not consist only of the measured tissue but also of electrodes impedances and contact effects. Corresponding to the typical measurement requirements, it should allow load impedances in the range from 100 Ω to 10 kΩ and have high output impedance of approximately 10 MΩ at 5 kHz and 1 MΩ at high frequencies up to 1 MHz without harmonics and influence of stray capacitances. The majority of voltage controlled current sources studied in literature does not fulfill the target output impedance's requirements.

The aim of this study is to design a stable voltage controlled current source (VCCS) with a high output impedance in the relevant frequency and impedance range for bioimpedance measurement. By studying the complex impedance of biological tissues as provided in section 2.3, the relevant frequency range is from kHz to MHz and the load impedance Z_{Load} can be between 100 Ω and 10 kΩ. The output impedance Z_{out} should be 10 MΩ at 5 kHz and 1 MΩ at 1 MHz as will be explained in chapter 2.

For that, different structures of voltage controlled current source need to be investigated with the option to provide a novel design including both a suitable structure and a suitable configuration of its elements.

The classical approach consists of exciting the voltage controlled current source with a series of single sine measurements over the frequency range of interest. It has a high energy efficiency and high accuracy but it demands a long measurement time. This is why, in a first phase, the designed voltage controlled current source is excited by the sine wave signal. In the second phase, different periodic excitation signals are classified and optimized based on a comparative study of the energy efficiency, the power spectral density and the crest factor with and without noise. The aim is to choose a suitable excitation signal having high energy efficiency, real time response and a simple generation.

1.3 Thesis overview

The thesis is structured in five chapters (Figure 1.2). In chapter 2, the biological tissue monitoring procedure is described using impedance spectroscopy and the specifications of bioimpedance measurement systems are expounded. Especially, the requirements for the current source are analyzed.

In chapter 3, a literature review of voltage controlled current sources in current-mode and voltage-mode approaches are presented, classified and explained. They are analyzed and compared b their output impedance and usability for bioimpedance measurement devices.

Chapter 4 focuses on VCCS in voltage-mode approach especially for grounded loads. For this, different variations of Tietze and Howland topologies are described and compared considering their output current and output impedance in order to choose the suitable configuration. The chosen configurations are simulated in order to define the suitable circuit element values and to analyze their influence.

In chapter 5, in pursuance of improving the stability of the output current at high frequencies up to 1 MHz, methods eliminating the influence of stray capacitances are expounded and the external compensation is proposed. Experimental investigations are carried out and results concerning voltage controlled current source are discussed.

In chapter 6, the selection of the suitable excitation signal is described for a portable impedance measurement system. It is based on the simulations of the signal while respecting the constraints of the system and ensuring the safety of the patient.

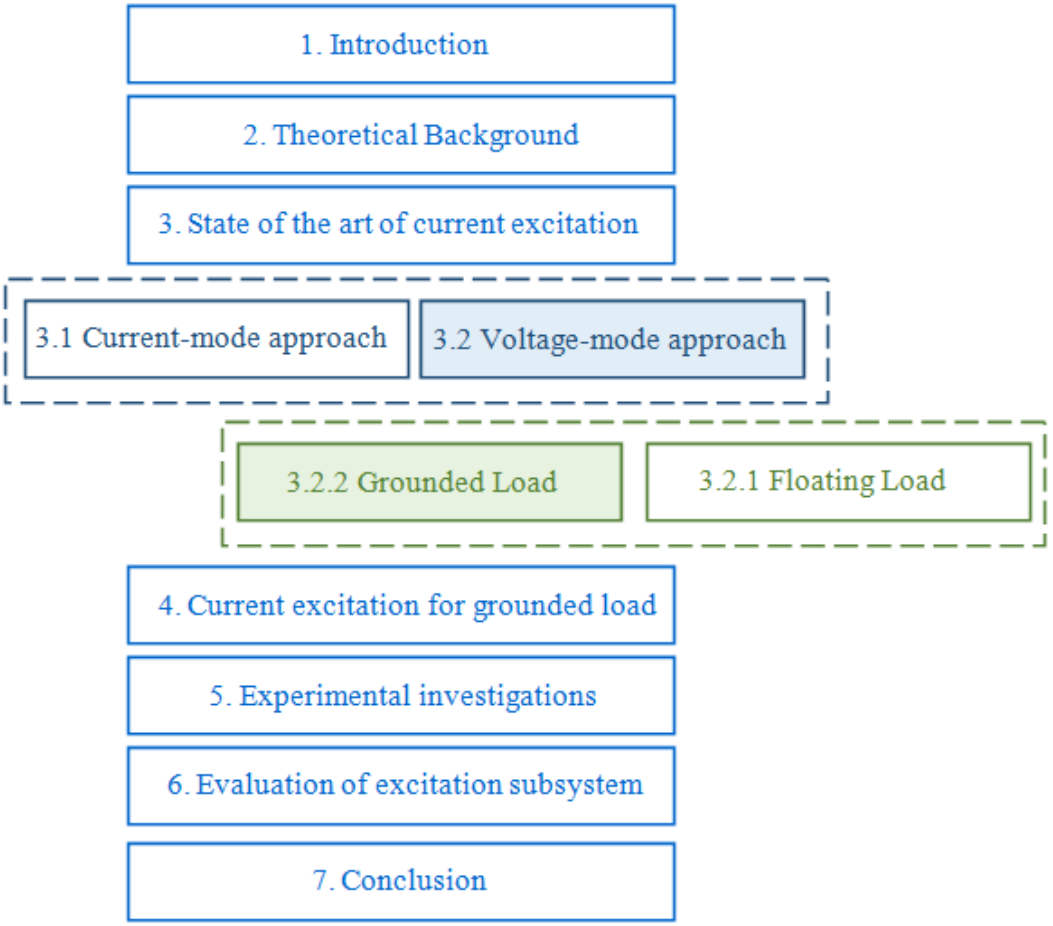

FIGURE 1.2: Thesis overview

2. Theoretical background

In clinical environments, invasive and non-invasive techniques e.g. nuclear magnetic resonance and X-ray measurements are often used for diseases detection. These techniques need a complex hardware with high costs, but are very accurate and useful [10]. Hence, they are not suitable for real time patient monitoring, where the state of the patient should be continuously monitored over a long time to pursue the development of a disease or the reaction on a certain treatment. A subject of interest of several researchers in the medical field is therefore the online pathological tissues states monitoring and real time data analysis using portable devices. Several studies have been conducted on the potential of electrical bioimpedance spectroscopy [8] [9]. This technique is non-invasive, cost efficient,easy to realize as a portable device and allows long-term measurements.
This chapter is an overview of the specifications of a portable device based on impedance spectroscopy given with emphasis on the excitation subsystem for personal health and biological tissues monitoring.

2.1 Biological tissues monitoring using impedance spectroscopy

Impedance spectroscopy is an effective method for biological tissues monitoring. It is based on the injection of an AC electrical signal with constant amplitude on the tissue under test by electrodes and the measurement of its impedance at different frequencies [11].

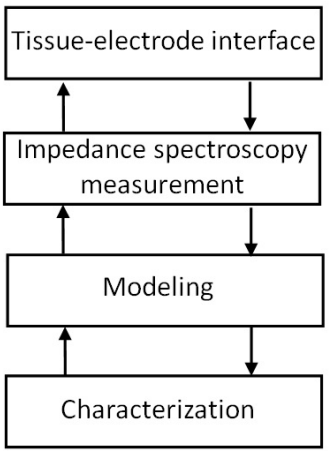

FIGURE 2.1: Flow diagram of biological tissues monitoring based on impedance spectroscopy

The measured impedances in the frequency range of interest are modeled by equivalent circuits in order to characterize the state of biological tissue under test (Figure 2.1). In the following sections, the four basic steps of biological tissues monitoring are explained.

2.1.1 Tissue-electrode interface

For bioimpedance measurements, the biological tissue is excited and the difference of potential is measured. In general, systems can use two electrodes (bipolar) or four electrodes (tetrapolar). In case of bipolar electrodes, the injected signal and the sensed signal use the same electrodes. In this case, the measured impedance $\underline{Z}_{meas}$ is the combination of the biological tissue's impedance $\underline{Z}_{tissue}$ and the impedance of cables and electrodes-tissue contact impedance defined as $\underline{Z}_{electrode-tissue}$ (Figure 2.2). Hence, the measured impedance is not accurately measured and includes a bias impedance.

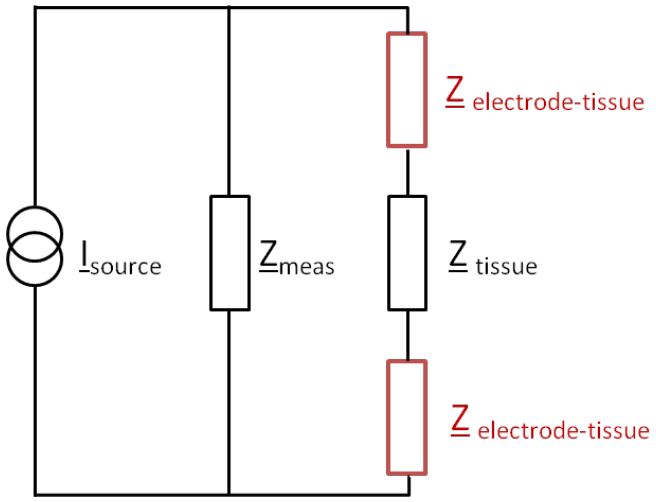

FIGURE 2.2: Bipolar electrode configuration [9]

To avoid the undesirable bias impedance, a four-electrode method can be used especially when measuring low impedance Tissues Under Test (TUT) [12] [13]. For this method, an excitation signal is injected via two electrodes and the dropped signal is measured via two other electrodes.

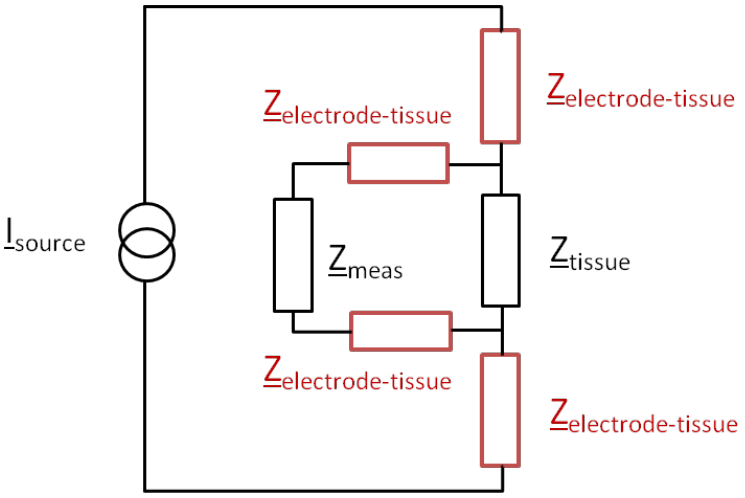

FIGURE 2.3: Tetrapolar electrodes configuration [9]

The measured signal is not including the electrode-tissue impedance and the cable impedance because of a high ohmic input of the measurement device. Even if these impedances are existing; they don't influence the measurement, because the flowing current to the measurement device is almost zero (Figure 2.3).

This is why; most impedance measurements for biological tissues use the four-electrode method that overcomes the influence of the additional impedance between electrodes and tissues [14]. However, the four-electrode method is not enough accurate especially at high frequency in the presence of parasitic impedances [15].

2.1.2 Impedance spectroscopy measurement

For the impedance measurement, there are basic techniques such as the bridge method [16], the analog and digital quadrature demodulation method [15] [17] and the magnitude ratio and phase difference detection. The bridge method and the quadrature demodulation method are not suitable for the design of portable bioimpedance spectrometer because of high costs, time requirements and power consumption. The magnitude ratio and phase difference detection [18] is the most used technique for impedance measurement because of its rapidity in measurement and simplicity in the design.

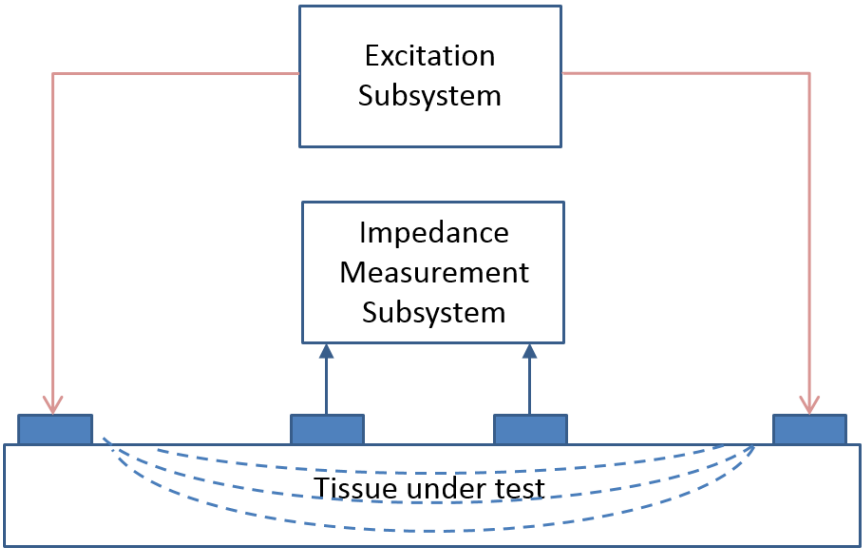

FIGURE 2.4: Block diagram of biomedical measurement system using four-electrode method [19]

By measuring the magnitude and phase of a biological tissue (Figure 2.4),bioimpedance spectroscopy method retrieves information regarding the electrical properties of tissues and organs [20].

2.1.3 Modeling

The impedance spectrum includes information about the electrical properties of biological tissue in the frequency range of interest [21]. At low frequencies, the impedance of the biological tissue is almost resistive equal to the impedance of the extracellular fluid because the injected signal flows only through it. Whilst at high frequencies, the impedance of the biological tissue is decreasing because the injected signal flows in both extracellular and intracellular fluids [22]. Therefore, the impedance spectrum can be converted to an equivalent circuit to extract the indicator parameters for the tissue condition.

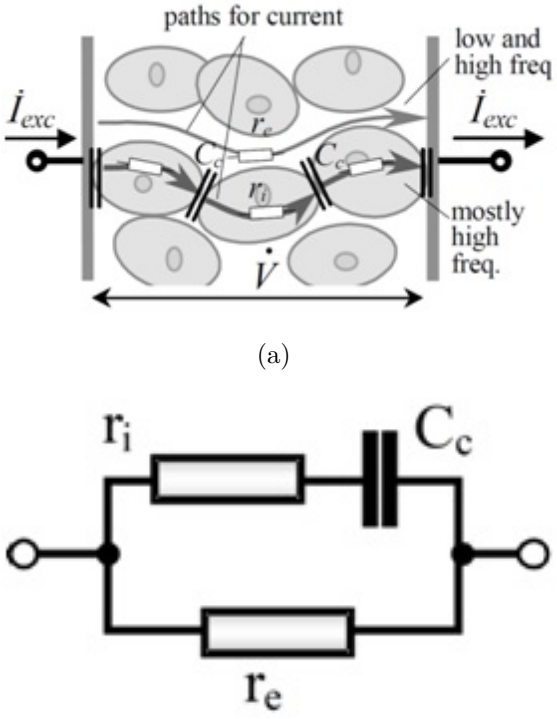

FIGURE 2.5: Tissue modeled as basic electronic circuit [23]

The cell's membrane, extracellular and intracellular fluids are represented respectively by a capacitor C_c, resistors r_e and r_i (Figure 2.5). Hence, variations of these parameters lead to the survey of the state of tissue under test and the monitoring of its pathological condition.

2.1.4 Characterization

Bioimpedance spectroscopy can be used for characterization for the whole body or for biological tissues. For the whole body, different aspects can be characterized, where the body fat analysis is the most known application. The principle is implemented today in the classical balances, where the impedance of the body is measured via electrodes at the feet. The bioimpedance is generally measured in this case at a frequency of 50 kHz. The evaluation of the body fat content estimated by the body mass index (BMI) which is carried out by means of statistic formulas 2.1 and 2.2.

$$Child\,body\,fat\,\% = (1.51 \times BMI) - (0.70 \times Age) - (3.6 \times sex) + 1.4 \qquad (2.1)$$

$$Adult\,body\,fat\,\% = (1.20 \times BMI) + (0.23 \times Age) - (10.8 \times sex) - 5.4 \qquad (2.2)$$

From a big number of applications of whole body bioimpedance, we can mention the bioimpedance cardiography where the electrical properties of the thorax are monitored via its impedance variations [24].

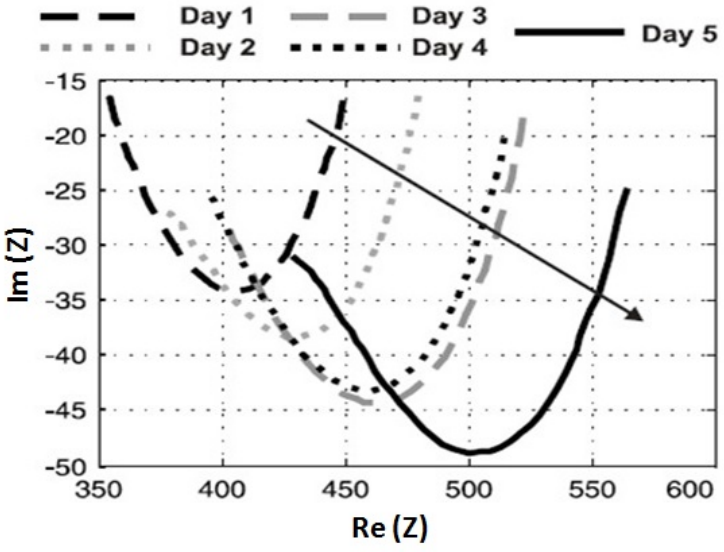

FIGURE 2.6: Whole body impedance plot of patient during the course of five days [25]

Beckman presented in [25] some measurements on the patient's whole body impedance during five days and collected a database to facilitate the monitoring of the state of the patient suffering from lung edema. This disease causes a body weight loss. For that, the body weight is monitored by the measurement of the whole body impedance (Figure 2.6). In the first day, the small impedance around 400 Ω points out the presence of a large amount of water in the body. Figure 2.6 shows the increase of the impedance within the measurement's duration of five days. This is a sign of water losses in the body which implies that the patient losses weight.

At tissue level, bioimpedance enables to analyze physiological variations. These can provide information about the general state of a muscle and also characterize some diseases like tumors, meningitis and brain cellular edema. Researchers conducted EIS studies in vivo for human tissues such as in bladder, stomach, and breast [26]. The impedance's variation of a biological tissue in normal or cancerous state at low or high frequencies is the diagnosis key point. Therefore, in order to detect any disease in an early phase and diagnose it, a database of the impedance spectra of normal and pathological tissues is required.

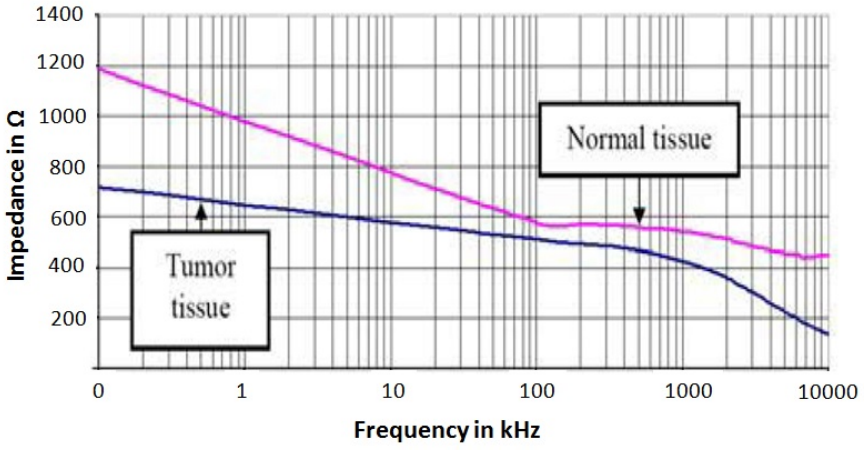

FIGURE 2.7: Impedance amplitude in breast tissue sample [27]

Marinova showed in [27] showed that the impedance variation between normal and tumor tissues has high values from 1 kHz to 100 kHz at low frequencies and from 1 MHz to 10 MHz at high frequencies (Figure 2.7).

2.2 Systems specifications for bioimpedance measurement

Impedance spectra are generally measured using a certain excitation signal's amplitude, a working frequency range and an approximate impedance range. These parameters should be in general defined in a suitable way to fulfill the requirements for impedance measurement as linear system identification method and to ensure the patient safety for application in medical sector.

The aim of this section is to define the general specifications for system design of a bioimpedance spectrometer which can be used for a big range of scenarios and applications in bioimpedance field. The focus thereby is the most physiological effects related to cell membranes and tissue properties.

2.2.1 Frequency range

For biological systems, dispersions can be classified from low to high frequencies to three categories which are α, β, and γ. The α-dispersion, from mHz to kHz, infers to ionic diffusion processes at site of cellular membrane.

TABLE 2.1: Electrical dispersions of biological matter [28]

Contributing biomaterial element		Dispersions		
		α	β	γ
Water & electrolytes				x
Biological macromolecules	Amino acids		x	x
	Proteins		x	x
	Nucleic acid	x	x	x
Vesicles	Surface charged	x	x	
	Non-surface charged		x	
Cells with membrane	Fluids free of protein		x	
	Tubular system	x	x	
	Surface charge	x	x	
	Membrane relaxation	x	x	
	Organelles		x	x
	Protein		x	x

The β-dispersion, from kHz to MHz, is associated with polarization of cellular membranes. The γ-dispersion, up to GHz, infers to polarization of water molecules within the biological tissues [28].

Table 2.1 shows that the β-dispersion includes most of physiological variables in the biological tissues. Within this dispersion, the pathological states can be controlled by the high impedance variations [20]. Therefore, for investigation of tissue's electrical properties and separation of different effects in the impedance spectrum, the typically used frequency range is from 5 kHz up to 1 MHz corresponding to the β-dispersion [29] [30].

2.2.2 Impedance range

Impedance range is in general changing dependently on the tissue's type and tissue state. Table 2.2 shows different impedance ranges. According to [31], the high frequency impedance of the skin at 1 MHz varies from 100 Ω to 400 Ω, whereas low-frequency impedance at 5 kHz varies from 5 kΩ to 10 kΩ. In this case, the impedance is decreasing when the frequency is increasing.

Breast tissue [27] impedance is in normal state higher than its impedance in cancerous state. The impedance range of normal tissue from 1 kHz to 1 MHz is between 1 kΩ and 580 Ω. Whereas the impedance range of a cancerous tissue is between 610 Ω and 400 Ω. The impedance variation is of a great importance in low frequencies from 1 kHz to 10 kHz.

For the whole body and thoracic impedance measurement, Beckmann showed in [25] that from the first to fifth day, the impedance is increasing in both low frequencies at 10 kHz and high frequencies at 1 MHz. Thoracic impedance remains a special case and is hard to monitor because the impedance variation is too small about 5 Ω. Rigaud presented in [32] the impedance of different biological tissues from low frequencies to high frequencies is decreasing from 720 Ω to 100 Ω.

In a nutshell, the impedance range of different biological tissues is changing from 10 kΩ to 100 Ω when increasing the frequency from 1 kHz to 1 MHz.

TABLE 2.2: Impedance range of different biological tissues

Reference	Tissue type	Impedance (Ω)			
		1 kHz	10 kHz	100 kHz	1 MHz
Rosell	Skin	5 000 - 10 000	800 - 5 000	200 - 900	100 - 400
Marinova	Breast (Normal)	1 000	800	600	580
	Breast (Cancerous)	610	595	580	400
Rigaud	Liver	530	480	380	210
	Lung	400	350	280	200
	Spleen	600	550	480	280
	Intestine	120	110	100	100
	Muscle I	390	350	200	120
	Muscle II	720	600	300	120
Beckmann	Whole body (Day 1)		450		350
	Whole body (Day 5)		572		431
	Thoracic (Day 1)		33		22
	Thoracic (Day 5)		38		25

2.2.3 Excitation signal's amplitude range

The excitation signal for biological tissues could be in general a voltage or current. With regard to patient safety, it is preferable to avoid the influence of voltage source degradation, contact impedance between the electrode and the tissue [33] and high currents through the tissue due to the temperature-dependence of tissue electrical conductivity [34]. Therefore, the injection of a current is preferred in biomedical applications. Specifically, the injection of an alternating current (AC) is safer than a direct current (DC), due to the heterogeneous aspect including resistive and capacitive elements of the biological tissue.

The magnitude of the AC-current should be well selected because of system linearity and because it is one of factors that are related to the danger of electrical shock. At low frequencies at 5 kHz, between 0.1 and 0.5 mA, no influence on the human body is detected, independent of the duration of the current flow.
From 0.5 mA to 500 mA, currents are progressively quite painful and can result in muscular contractions and difficulties in breathing. Up to 1 A, currents can lead to cardiac arrest and severe burns [35].

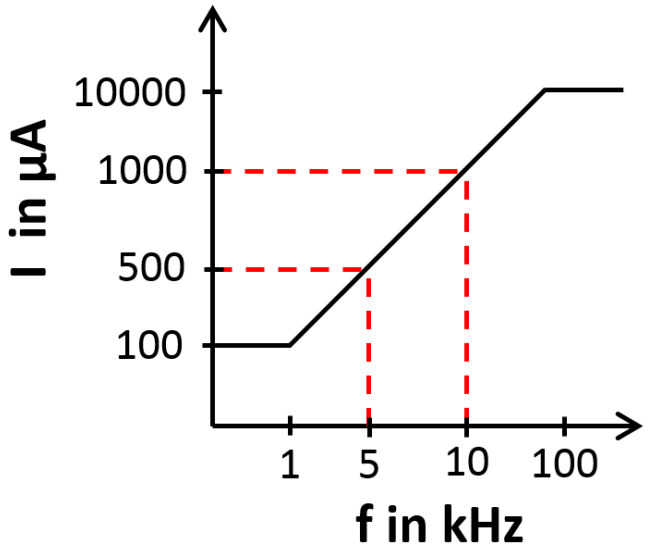

FIGURE 2.8: Permissible current through extracted body from standard EN60601

To avoid harmful risks (burning tissue, freezing muscles, fibrillating heart and cardiac arrest) and maintain the medical requirements, the current should be below the perception threshold (0.5 mA) at 5 kHz [33] imposed by the standard EN-60601 (Figure 2.8). The perception threshold increases when the frequency increases following the equation 2.3 where the current is in rms value and the frequency in Hz [34] [36].

$$I_{max} = 10^{-7} f \tag{2.3}$$

2.3 Current excitation subsystem requirements

The accuracy and compliance of the excitation subsystem can significantly affect the quality of the measurement results and also the safety of patients, since it is the

basis for measurement and signal processing. Ensuring the safety of patients makes the choice of safe current excitation over a wide-band frequency range especially critical. Therefore, it is essential to have awareness of the excitation subsystem's design of the bioimpedance health monitoring device.

For patient safety, it is preferable that the output signal is delivered to biological tissue by a current source, which fulfills both technical and safety requirements. Therefore, the excitation subsystem consists of the generation of the excitation signal and a voltage controlled current source, in the case of a current excitation.

2.3.1 Quality factors of excitation signals

For the generation of an excitation signal, the selection of the excitation is an important phase in the design of portable biomedical measurement system given the fact that a suitable signal enables better data collection within a given time frame. The low crest factor, short measurement time, low average power and high energy efficiency are the requirements for the design of a wearable bioimpedance spectroscopy device.

There are various excitation signals that can be applied in the EIS measurement; each one has its own features in the time and frequency domain. In order to select the appropriate signal that fits the given application, different signal quality metrics are used. The most important parameters in time domain are the crest factor (CF) and the time factor (TF). Gibbs phenomenon, spectral leakage and Picket Hence effect, should be also considered.

2.3.1.1 Crest Factor

The crest factor of an excitation signal u(t) is defined as the ratio of the pick value of the signal to its Effective Root Mean Square value (RMSe) in the frequency band of interest [37] given by the equation 2.4.

$$CF(u(t)) = \frac{U_{peak}}{U_{RMSe}} = \frac{t \in [0,T] max \mid u(t) \mid}{\sqrt{\frac{1}{T}\int_0^T u^2(t)\frac{P_i}{P_T}}} \tag{2.4}$$

T denotes the measurement time, P_i is the power focused on the frequency band of interest and P_T is the total power of the excitation signal u.

This metric reflects the compactness of the signal and measures how much power is injected into the system under test. Low crest factor is required to provide more energy injection resulting in maximal SNR with keeping limited excitation amplitude, necessary to maintain the linear behaviour of the system under test.

2.3.1.2 Time Factor

The time factor of the signal is defined as the ratio of the relative measurement time to the frequency line (equation 2.5).

$$Tf(u) = \frac{T}{F} = max\, 0.5\, Cr^2(u(t)) \frac{U^2_{RMSE}}{|U(k)|^2} \tag{2.5}$$

Where: T is the required measurement time and U_{RMSe} is the Effective Root Mean Square value and defined as show in equation 2.6.

$$U^2_{RMSE} = \sum_{k=1}^{F} \frac{|U(k)|^2}{F} \tag{2.6}$$

$k \in F$ with F is the number of frequencies in frequency band of interest

It describes the signal's power distribution over the frequencies [38] and shows the required time per frequency line necessary to achieve maximal SNR. Hence, this factor should be maintained as low as possible.

2.3.1.3 Gibbs phenomenon

The Gibbs phenomenon occurs by approximating discontinuous functions with a partial finite number of terms from Fourier series. It is detected when the n^{th} component of Fourier series has large oscillation results in an overshoot. This phenomenon is mainly illustrated in periodic waves [39].

2.3.1.4 Spectral leakage

One of the most Fast Fourier Transform algorithm limitations is the leakage effect, which occurs if the time record of the periodic signal is a non-integer number of cycles or if aperiodic signals are considered, as it produces discontinuities at the end of the measurement time. This phenomenon leads to loss of energy of the desired signal component in addition to the difficulties of the detection of the signal behavior [40].

There are two solutions to be taken into consideration to reduce this issue. One of them is averaging a high number of measurement times. The other one consists on applying appropriate windowing functions [41].

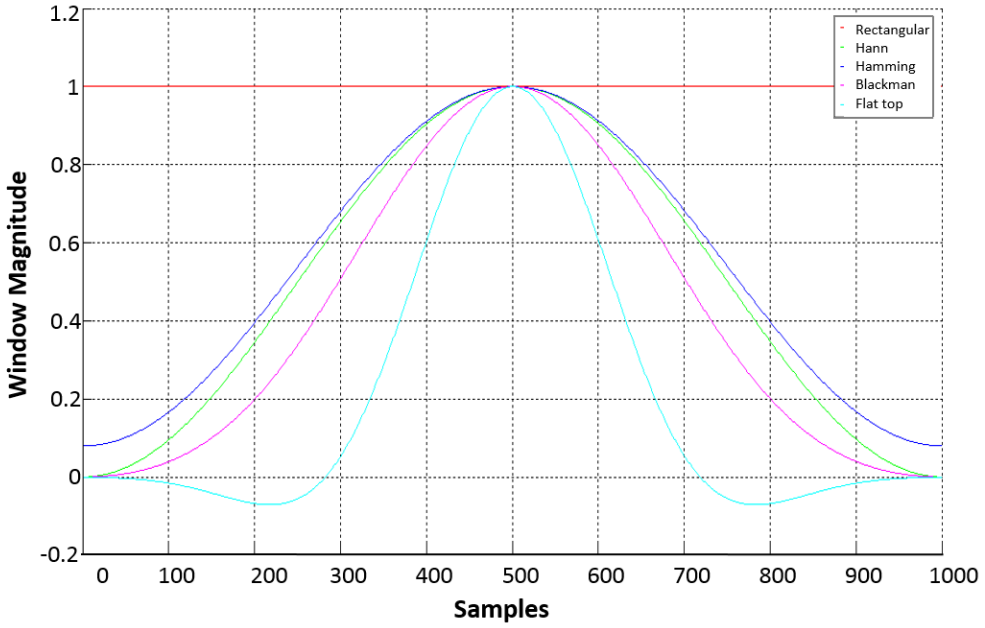

FIGURE 2.9: Shapes of different windows

Figure 2.9 presents comparative plots of frequently used window functions (rectangular, Hann, Hamming, Blackman, flat top windows) having the same length (e.g. 1000 samples).

Figure 2.10 shows the effect of applying these window functions on the sine signal.

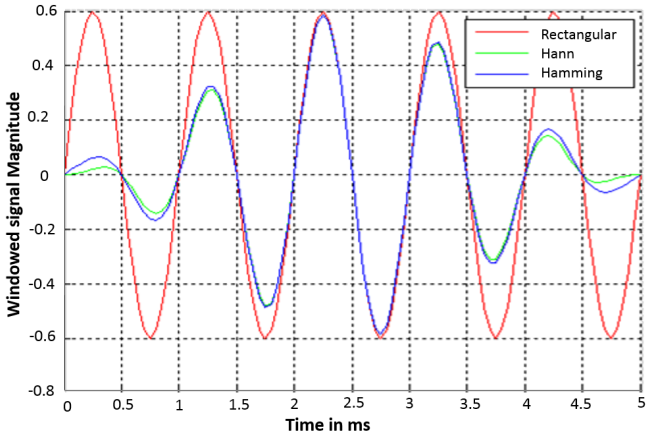

(a)

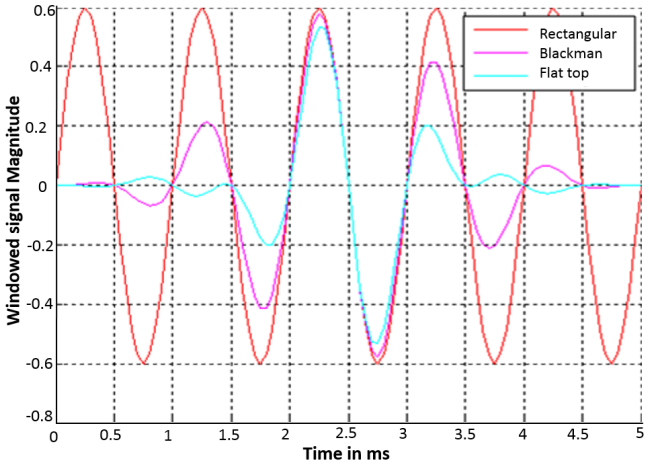

(b)

FIGURE 2.10: Effects of different window functions on the sine signal: (a)Hann and Hamming windows (b)Blackman and flat top windows

2.3.1.5 Picket Hence effect

The Discrete Fourier Transform spectrum represents the spectral level in each discrete frequencies component. The spectrum of the analyzed signal may contain peaks that do not correspond to the represented frequencies. This phenomenon is called picket hence effect. To minimize this problem, an increase of the spectrum's resolution is recommended. For this purpose, zero padding technique (Figure 2.11) is used to increase the measurement time synthetically and increase frequency resolution [42].

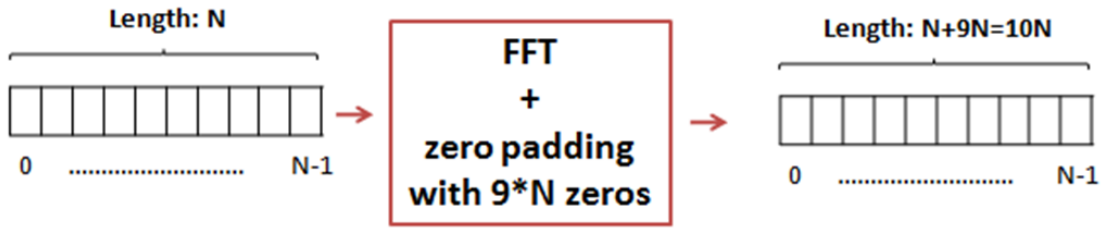

FIGURE 2.11: Length of the sequence before and after applying the zero padding technique

2.3.1.6 Signal to noise ratio (SNR)

In order to describe the quality of a signal and to evaluate the sensitivity of the measurement process to disturbing noise, the signal to noise ratio is defined as the ratio of signal power to the noise power (equation 2.7)

$$SNR = 10\,log(\frac{P_{signal}}{P_{noise}}) \tag{2.7}$$

2.3.1.7 Sources of noise

Noise is unwanted and disruptive signals that occur during the measurement process which may results in a poor accuracy of measurement. Many classes of noise exist and they vary from a system to another. In bio-impedance spectroscopy devices we can classify noise to two types: the first one is caused by noise coming from electronic system and the second is due to ADC quantization.

• Electronic noise: Numerous electronics noise can appear in the circuit. The most known one is the thermal noise called Johnson noise caused by any resistor set at non-zero temperature. It is characterized by a white power density spectrum and its voltage noise is defined by equation 2.8.

$$V_n = \sqrt{4KTBR} \tag{2.8}$$

Where R is the resistance, K is the Boltzman constant, B denotes the bandwidth and T is the temperature.

In addition, a crosstalk from channel of transmission power can greatly distort the impedance signal [43]. Moreover, the external disturbances and deterioration of the behavior of electronic circuit can be considered as one factor of the malfunction of the measurement system [44].

• Quantization noise: The ADC noise is considered as an important limitation source when broadband signal is digitized using a b-bit A/D. In this case, the SNR is given by equation 2.9.

$$SNR = 6.02b + 1.67 - 20log_{10}(\frac{CF}{\sqrt{2}}) \tag{2.9}$$

In addition to that, the instability of the sampling clock can be introduced when conversion from analogue to digital data or inversely is occurred. This leads to produce jitter noise which follows a Gaussian distribution. The SNR based only on jitter is given by equation 2.10.

$$SNR = 20\,log_{10}(2\pi f t_{jitter}) \tag{2.10}$$

2.3.1.8 Energy efficiency

The total energy of the signal dissipated over 1 $k\Omega$ resistor is given by equation 2.11.

$$E = \lim_{T\to\infty} \int_{-T}^{T} |x(t)|^2\,dt \tag{2.11}$$

The time average power of a signal dissipated over 1 $k\Omega$ resistor is defined by equation 2.12.

$$P = \lim_{T\to\infty} \frac{1}{2T} \int_{-T}^{T} |x(t)|^2\,dt \tag{2.12}$$

The energy efficiency δ_E [45] is defined as the ratio of the energy focused on the desired bandwidth Bexc to the total bandwidth (eqation 2.13).

$$\delta_E = \frac{E_{exc}}{E_{tot}} \tag{2.13}$$

Where:

E_{exc} and E_{tot} are respectively the energy concentrated in the desired frequency range and the total energy.

In general the energy efficiency [46] can be developed from the results of FFT-processing as shown in equation 2.14.

$$\delta_E = \frac{\sum_{i=N0}^{Nfin} |X(f_i)|^2}{\sum_{i=N0}^{Nmax^{-1}} |X(f_i)|^2} \tag{2.14}$$

where $|X(f_i)|$ is the value of the magnitude spectrum at the i^{th} frequency bin, N0 and Nfin are the numbers of frequency bins, corresponding respectively to the initial frequency f_0 and the last frequency f_{fin} , and N_{max} is the total number of frequency bins.

2.3.1.9 Power spectral density

To describe the behavior of input signal in frequency domain, a plot of its power spectral density (PSD) is suggested. This latter can be developed in two ways:

$*$ The power spectral density (PSD) of a voltage signal associated with 1 Ω resistance is mathematically related to the autocorrelation function by the Fourier transforms expressed in [47] by equation 2.15.

$$S_x(f) = \int_{-\infty}^{\infty} R_x(\tau) e^{-i2\pi f\tau}\, d\tau \tag{2.15}$$

The autocorrelation function can be derived from the PSD by the inverse time Fourier transforms (equation 2.16).

$$R_x(\tau) = F^{-1}(S_x(f)) = \int_{-\infty}^{\infty} S_x(f) e^{-i2\pi f\tau}\, d\tau \tag{2.16}$$

This relation between the time domain (correlation function, $R_x(\tau)$) and the frequency domain (spectral density, S(f)) is called Einstein-Wiener-Khinchin theorem.

The expected power in a voltage signal across a unit resistor is given by equation 2.17.

$$E[x^2(t)] = R_x(0) = \frac{1}{2\pi}\int_{-\infty}^{\infty} S_x(j\omega)\, d\omega = \int_{-\infty}^{\infty} S_x(f)\, df \tag{2.17}$$

$*$ A second definition of PSD can be developed as shown in equation 2.18.

$$S_x(j\omega) = \lim_{T\to\infty} \frac{1}{2T}\int_{-T}^{T} E[|X(j\omega)^2|] \tag{2.18}$$

For that, we define $X(j\omega)$ as the Fourier transform of the signal $x(t)$.

There are two main approaches of power spectrum estimation: parametric and non-parametric methods. The non-parametric approach is directly related to the second definition and doesn't rely on data model. However, the parametric method assumes that the signal is characterized by a model and then permits the estimation of its parameter.

The parametric approaches, can be used only when there is enough information about the signal under study, which allows a better formulation of a model. Therefore, in our research we will focus on non-parametric techniques. Table 2.3 illustrates a description of some non-parametric methods.

TABLE 2.3: Non-parametric method description [47]

Non-parametric method		Features
Periodogram		- Estimated PSD is defined by equation $\hat{S}(f) = N * \frac{\|X(f)\|^2}{F_s}$; (N: Number of samples, F_s: Sampling rate and $\mid X(f) \mid$: Fourier transforms of x (t)). - Simple to compute. - High resolution for long data length. - Poor spectral estimator as it has high variance. - Useful when there is a high SNR.
Modified-Periodogram	Welsh's method	- Averaging the PSD after dividing the time series data into M overlapped segments. - Reduces the large fluctuation of the Periodogram. - Useful in case of low SNR
	Barlett's method	- Averaging the Periodogram after dividing the time record in M non-overlapped segments - High resolution - Large leakage - Relatively large variance
	Blackman Tukey	- Applying window to correlation function - Minimizes the variance of the estimator
	Multitaper Method	- Filtering a length signal L through a filter bank (a set of filters in parallel) of LFIR band pass filters. Computing the Periodogram of the power of each filtered signal - Useful for long data length

We remark that the Periodogram is used later in the PSD estimation as it combines both simplicity of computation and high resolution for long data length that characterize signals under study.

One of the most frequently applied techniques in impedance spectrum measurement is based on the sine wave signal.

2.3.2 Voltage controlled current source

The voltage controlled current source plays an important role to ensure a safe and stable current injected on a human body and biological tissues. It is a challenge to generate an AC-current with a constant amplitude in a wide frequency range from low frequencies up to 1 MHz. The aspects considered in the circuit analysis of the current excitation are: Output impedance, output current and operational amplifier characteristics.

The function of voltage controlled current source (VCCS) is to generate a current I_2 that is independent on the voltage V_2 and is determined only by the control voltage V_1 [48]. In practice, the voltage controlled current source has the equivalent circuit given in Figure 2.12.

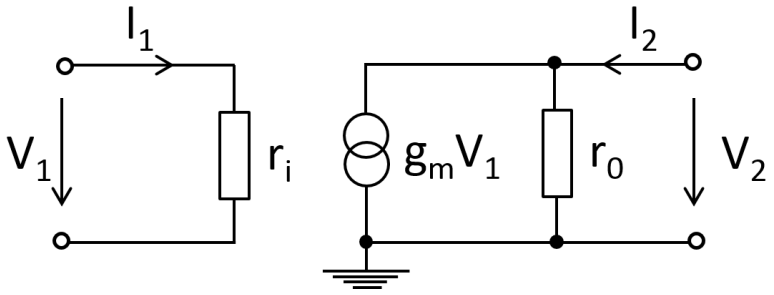

FIGURE 2.12: Low frequency equivalent circuit of real voltage controlled current source [48]

Its transfer characteristics are:

$$I_1 = \frac{1}{r_i} V_i + 0 \times V_2 \tag{2.19}$$

$$I_2 = g_m \times V_1 - \frac{1}{r_0} V_2 \tag{2.20}$$

where r_i, r_0 and g_m are respectively the input resistance, output resistance and mutual conductance or transconductance. For infinite output resistance (r_0=∞), ideal voltage controlled current source is obtained. It generates a controlled output current I_2 proportional to a controlling input voltage V_1 (equation 2.21).

$$I_2 = g_m \times V_1 \tag{2.21}$$

In real implementation, voltage controlled current sources have neither stable current amplitude nor high output impedance in the frequency range of interest. This is due to the presence of stray capacitances and the non-ideal characteristics of the amplifiers especially at high frequencies.

For a current source requiring "b"-bits accuracy, its resolution is equal to:

$$|\underline{I}_{Load\,min} - \underline{I}_{Load\,max}| \leqslant \frac{\underline{I}_{out}}{2^b} \tag{2.22}$$

Therefore the output impedance $\underline{Z}_{out}$ (Figure 2.13) should be larger than:

$$|\underline{Z}_{out}| > 2^b \times |\underline{Z}_{Load\,max} - \underline{Z}_{Load\,min}| \tag{2.23}$$

For biological tissues, the high frequency impedance at 1 MHz varies from 100 Ω to 1 kΩ, whereas low-frequency impedance at 5 kHz varies from 2 kΩ to 10 kΩ [31].

TABLE 2.4: Output impedance depending on current source's accuracy

Accuracy (bits)	Frequency (kHz)	Load (kΩ)	Output impedance (kΩ)
10	5	2 – 10	8 192
	1000	0.1 – 1	921.6
11	5	2 – 10	16 384
	1000	0.1 – 1	1 843.2
12	5	2 – 10	32 768
	1000	0.1 – 1	3 686.4
13	5	2 – 10	65 536
	1000	0.1 – 1	7 372.8
14	5	2 – 10	131 072
	1000	0.1 – 1	14 745.6

At the frequency range of interest from 5 kHz to 1 MHz (Table 2.4), the output impedance must be larger than 8.19 MΩ and then 921.6 kΩ, respectively (Equation

2.8). Therefore, the aim in this thesis is to design a voltage controlled current source with a high output impedance $\underline{Z}_{out}$ of approximately 10 MΩ at 5 kHz and 1 MΩ at 1 MHz when changing the load $\underline{Z}_{Load}$ from 100 Ω to 10 kΩ. Figure 2.13 depicts the Norton equivalent circuit of ideal current source.

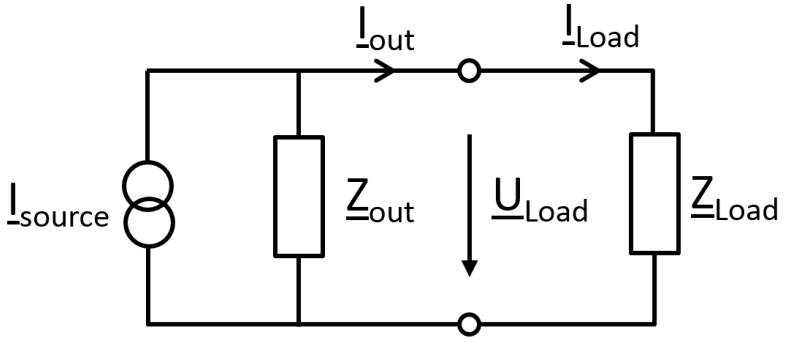

FIGURE 2.13: Norton equivalent circuit of ideal current source

The larger $\underline{Z}_{out}$ the smaller influence $\underline{Z}_{Load}$ has. When $\underline{Z}_{out}$ is infinite, $\underline{I}_{Load}$ is a constant, which is independent of $\underline{Z}_{Load}$.

$$\underline{I}_{Load} = \frac{\underline{Z}_{out}}{\underline{Z}_{out} + \underline{Z}_{Load}} \underline{I}_{out} \tag{2.24}$$

For the minimum load impedance $\underline{Z}_{Load\,min} = 100\ \Omega$, the miminum load current is equal to $\underline{I}_{Load\,min} = 149.98\ \mu$A. Then the error for the minimum load is as follows:

$$\epsilon = \frac{\underline{I}_{out} - \underline{I}_{Load\,min}}{\underline{I}_{out}} = 0.013\% \tag{2.25}$$

For the maximum load impedance $\underline{Z}_{Load\,max} = 10$ kΩ, the maxinum load current is equal to $\underline{I}_{Load\,max} = 149.85\ \mu$A (Table 2.5). Then the error for the maximum load is the following:

$$\epsilon = \frac{\underline{I}_{out} - \underline{I}_{Load\,max}}{\underline{I}_{out}} = 0.1\% \tag{2.26}$$

TABLE 2.5: Output current errors at high and low frequency

Frequency (kHz)	Load (kΩ)	Output current (μA)	Output impedance (kΩ)	Load current (μA)	Error (%)
5	10.00	150	10000	149.98	0.013
1000	0.10		1 000	149.85	0.100

In experiment conditions, we have $|\underline{Z}_{Load}| \ll |\underline{Z}_{out}|$. Thus, we can write:

$$\frac{\underline{I}_{Load}}{\underline{I}_{out}} = \frac{1}{1 + \frac{\underline{Z}_{Load}}{\underline{Z}_{out}}} = 1 - \frac{\underline{Z}_{Load}}{\underline{Z}_{out}} + o(\frac{\underline{Z}_{Load}}{\underline{Z}_{out}})^2 \tag{2.27}$$

Then the relative error can be expressed by:

$$\epsilon = \frac{\underline{I}_{Load} - \underline{I}_{out}}{\underline{I}_{out}} \cong |\frac{\underline{Z}_{Load}}{\underline{Z}_{out}}| \leq |\frac{\underline{Z}_{Load\,max}}{\underline{Z}_{out}}| = \frac{10k\Omega}{10M\Omega} = 10^{-3} = 0.1\% \tag{2.28}$$

For an output impedance between 1 MΩ and 10 MΩ, the error of the output current must be therefore lower than 0.10%. In the next chapter, a detailed literature review is expounded and analyzed about the types of voltage controlled current source.

3. State of the art of current excitation for bioimpedance measurement

Voltage controlled current sources (VCCS) for impedance measurements can be classified in two big classes which are the so called the voltage-mode approach and the current-mode approach (Figure 3.1). The main difference between both classes of current sources is the fact that the output is a true current source, in the case of the current-mode approach. In case of the voltage-mode approach, the current is generated in the feedback of an inverting amplifier due to the virtual ground.

The type of the load is decisive in the case of the voltage-mode. The voltage-mode approach can be classified in both floating load or grounded load. For the grounded load, Howland and Tietze are the main representatives, while the so called "load in the loop" approach is suitable for the floating load type.

The aim of this chapter is to describe the typical current sources in both current-mode and voltage-mode, and evaluate them considering their advantages and limitations for usability in bioimpedance measurement systems.

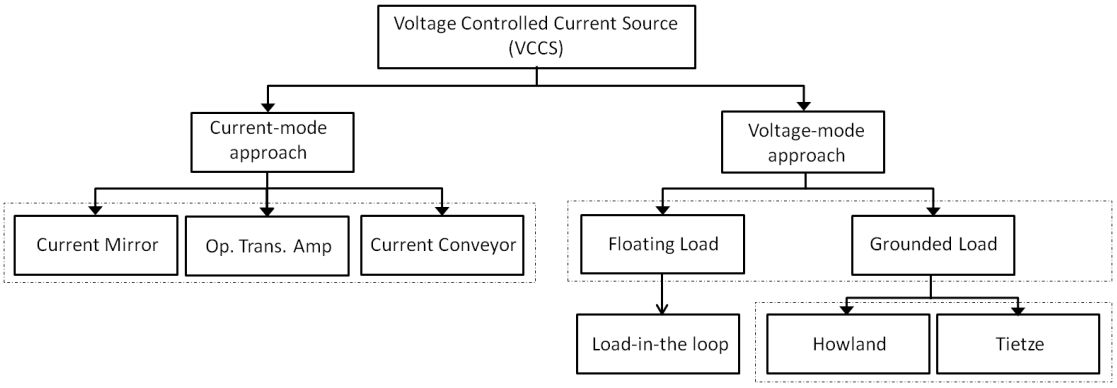

FIGURE 3.1: Classification of different approaches for voltage controlled current sources [49]

3.1 VCCS in current mode approach

In the current-mode approach, the output signal current is generated by a true current source and not by a voltage transformed to a current, like in the case of the VCCS in voltage mode described in the next section. This is the case of the current sources e.g. based on operational transconductance amplifier, supply current sensing and current conveyors [50] which can realize a current source with a sufficiently high output resistance able to provide a stable supply.

3.1.1 Operational transconductance amplifier

An Operational Transconductance Amplifier (OTA), implemented in the CMOS or bipolar technology, converts the voltage differential inputs (V_{in+} ,V_{in-}) into an output current I_{out}. Its ideal transfer characteristic is expressed as follows:

$$I_{out} = g_m(V_{in+} - V_{in-}) \tag{3.1}$$

where g_m is an adjustable transconductance controlled by the input bias current I_{bias} and an auxiliary current I_{abc} (Figure 3.2).

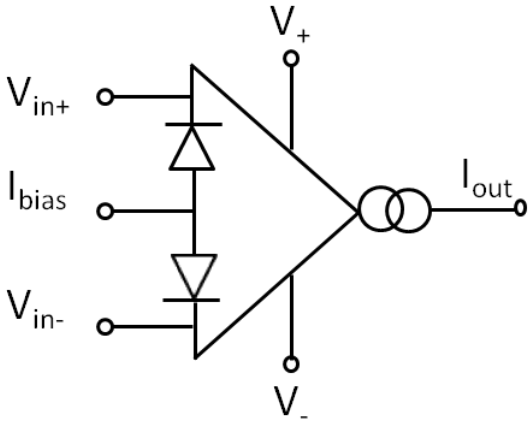

FIGURE 3.2: Operational transconductance amplifier schematic [51]

Different operational transconductance amplifiers are commercially available such as the CA3080, which is the simplest one. It consists of only the source coupled

differential pair [51] and current mirrors biasing the input transistors and generating the output current. In Table 3.1, an overview of commercially available OTAs and their output current are given.

TABLE 3.1: Selected commercial operational transconductance amplifiers

Transconductance amplifier	Output current (μA)	
	Min	Max
CA3080/CA3280	350	650
NE5517	350	650
LM13600/LM13700	350	650
OPA660	10000	15000
LT1228	25000	125000
MAX435/436	-15000	15000

None of the presented commercial operational transconductance amplifiers except MAX435/436 corresponds to the requirements of the output current's amplitude for personal health monitoring. Their output currents are more than the desired injected peak-to-peak (500 μA) at 5 kHz. For MAX435/436, it is no more recommended for new designs circuits.

The main drawback of OTA is that the output current is linear to the input voltage only in a limited operation range [52].

Therefore, different non-commercial operational transconductance amplifiers were designed with stable output current's amplitude corresponding to the medical requirements in definite wide frequency range. For a stable output current, current source should have high output impedance in the whole working frequency range. As mentioned in the previous chapter, an output impedance of 10 $M\Omega$ and 1 $M\Omega$ at respectively 10 kHz and 1 MHz is required for bioimpedance applications.

Hong proposed in [53] an architecture which consists of two OTA without cascade circuit (Architecture 1) (Table 3.2). This architecture is an adaptively biased differential pair using two transistor squaring circuits [51]. The output impedance is constant at low and high frequencies with 3.1 $k\Omega$. In order to maximize the output impedance, the first architecture is connected to a cascade circuit (Architecture 2). At a high frequency (1 MHz) and a low frequency (5 kHz), the output

impedance is increased and is equal respectively to 40 $k\Omega$ and 2 $M\Omega$. By adding a resistor between the inputs in the first architecture (Architecture 3), the output impedance increases and reached 5 $M\Omega$ at 5 kHz and around 200 $k\Omega$ at 1 MHz.

TABLE 3.2: Implemented operational transconductance amplifiers

Reference	OTA based voltage controlled current source	Output impedance (kΩ)	
		5 kHz	1 MHz
Hong [53]	Architecture 2	2000	40
	Architecture 1	3.1	3.1
	Architecture 3	5000	157
Filho [36]	Current conveyor (CCII)	70800	2800
	Class-AB OTA	70800	2800
	Class-A OTA	2800	695.5
Hong [54]	Two-stage OTA with negative feedback loop	13000	1000

Fihlo implemented in [36] a class-A and a class-AB operational transconductance amplifier. The designed class-A OTA circuit has an output impedance equal to 2.8 $M\Omega$ at 5 kHz and around 700 $k\Omega$ at 1 MHz. The designed class-AB OTA circuit reaches an output impedance of 70.8 $M\Omega$ at a low frequency (5 kHz) and decreases to approximately 2.8 $M\Omega$ at a high frequency (1 MHz).

Hong proposed in [54] two-stage OTA with negative feedback loop by including a sense resistor. This structure reached 1 $M\Omega$ at 1 MHz and 13 $M\Omega$ at 5 kHz. For a stable and precise transconductance, a precise sense resistor is required. As a conclusion, the drawback of this implementation is that the output impedance is dependent on the transconductance. The higher the transconductance the higher the output impedance is. In this way, a complex hardware is obtained. Furthermore, in experiments, the mismatch between transistors and voltage limitations due to transistors coming out of saturation are sources of errors in the circuit design. This leads to an increase for the output impedance especially at high frequencies. In fact, there is an upper and lower limit where the output current is nonlinear and dependent of the output voltage [55].

3.1.2 Supply current sensing

Based on the supply current sensing technique, the output current is equal to the sum of the currents in the supply leads of the operational amplifier. To sense the current flowing in the supply leads of the operational amplifier, Graeme [56] used complementary field effect transistors [57]. The accuracy of the circuit is dependent on the resistor mismatch, the gain bandwidth and the power supply rejection of the operational amplifier. Instead of field effect transistors, Hart&Braker used a set of complementary current-mirrors. With Hart&Braker's class-B voltage to current converter, the resistor mismatch problem is avoided but cross-over distortion problem appeared. Using the class-AB voltage converter proposed by Rao&Haslett, the performance of the output circuit is improved.

To avoid the source of voltage modulation caused by the connection of the current mirrors to the circuit's open loop, Wilson has proposed to connect the current mirrors m_1 and m_2 in the feedback arrangement (Figure 3.3). It could be either shunt or series feedback. By connecting the current mirrors in the shunt feedback, the accuracy of the VCCS is dependent on the accuracy of the current mirrors [51].

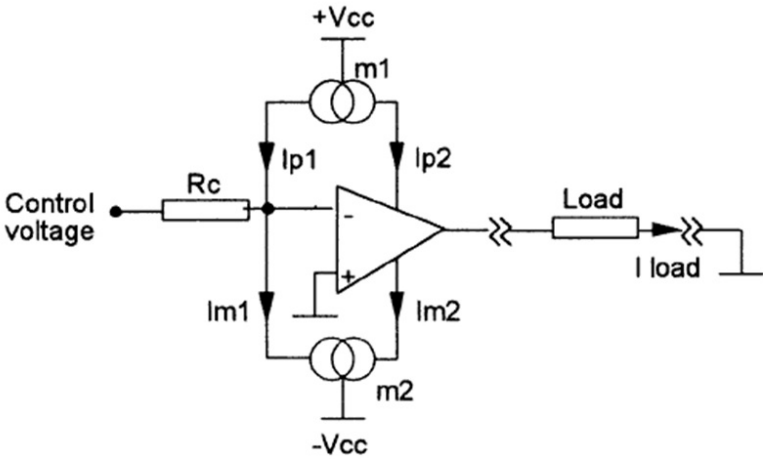

FIGURE 3.3: Wilson's VCCS using shunt feedback [51]

The Wilson's voltage to current converter using a shunt feedback (Figure 3.3) presents the problem of high distortion performances. By adding an adjustable bleed current into the feedback loop, the output offset is dramatically reduced [58]. Its output impedance is equal to 80 $k\Omega$ at a low frequency (1 kHz). Denyer used in

[59] the modified Wilson four-transistor current mirror with a DC feedback correction which actively eliminates the offset. The output impedance of the proposed circuit is around 8 $M\Omega$ at 50 kHz and decreases dramatically to around 30 $k\Omega$ at a high frequency (1 MHz). At 100 kHz, Leung [60] and Record [61] realized an output impedance equal to 300 $k\Omega$ and 2 $M\Omega$ respectively [62].

The non-idealities of the current mirrors and the operational amplifier limit the performances of the current source circuit. In fact, the performances of the current copied by the transistors affect the performances of the current source. In addition, the drawbacks of these circuits are the relatively high power supply requirements and high distortions.

3.1.3 Current conveyor

The second generation current conveyor can be used in different applications [63]. It is three-port network with two inputs terminal X and Y and one output Z represented by the following hybrid matrix:

$$\begin{bmatrix} i_Y \\ v_x \\ i_z \end{bmatrix} = \begin{bmatrix} 0 & 0 & 0 \\ 1 & 0 & 0 \\ 0 & \pm 1 & 0 \end{bmatrix} \begin{bmatrix} v_Y \\ i_x \\ v_z \end{bmatrix} \tag{3.2}$$

The polarity of the current-conveyor changes depending on the flow's direction of the inputs i_x and i_y (Figure 3.4). The positive sign means that the inputs i_x and i_y are in the same direction, whilst the negative sign means that the inputs i_x and i_y flow in the opposite direction.

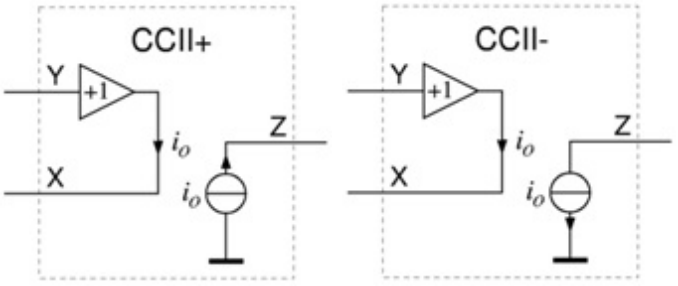

(a) (b)

FIGURE 3.4: Second generation current conveyor [64]

The voltage controlled current source is realized based on second generation current conveyor (CCII+) (Figure 3.5). In this case, the input voltage V_y is single ended and its transconductance (R_1) is externally controlled [65].

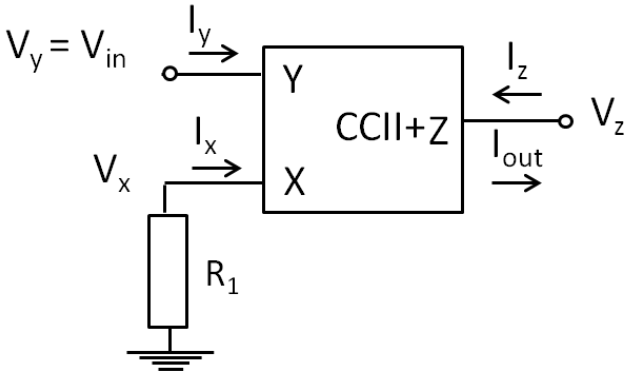

FIGURE 3.5: VCCS based on current conveyor [63]

Its output current is represented as following:

$$I_{out} = \frac{V_{in}}{R_1} \tag{3.3}$$

Bragos proposed in [66] an AC-coupled current source which consists of the current-feedback amplifier from Analog Devices (AD844) used as current conveyor and a DC-feedback circuit. The advantage of using an integrated circuit rather than the designed supply-current sensing is that the temperature matching and the bipolar complementary process of the transistors are ensured. The proposed circuit is designed in two configurations depending on the phase shift between the input voltage and the output current: inverting and non-inverting. The output impedance of the designed circuit is 7.6 $M\Omega$ at 5 kHz and 700 $k\Omega$ at 1 MHz for non-inverting source. For the inverting source, the output impedance decreases to 5.5 $M\Omega$ at 5 kHz and 300 $k\Omega$ at 1 MHz.

Kaewpoonsuk proposed in [67] a voltage controlled current source composed by a commercial current conveyor CCII (AD844), instrumentation amplifier, difference amplifier and feedback resistor. The performances of the proposed circuit are dependent on the frequency performance of the instrumentation and differential amplifiers. Experimental results show that the output current decreases approximately from 100 kHz. Jivet proposed in [68] a voltage controlled current

source based on a modified current conveyor (CCII). At low frequencies, the output impedance reached 123 $M\Omega$. While at a high frequency (1 MHz), the output impedance decreases. The limitations are due to the mismatch between transistors and coming out of saturation i.e. the collector and emitter are at higher potential than the base. In this case, the current driven into the base is not enough to forward bias the base-collector and the base-emitter junctions. These restrictions influence the accuracy circuit by increasing its current noise and reducing the output impedance.

Table 3.3 shows that only the current conveyor (CCII) proposed by Fihlo [36] and the modified Hart&Barker's universal converter network designed by Tetrzopoulos [69] have reached the requirements. They have an output impedance larger than 10 $M\Omega$ and 1 $M\Omega$ at 5 kHz and at 1 MHz respectively. Because the development of current-mode approaches is expensive and requires custom fabrication, the interest in this study remains on the voltage-mode approach.

TABLE 3.3: Supply current sensing based VCCS

Reference	Supply current sensing based VCCS	Output impedance (kΩ)	
		5 kHz	1 MHz
Denyer [70]	Wilson's current source with DC feedback correction	7900	32
Tetrzopoulos [69]	Modified Hart & Barker's universal converter network	17500	2500
Bragos [66]	CCII (Non-inverting)	7600	700
	CCII (Inverting)	5500	300
Filho [36]	Current conveyor (CCII)	70800	2800

3.2 VCCS in voltage mode approach

In the voltage-mode approach, the output current is generated by the voltage in one or more nodes of an active circuit, including operational amplifiers, such as the Howland topologies, Tietze topology and the so called "load-in-the-loop" approach. Each current source approach has two possibilities of the load connection: the load can be floating (load-in-the-loop) or grounded (Howland circuit). In this section, the advantages and disadvantages of the voltage mode approach's types are discussed.

3.2.1 Floating load

The traditional implementation of a voltage controlled current source based on a single operational amplifier with a floating load as a feedback is known as load-in-the-loop current source (Figure 3.6).

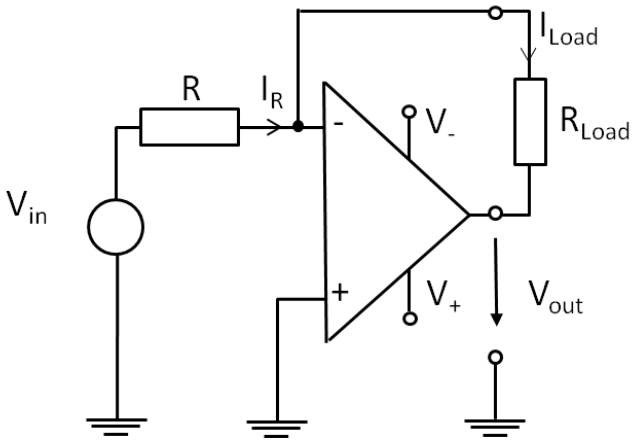

FIGURE 3.6: Load in the loop current source [50]

The terminal of the amplifier is virtually grounded. The current through R is

$$\underline{I}_R = \frac{\underline{V}_{in}}{R} \tag{3.4}$$

The same current flows through the load and it can be expressed as follows:

$$\underline{I}_{Load} = \frac{\underline{V}_{in}}{R} \tag{3.5}$$

Whereas, the voltage at the output of the amplifier is defined by

$$\underline{V}_{out} = -R_{Load}\underline{I}_{Load} = -\frac{R_{Load}}{R}\underline{V}_{in} \tag{3.6}$$

The output impedance is dependent especially at high frequencies on the value of the load and the resistor R and the characteristics of the operational amplifier. Sheingold proposed in [71] a modified load in the loop circuit by adding a feedback resistor in parallel with the load (Figure 3.7). In the load-in-the-loop structure, the output impedance is dependent on the feedback resistor connected in parallel with

the load. If the feedback resistor's value increases, the output impedance increases to around 1.5 MΩ at both low and high frequencies (Table 3.4). The reason behind the fact that the higher the value of the feedback resistor the higher the output impedance is, is that the feedback resistor acts like a current divider. However, the high value of the feedback resistor demands high voltage of the source driving the current leading to a high power consumption.

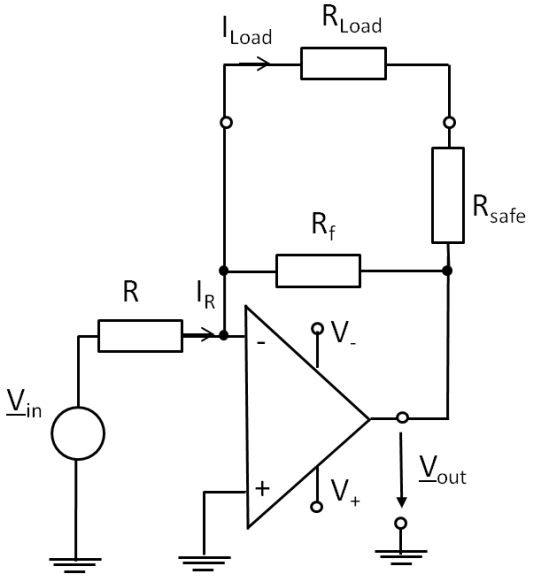

FIGURE 3.7: Load in the loop current source with feedback resistor [50]

To avoid these limitations, Seoane proposed in [50] to add a stage consisting of a current conveyor (CCII) before the loop in the loop structure (Figure 3.8).

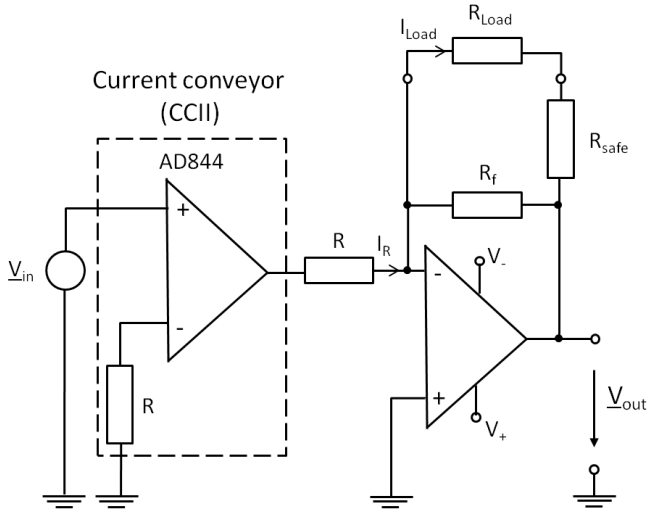

FIGURE 3.8: Load in the loop circuit driven by current conveyor [50]

When connecting the load-in-the-loop to the current conveyor, the output impedance at 1 MHz increases slightly but remains low around 400 kΩ [72].

TABLE 3.4: Selected floating load current sources

Type	Reference	Output impedance (kΩ)				Note
		1 kHz	5 kHz	100 kHz	1 MHz	
H-Bridge Howland	Fihlo [73]	858		787	102	Bipolar modified Howland without buffer
		272		249	61	Bipolar modified Howland with buffer
	Hong [74]			629	63	Inverting Howland H-Bridge configuration
Load-in-the-loop Current driven load in the loop	Seoane [72]		380		360	$R_f = 390$ kΩ
			1500		1500	$R_f = 1$ MΩ
			380		410	$R_f = 390$ kΩ

The choice of high performance characteristics of the operational amplifier leads to a high output impedance. Unfortunately, at high frequency (1 MHz), the output impedance decreases due to the frequency-dependence of the characteristics of the operational amplifier.

As a conclusion, the floating load in the feedback loop has a significant effect on stability. In case of complex loads, which are not purely resistive, additional components are required to insure stability.

3.2.2 Grounded load

For voltage controlled current sources for grounded loads, several topologies have been studied in literature, such as mirrored enhanced Howland circuit [36] [74],

inverting and non-inverting enhanced Howland in single and dual configuration with negative or positive feedback [73] and Tietze topology.

3.2.2.1 Tietze topology

The Tietze topology [48] uses two operational amplifiers with negative feedback in cascade configuration with six resistors (Figure 3.9). The output current $\underline{I}_{Load}$ and the output impedance $\underline{Z}_{out}$ for Tietze circuit are respectively:

$$\underline{I}_{Load} = -\frac{R_2 R_4 \underline{V}_{in}}{R_1 R_3 R_5} \tag{3.7}$$

$$\underline{Z}_{out} = \frac{R_3 R_5 R_6}{R_2 R_4 - R_3(R_5 + R_6)} \tag{3.8}$$

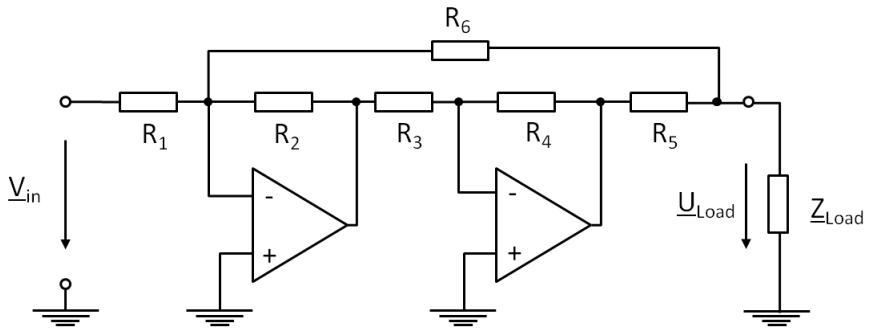

FIGURE 3.9: Schematic of Tietze circuit [48]

In order to realize a very high output impedance, the denominator of $\underline{Z}_{out}$ in equation 3.8 should be almost zero. We can therefore calculate the so-called balance condition for a high accuracy current source in Tietze topology as given in equation 3.9.

$$\frac{R_3}{R_4} = \frac{R_2}{R_5 + R_6} \tag{3.9}$$

$$If\ R_3 = R_2\ and\ R_4 = R_5 + R_6\ then\ \underline{I}_{Load} = \frac{R_4 \underline{V}_{in}}{R_1 R_5} \tag{3.10}$$

Abad proposed in [75] a Tietze circuit which has an output impedance of 5 MΩ at 1 kHz and 5.5 kΩ at 1 MHz. The output impedance at high frequency decreases due to the resistor mismatching and the low performance of the selected operational amplifiers.

3.2.2.2 Howland topologies

Structure simplicity and good performances are the main advantageous properties of the Howland topologies. Thus, Howland is an extensively used circuit for the current source design with grounded loads in bioimpedance measurements. The Howland circuit design includes inverting and non-inverting configurations using single or double amplifiers (Figure 3.10).

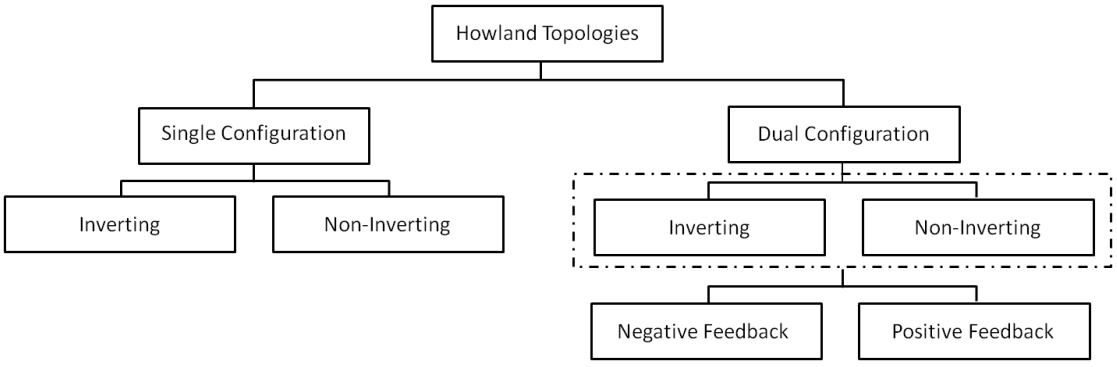

FIGURE 3.10: Howland circuit topologies [49]

The basic Howland circuit, called also Howland current pump, is using a single operational amplifier with both negative and positive feedback with four resistors (Figure 3.11). The output current or the load current $\underline{I}_{Load}$ is fed back to both positive and negative inputs.

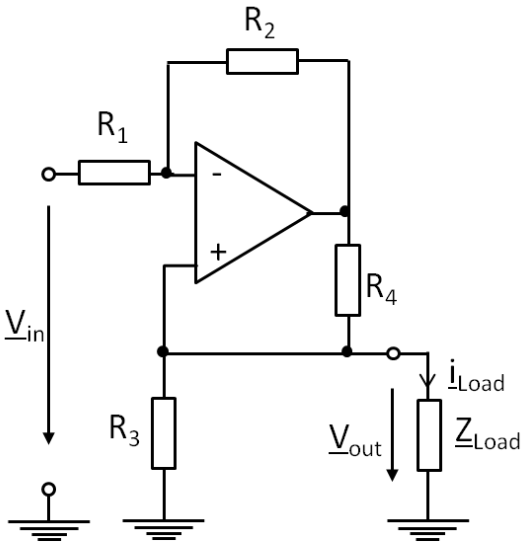

FIGURE 3.11: Howland circuit: Inverting single configuration (ISC) [76]

Hammond [77] and Chen [78] used first the basic Howland circuit in their investigations. The output impedance at 100 kHz is less than 500 kΩ. The drawback of this configuration is the waste of power consumed by the resistor R_1. To reduce this power consumption, the configuration is modified by splitting the resistor R_4 in two resistors R_{4a} and R_{4b} [79]. The new configuration, using a single operational amplifier with five resistors, is called improved Howland circuit (Figure 3.12).

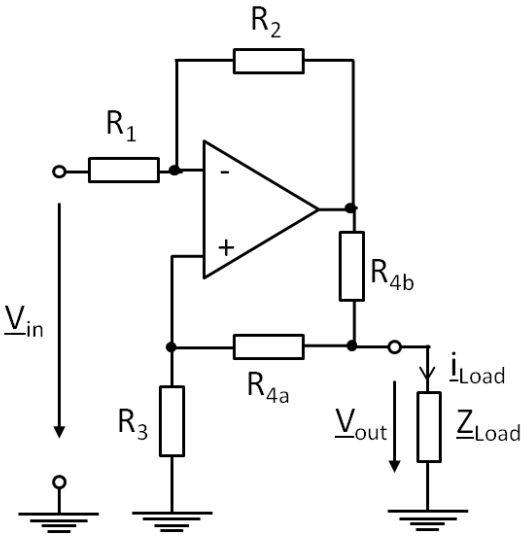

FIGURE 3.12: Improved Howland circuit: Inverting single configuration (ISC) [76]

The output current $\underline{I}_{Load}$ and the output impedance $\underline{Z}_{out}$ for the improved Howland inverting single configuration are expressed respectively by:

$$\underline{I}_{Load} = -\frac{R_2 \underline{V}_{in}}{R_1 R_{4b}} \tag{3.11}$$

$$\underline{Z}_{out} = \frac{R_1 R_{4b}(R_3 + R_{4a})}{R_2 R_3 - R_1(R_{4a} + R_{4b})} \tag{3.12}$$

In order to realize a very high output impedance, the denominator of $\underline{Z}_{out}$ in equation 3.12 should be almost zero. We can therefore calculate the so-called balance condition for a high accuracy current source in the single configuration of the improved Howland circuit as given in equation 3.13.

$$\frac{R_1}{R_2} = \frac{R_3}{(R_{4a} + R_{4b})} \tag{3.13}$$

$$If\ R_1 = R_2\ and\ R_3 = R_{4a} + R_{4b}\ then\ \underline{I}_{Load} = -\frac{\underline{V}_{in}}{R_{4b}} \tag{3.14}$$

Despite simple adjustment of output resistance by both positive and negative feedback, the Howland circuit may oscillate at high frequencies due to the presence of two feedback paths (negative and positive). For circuit stabilization at high frequencies, two capacitors, typically around 10 pF, are connected in parallel with the feedback resistors [79].

Table 3.5 shows the output impedance of the selected Howland single configuration of inverting, non-inverting and differential improved designs. An inverting enhanced Howland voltage to current converter is proposed in [78] [73] [75] [76] [80] [81] [82] which has an output impedance lower than 200 kΩ at high frequency up to 1 MHz. For the non-inverting improved circuit, an output impedance is lower than 500 kΩ at high frequency [75] [83]. Pandiev suggested in [84] a voltage controlled current source for a grounded load using an additional bipolar transistor. The output impedances at 5 kHz and 1 MHz are 10 kΩ and 100 Ω respectively.

TABLE 3.5: Selected Howland single configuration

Type	Reference	Output impedance (kΩ) 1 kHz	5 kHz	100 kHz	1 MHz	Note
Inverting Basic	Hammond [77]			22		Resistor matching level =1%
				200		Resistor matching level = 0.1%
	Chen [67]		3800	425		
Inverting Improved	Chen [78]		5700	638		
	Fihlo [73]	537		786	102	
	Abad [75]	7500	3000		9	
	Fihlo [76]	610			70	
	Cheng[80]	30000		517	1.6	
	Jossinet [85]				1000	
	Islam [81]			50		
	Zaho [82]	180	180	180	180	THS4021
		95	95	5	<1	THS4631
		10	10	<1	<1	THS3061
	Zhangyong [86]			18000	1000	
	Hong [53]				<100	Power supply voltage of ± 5V
					2100	Power supply voltage of ±15V
Non-inverting	Abad [75]	4000	2000		6.7	
	Lee [83]			<500		
	Naeini [87]			10000	10000	
	Pandiev [84]	30	20	0.3	0.08	With bipolar transistor
Differential	Garcia [88]			50		
	Tucker [89]	3300	3300	3300	500	Lead lag compensated

In dual configuration of the improved Howland current source, a second amplifier has been added as voltage follower, in one of feedback paths of the first operational amplifier. The addition of the voltage follower increases the circuit's output impedance. Figure 3.13 depicts a dual configuration with voltage follower connected in the negative feedback.

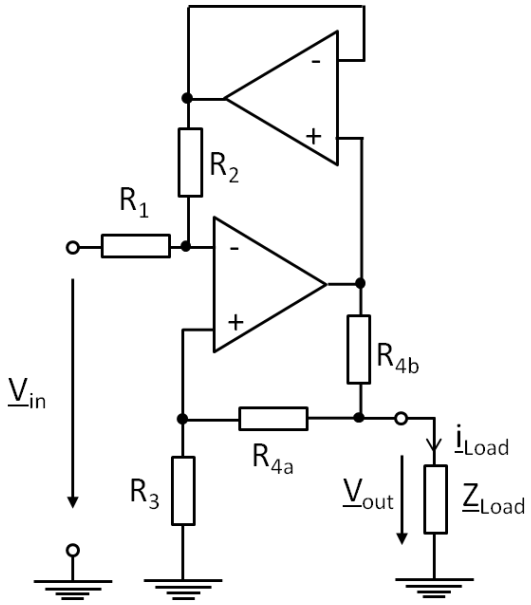

FIGURE 3.13: Improved Howland circuit: Inverting dual configuration (IDC) with negative feedback [76]

The output current $\underline{I}_{Load}$ and the output impedance $\underline{Z}_{out}$ for the dual configuration with negative feedback can be expressed as:

$$\underline{I}_{Load} = \frac{R_2(R_3 + R_{4a})}{R_3 R_{4b}(R_1 + R_2)} \underline{V}_{in} \tag{3.15}$$

$$\underline{Z}_{out} = \frac{R_3 R_{4b}(R_1 + R_2)}{R_1 R_{4b} + R_1 R_{4a} - R_2 R_3} \tag{3.16}$$

Equation 3.17 is the balance condition corresponding to a very high output impedance of the improved Howland circuit in the dual configuration.

$$\frac{R_1}{R_2} = \frac{R_3}{R_{4a} + R_{4b}} \tag{3.17}$$

The output current is dependently related to the balance condition. If the resistors are not tightly matched, the current source performance is affected, i.e. the output impedance degrades and the output current is instable over the working frequency range. A resistance trimming can be a solution in certain applications to get precise values of resistors. However, trimmers are bulkier than normal resistors and are mechanically and thermally instable. That's why it is preferable to choose standard resistors with tolerance not exceeding 0.1 % than using trimmers [79]. Using one or two additional resistors in series with the main resistor [90] and the resistor's percentage tolerance less than 0.1 % provides good performances and an accurate circuit.

TABLE 3.6: Selected Howland dual and triple configurations

Type	Reference	Output impedance (kΩ)			
		1 kHz	5 kHz	100 kHz	1 MHz
Dual	Fihlo [76]	570		602	62
Inverting	Abad [75]	20000	7500		14.6
	Chen [78]		5078	579	
Dual	Abad [75]	7500	3000		9.6
Non-inverting	Radhakrishman [91]	25		3	
	Zhangyong [86]			30000	1600
Triple	Zhang [92]	1100			1100
Non-inverting	Khalighi [93]			<500	

Moreover, operational amplifier intrinsic specifications play an important role to ensure a high output impedance. The main parameters of operational amplifiers, that are highly recommended to get a stable current and a high output impedance especially at high frequencies, are low input bias current, low input offset, high slew rate, high common mode rejection ratio and high bandwidth [94]. In the next section, the influence of the amplifier's parameters on the output impedance and the current error will be analyzed.

Howland configurations and Tietze circuit [75] have output impedance lower than 110 kΩ at 1 MHz. In [73], all configurations of Howland do not fulfill the output impedance's requirements. Tietze circuit is compared to Howland configurations [75]. Only dual configuration with negative feedback in inverting and non-inverting configuration has an output impedance larger than 10 MΩ at low frequencies but at high frequencies, it becomes lower than 1 MΩ (Table 3.6). Based on these

results, we decide to investigate current sources for voltage-mode approach with grounded loads, especially on Tietze topology and Howland based circuits.

3.2.2.3 Evaluation of current sources approaches

The voltage controlled current can be in current or voltage mode. The development of current-mode is expensive and requires custom fabrication. Hence, the interest in this thesis remains on the voltage mode according to the requirements of bioimpedance portable device. The voltage approach is classified in two types depending on the load connection. For grounded loads, no additional components are needed [95].

Voltage controlled current source based on floating load (load-in-the-loop) and grounded load (Howland circuit) are compared [96]. Figure 3.14 depicts that the floating loads structure degrades severely comparing to Howland topologies when changing the load from 1 kΩ to 10 kΩ. Therefore, the floating load is instable and not sufficiently performant.

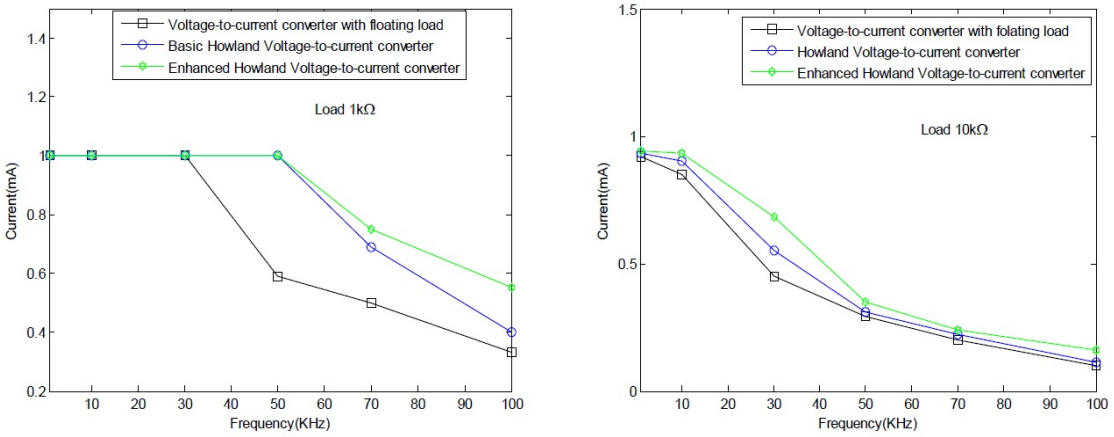

FIGURE 3.14: Comparison of grounded load (Howland) and floating load for fixed load [96]

Grounded load provides a better circuit's stability and thus the stability of the current flowing through the patient. In bioimpedance measurements this mode is more accepted because of patient safety and in order to increase accuracy of measurement. In the next chapter, we will investigate suitable configuration of these circuits in order to get a high output impedance at both low and high frequencies. For this purpose, the most important structures, such as Howland

and Tietze topologies, are evaluated by simulations after the choice of suitable configurations and components.

4. Current excitation for grounded load

Stable and accurate voltage controlled current source requires high output impedance. However, the output impedance is affected by the resistor balancing and parameters of the operational amplifier e.g. bandwidth, open loop gain and input bias current. Therefore, to achieve high output impedance, high performant amplifiers is strongly needed. In this chapter, the influence of characteristics of operational amplifiers and discrete circuit elements on the output current and output impedance of the voltage controlled current source is studied.

4.1 Influence of operational amplifier characteristics

The real output current of the circuit is dependent on the input bias current or the common mode input current $\underline{I}_B = \frac{\underline{I}_B^+ + \underline{I}_B^-}{2}$, the input offset current or the

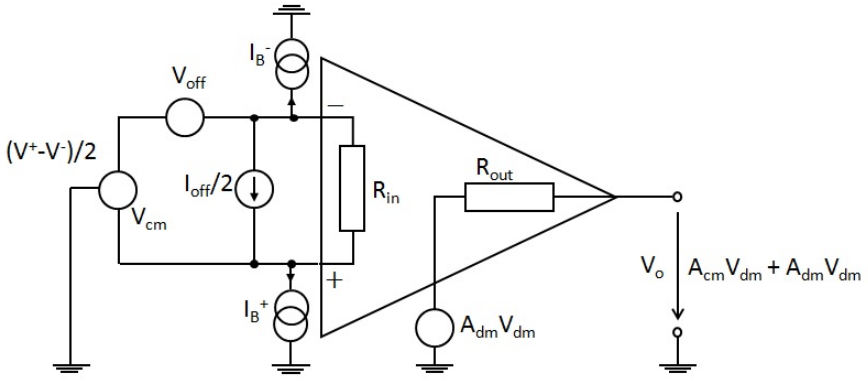

FIGURE 4.1: Non ideal parameters in operational amplifier

differential mode input current $\underline{I}_{off} = \frac{\underline{I}_B^+ - \underline{I}_B^-}{2}$ and the input offset voltage $\underline{V}_{off} = \underline{V^+} - \underline{V^-}$ (Figure 4.1). To study the influence of these parameters in the output current of the current source, the dual enhanced Howland in negative feedback is

taken as a case study (Figure 4.2). Setting the current flowing in each node to be equal and assuming that $\underline{V^+} = \underline{V^-}$, we can determine the following relations: In node $\underline{V^+}$, we have

$$\frac{0 - \underline{V^+}}{R_3} = \frac{\underline{V^+} - \underline{V_{out}}}{R_{4a}} \tag{4.1}$$

Similarly, in Node $\underline{V^-}$

$$\frac{\underline{V_{in}} - \underline{V^+}}{R_1} = \frac{\underline{V^+} - \underline{V_0}}{R_2} \tag{4.2}$$

$$\underline{I_{Load}} = \frac{\underline{V^+} - \underline{V_{out}}}{R_{4a}} + \frac{\underline{V_0} - \underline{V_{out}}}{R_{4b}} \tag{4.3}$$

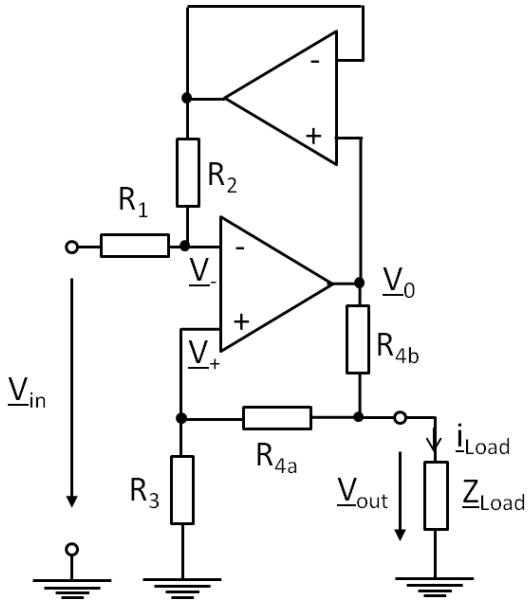

FIGURE 4.2: Enhanced Howland current source with voltage follower in negative feedback [76]

Using equations (4.1) and (4.2), the voltages $\underline{V^+}$ and $\underline{V^-}$ are as follows:

$$\underline{V^+} = -\frac{R_3}{R_{4a} + R_3}\underline{V_{out}} \tag{4.4}$$

$$\underline{V_0} = -\frac{R_2}{R_1}\underline{V_{in}} + \frac{R_3}{R_{4a} + R_3}\underline{V_{out}} \tag{4.5}$$

Substituting $\underline{V^+}$ and $\underline{V_o}$ in equation (4.3), we can define the output current and impedance of the enhanced Howland current source as follows:

$$\underline{I_{Load}} = -\frac{R_2}{R_1 R_{4b}}\underline{V_{in}} + \frac{R_2 R_3 - R_1 R_{4b} - R_1 R_{4a}}{R_1 R_{4b}(R_{4a} + R_3)}\underline{V_{out}} \tag{4.6}$$

$$R_0 = \frac{R_1 R_{4b}(R_{4a} + R_3)}{R_2 R_3 - R_1 R_{4b} - R_1 R_{4a}} \tag{4.7}$$

Infinite output impedance is necessary for an accurate and stable voltage controlled source. Therefore, the following condition should be satisfied

$$R_2 R_3 = R_1 R_{4b} + R_1 R_{4a} \tag{4.8}$$

Consequently, the output current becomes equal to:

$$\underline{I}_{Load} = -\frac{R_2}{R_1 R_{4b}} \underline{V}_{in} \tag{4.9}$$

4.1.1 Input bias current

In the previous analyses, we assume that the amplifier input bias currents are equal to zero and $\underline{V}^- = \underline{V}^+$. If we include the input bias current, equations (4.1), (4.2) and (4.3) become:

$$\frac{0 - \underline{V}^+}{R_3} - \underline{I}_B^+ = \frac{\underline{V}^+ - \underline{V}_{out}}{R_{4a}} \tag{4.10}$$

$$\frac{\underline{V}_{in} - \underline{V}^+}{R_1} - \underline{I}_B^- = \frac{\underline{V}^+ - \underline{V}_0}{R_2} \tag{4.11}$$

$$\underline{I}_{Load} = \frac{\underline{V}^+ - \underline{V}_{out}}{R_{4a}} + \frac{\underline{V}_0 - \underline{V}_{out}}{R_{4b}} \tag{4.12}$$

Using equations (4.10) and (4.11), we obtain the following expressions of the voltages $\underline{V}^+$ and $\underline{V}_o$:

$$\underline{V}^+ = -\frac{R_3}{R_{4a} + R_3} \underline{V}_{out} - \frac{R_3 R_{4a}}{R_3 + R_{4a}} \underline{I}_B^+ \tag{4.13}$$

$$\underline{V}_0 = -\frac{R_2}{R_1} \underline{V}_{in} + \frac{R_3}{R_3 + R_{4a}} \left(\frac{R_1 + R_2}{R_1}\right) \underline{V}_{out} - \frac{R_3 R_{4a}}{R_3 + R_{4a}} \left(\frac{R_1 + R_2}{R_1}\right) \underline{I}_B^+ + R_2 \underline{I}_B^- \tag{4.14}$$

Thus, the output current of the circuit when considering the input bias current, is defined as follows:

$$\underline{I}_{Load} = -\frac{R_2}{R_1 R_{4b}} \underline{V}_{in} + \frac{R_2 R_3 - R_1 R_{4b} - R_1 R_{4a}}{R_1 R_{4b}(R_3 + R_{4a})} \underline{V}_{out} - \frac{R_2}{R_{4b}} (\underline{I}_B^+ - \underline{I}_B^-) \tag{4.15}$$

For an infinite impedance of the voltage controlled current source, the output current becomes equal to

$$\underline{I}_{Load} = -\frac{R_2}{R_1 R_{4b}}\underline{V}_{in} - \frac{R_2}{R_{4b}}(\underline{I}_B^+ - \underline{I}_B^-) \tag{4.16}$$

For stable current in the working frequency range, the input bias current should be as low as possible. Setting this configuration of resistors for an input voltage of 600 mV to get a stable current of 150 μA, $R_1 = R_3 = 6k\Omega$, $R_2 = 6k\Omega$, $R_{4a} = 1k\Omega$, and $R_{4b} = 2k\Omega$. According to equation (4.16), the input offset current should be lower than 1 μA to have an output current error lower than 0.01%.

4.1.2 Input offset voltage

In the previous analyses, we assume that $\underline{V}^- - \underline{V}^+ = 0$. In the presence of an amplifier input offset however, this becomes $\underline{V}^- - \underline{V}^+ = \underline{V}_{off}$. n this case, equations (4.1), (4.2) and (4.3) become: can be written as follows:

$$\frac{0 - \underline{V}^+}{R_3} = \frac{\underline{V}^+ - \underline{V}_{out}}{R_{4a}} \tag{4.17}$$

$$\frac{\underline{V}_{in} - \underline{V}^+ + \underline{V}_{off}}{R_1} = \frac{\underline{V}^+ - \underline{V}_{off} - \underline{V}_0}{R_2} \tag{4.18}$$

$$\underline{I}_{Load} = \frac{\underline{V}^+ - \underline{V}_{out}}{R_{4a}} = \frac{\underline{V}_0 - \underline{V}_{out}}{R_{4b}} \tag{4.19}$$

Based on equations (4.17) and (4.18), voltages $\underline{V}^+$ and $\underline{V}_o$ are derived as below:

$$\underline{V}^+ = -\frac{R_3}{R_{4a} + R_3}\underline{V}_{out} \tag{4.20}$$

$$\underline{V}_0 = -\frac{R_2}{R_1}\underline{V}_{in} + (\frac{R_3}{R_{4a} + R_3}\underline{V}_{out} - \underline{V}_{off})(\frac{R_1 + R_2}{R_1}) \tag{4.21}$$

$$\underline{I}_{Load} = -\frac{R_2}{R_1 R_{4b}}\underline{V}_{in} + \frac{(R_2 R_3 - R_1 R_{4b} - R_1 R_{4a})}{R_1 R_{4b}(R_{4a} + R_3)\underline{V}_{out}} - \frac{(R_1 + R_2)}{R_1 R_{4b}}\underline{V}_{off} \tag{4.22}$$

Infinite impedance permits the generation of the following expression of the output current

$$\underline{I}_{Load} = -\frac{R_2}{R_1 R_{4b}}\underline{V}_{in} - \frac{(R_1 + R_2)}{R_1 R_{4b}}\underline{V}_{off} \tag{4.23}$$

For stable current in the working frequency range, the input bias current should be as low as possible. Setting this configuration of resistors for an input voltage of 600

mV to get a stable current of 150 μA, $R_1 = R_3 = 6k\Omega$, $R_2 = 6k\Omega$, $R_{4a} = 1k\Omega$, and $R_{4b} = 2k\Omega$. According to equation (4.23), the input offset current should be lower than 1 μA to have an output current error lower than 0.01%. As a conclusion, when taking into consideration the amplifier bias current and output offset with infinite output impedance, the output current of the circuit becomes

$$\underline{I}_{Load} = -\frac{R_2}{R_1 R_{4b}}\underline{V}_{in} - \frac{R_2}{R_{4b}}(\underline{I}_B^+ - \underline{I}_B^-) - (\frac{R_1 + R_2}{R_1 R_{4b}})\underline{V}_{off} \tag{4.24}$$

To ensure a stable output current through a wide frequency range with an error lower than 0.01%, the input offset voltage and the input offset current should be lower respectively than 2 mV and 1 μA. Therefore, characteristics of the operational amplifier should be selected carefully to not affect the output impedance, the output current error and the flatness. To fulfill these requirements, three amplifiers are selected (Table 4.1).

Table 4.1: Selected operational amplifiers [49]

Amplifier	Input offset current (μA)	Input offset voltage (mV)	Slew rate (V/μs)	Bandwidth (MHz)	Open loop gain (dB)	CMRR (dB)
AD8021	0.1	0.4	170	490	86	98
AD8041	0.2	2.0	160	160	95	80
THS4304	0.5	0.5	830	3000	50	73

THS4304 is selected for its high bandwidth around 3 GHz and high slew rate of 830 V/μs and AD8041 is chosen for its low input offset current around 0.2 μA and high open loop gain (95 dB). AD8021 is also selected due to its high common mode rejection ratio (CMRR) (98 dB), low input voltage noise and acceptable wide bandwidth (490 MHz). Its gain bandwidth product is variable related to the value of its dc decoupling capacitor on the feedback network. The increase of this compensation capacitor helps to reduce oscillations at high frequencies. That's why, it is called also gain compensation capacitor.

4.2 Influence of the passive components

After selecting the main intrinsic specifications of the amplifier, the influence of passive components on the output impedance is studied using the same case study described in the previous section. In this comparison, we use the dual configuration with negative feedback.

4.2.1 Passive components configuration

To compare different configurations, errors related to the changing of the frequency and the loads are calculated. The error at 1 kHz or at 1 MHz is the difference between the maximum and minimum values of the current with different loads at a same frequency (equation 4.25). The error shows the ability of the current source to remain constant despite of the load variation.

$$Error = [\frac{I_{max} - I_{min}}{I_{min}}]_{same\,frequency,different\,loads} \tag{4.25}$$

While the flatness is the difference between the maximum and minimum values of the current with a same load over the whole frequency range (equation 4.26). The flatness shows the available bandwidth of the current source. The flatness of each load is measured. The one with the highest value is called the worst flatness. The corresponded load is indicated in parenthesis.

$$Flatness = [\frac{I_{max} - I_{min}}{I_{min}}]_{same\,load,different\,frequencies} \tag{4.26}$$

All configurations have been simulated and compared with load changed from 10Ω to 10 kΩ along a frequency range between 1 kHz and 1MHz. The input voltage is fixed around 600 mV for a desired output current of 150 μA. AD8021 is compared with uncompensated amplifiers AD8041 and THS4304. Different values of the compensation capacitor, (C_c) have been used in order to find the optimum configuration with lowest error.
Table 4.2 shows that errors at low frequencies are smaller than errors at high frequencies. Comparing between two amplifiers, the uncompensated operational amplifier AD8041 and THS4304 has the biggest error at 1 MHz and biggest flatness. The compensated operational amplifier AD8021 has best performances, not only errors at 1 MHz, but also the flatness. This is because of the addition of the

compensated capacitor to the amplifier. In addition, from Table 4.2, we see that the higher the compensation capacitance, the higher the error at 1 MHz and the flatness. The best configuration for lowest error at 1 MHz and lowest flatness is: $R_1 = 5k\Omega$, $R_1 = 2.5k\Omega$, $R_3 = 5k\Omega$, $R_{4a} = 0.5k\Omega$, $R_{4b} = 2k\Omega$ and $C_c = 1$ pF for all amplifiers (AD8021, AD8041 and THS4304).

TABLE 4.2: Simulation results with different resistor configurations [49]

Amplifier	Resistance (kΩ)					Capacitance (pF)	Error (%)		Flatness (%)
	R_1	R_2	R_3	R_{4a}	R_{4b}	C_c	1 kHz	1 MHz	
AD8041	6	3	6	1	2		0.007	0.221	0.270
	5	**2.5**	**5**	**0.5**	**2**		**0.007**	**0.195**	**0.240**
	9	2	9	1	1		0.006	0.274	0.313
AD8021	6	3	6	1	2	7	0.020	0.101	0.142
	6	3	6	1	2	10	0.020	0.141	0.189
	6	3	6	1	2	3	0.020	0.049	0.079
	6	3	6	1	2	1	0.020	0.022	0.048
	5	**2.5**	**5**	**0.5**	**2**	**1**	**0.021**	**0.017**	**0.043**
	9	2	9	1	1	1	0.016	0.028	0.049
THS4304	6	3	6	1	2		0.269	0.243	0.029
	5	**2.5**	**5**	**0.5**	**2**		**0.260**	**0.235**	**0.028**
	9	2	9	1	1		0.258	0.232	0.029

4.2.2 Passive components tolerance

$$\underline{I}_{Load} = -\frac{R_2}{R_1 R_{4b}}\underline{V}_{in} + (\frac{R_2 R_3 - R_1 R_{4b} - R_1 R_{4a}}{R_1 R_{4b}(R_{4a} + R_3)})\underline{V}_{out} \tag{4.27}$$

$$\underline{I}_{Load} = -\frac{R_2(1 \pm T)}{R_1 R_{4b}(1 \pm T)^2}\underline{V}_{in} = -\frac{R_2}{R_1 R_{4b}(1 \pm T)}\underline{V}_{in} \tag{4.28}$$

According to equation (4.28), the output current is inversely proportional to the tolerance of the passive components (T). The lower the tolerance, the lower the error of the output current is.

$$\underline{Z}_{out} = \frac{R_1 R_{4b}(R_{4a} + R_3)(1 \pm T)^3}{(R_2 R_3 - R_1 R_{4b} - R_1 R_{4a})(1 \pm T)^2} = \frac{R_1 R_{4b}(R_{4a} + R_3)(1 \pm T)}{(R_2 R_3 - R_1 R_{4b} - R_1 R_{4a})} \tag{4.29}$$

According to equation (4.29), the output impedance is proportional to the tolerance of the passive components (T). The lower the tolerance, the higher the output impedance is. The tolerance of the chosen resistors in this work is 0.01%.

4.3 Comparative study of different configurations

4.3.1 Error and flatness

To compare between selected configurations, the error and flatness of the output current are simulated using the amplifier AD8041. From Table 4.3, all configurations have smaller errors and better fatnesses at low frequencies than at high frequencies. Comparing to other configurations, the inverting dual configuration (IDC) with negative feedback and Tietze circuit have error lower than 0.13% at both 1 kHz and 1 MHz.

TABLE 4.3: Simulation results of selected current source configurations [49]

Current Source Configurations	Error (%)		Worst Flatness (%)
	5 kHz	1 MHz	
ISC	0.048	0.195	0.255 (6 kΩ)
NISC	0.048	0.195	0.261 (6 kΩ)
IDC (Negative Feedback)	0.007	0.058	0.043 (4 kΩ)
NIDC (Positive Feedback)	0.308	0.450	0.176 (5 kΩ)
Tietze	0.033	0.089	0.265 (7 kΩ)

Inverting single configuration (ISC) and non-inverting single configuration (NISC) have small error at 1 kHz (0.048%) lower than 0.13%, but a quite higher at 1 MHz (0.19%) than 0.13%. The dual configuration with negative feedback has best performances, not only errors at 1 kHz (0.007%) and at 1 MHz (0.058%), but also the worst flatness (0.043%) at 4 kΩ (Figure 4.3). In the next step, the output impedance is simulated in terms of the configuration type and the amplifier characteristics. Tietze circuit, the single configuration and the dual configuration with negative feedback are studied as they have low error and flatness than the dual configuration with positive feedback.

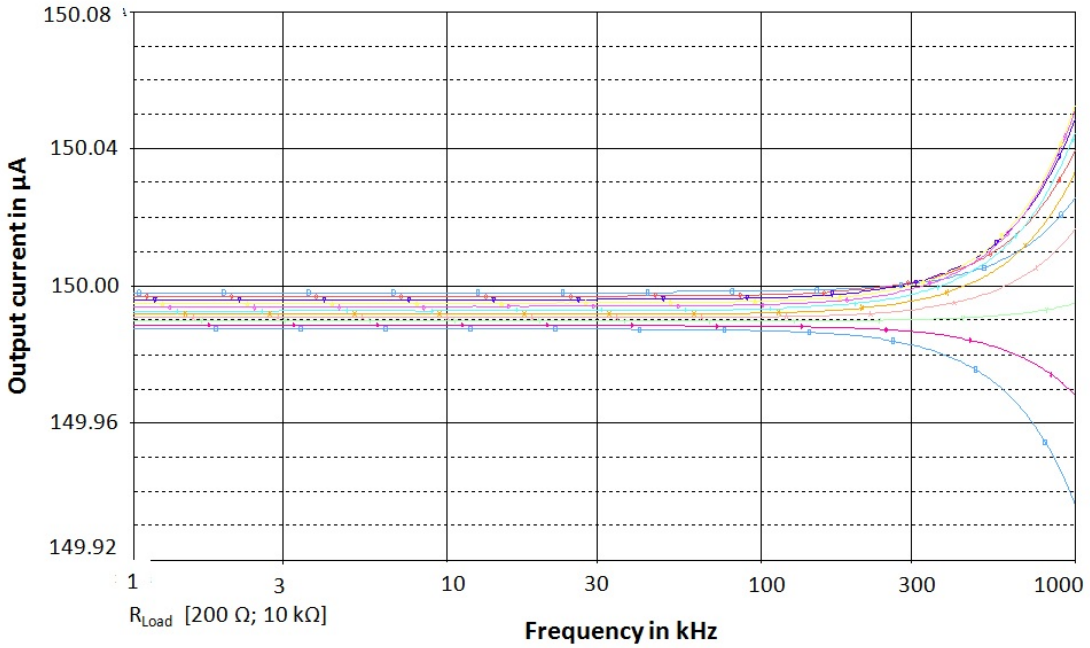

FIGURE 4.3: Output current of DCNF using AD8041

4.3.2 Output impedance with and without compensation

The challenge in the design of the current source is to ensure high output impedance at high frequencies. To increase the output impedance, compensation capacitors (C_1, C_2) are added to the circuit as shown in the following figure (Figure 4.4).

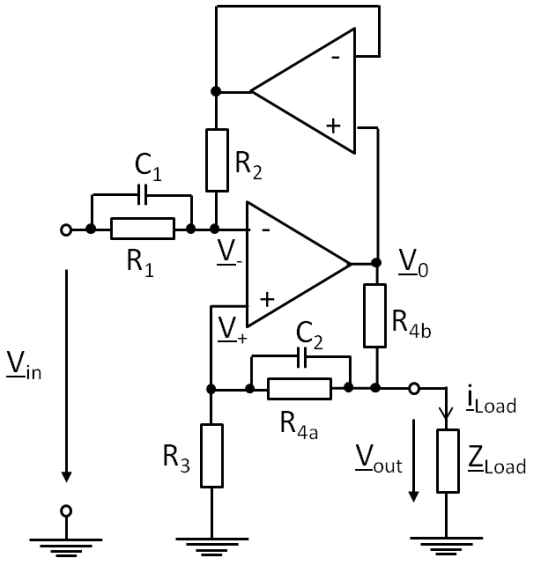

FIGURE 4.4: Dual enhanced Howland with negative feedback with compensation capacitors

Different values of compensation capacitors from 10 nF to 0.01 pF are simulated in order to choose the suitable values for high output impedance especially at high frequencies. It has been proven that using two 0.1 pF compensation capacities has the high value of the output impedance at low and high frequencies (Figure 4.5).

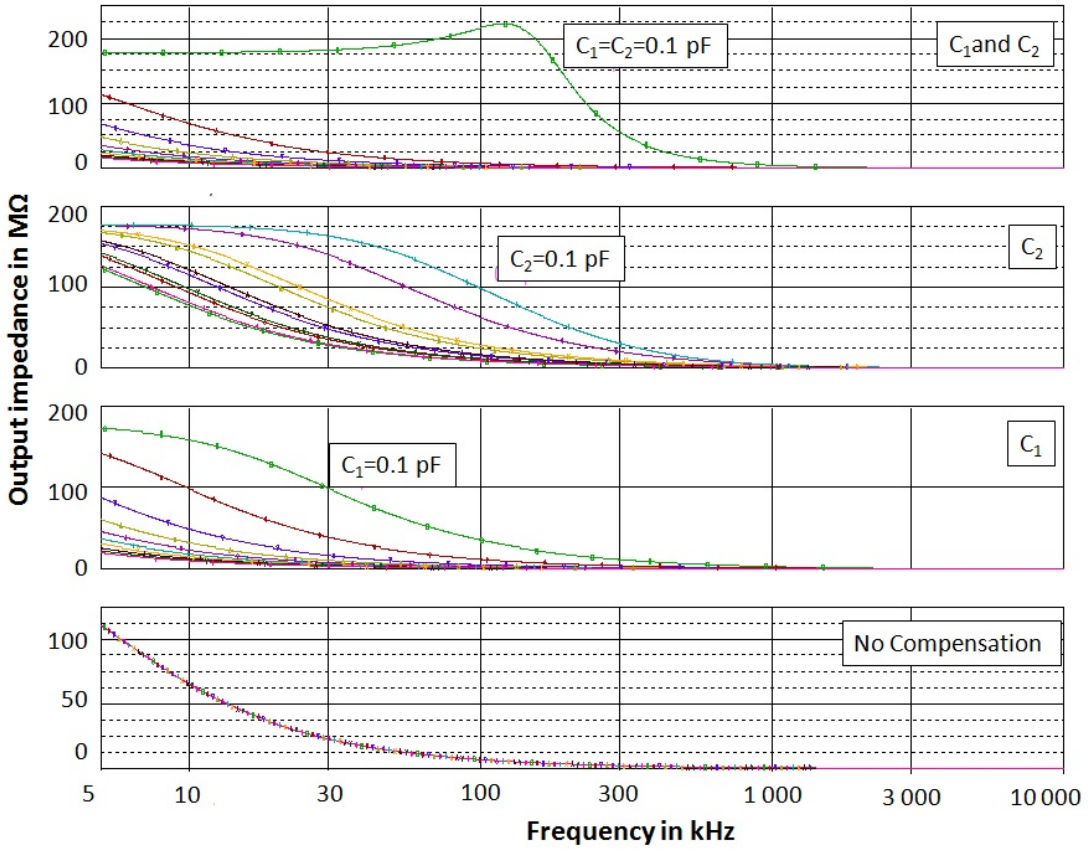

FIGURE 4.5: Inverting double configuration using AD8041 with different compensation capacitors

Table 4.4 shows the dependence of the output impedance of the amplifier's characteristics and the configuration's type using two 0.1 pF compensation capacitors. As mentioned before, the output impedance should be higher than 10 MΩ and 1 MΩ respectively at 5 kHz and 1 MHz. Four cases fulfill these requirements.

TABLE 4.4: Output impedance dependences [49]

Circuit	Configuration	Amplifier	Output impedance (MΩ)			
			5 kHz	1 MHz	3 MHz	10 MHz
Howland	ISC	**AD8021**	**15.91**	**12.61**	2.08	0.18
		AD8041	25.00	0.32	0.10	0.02
		THS4304	1.44	1.42	1.28	0.69
	NISC	AD8021	15.64	0.43	0.14	0.04
		AD8041	22.00	0.47	0.14	0.01
		THS4304	1.44	0.44	0.15	0.04
	IDC (Negative Feedback)	**AD8021**	**62.41**	**1.16**	0.38	0.10
		AD8041	**177.82**	**4.33**	0.48	0.04
		THS4304	3.88	3.83	2.15	0.19
Tietze	Cascade configuration	**AD8021**	**10.65**	**2.71**	0.57	0.57
		AD8041	28.55	0.63	0.13	0.13
		THS4304	1.02	1.27	1.27	0.52

The first case is the inverting single configuration (ISC) using the compensated amplifier AD8021. At both 5 kHz and 1 MHz, the output impedance is more than 10 MΩ and more than 1 MΩ until 3 MHz (Figure 4.6).

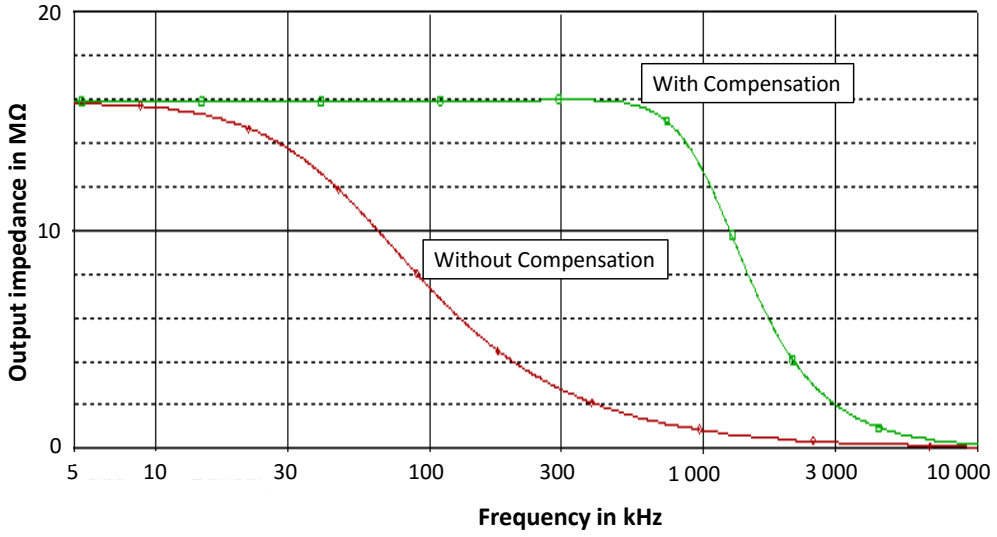

FIGURE 4.6: Inverting single configuration using AD8021

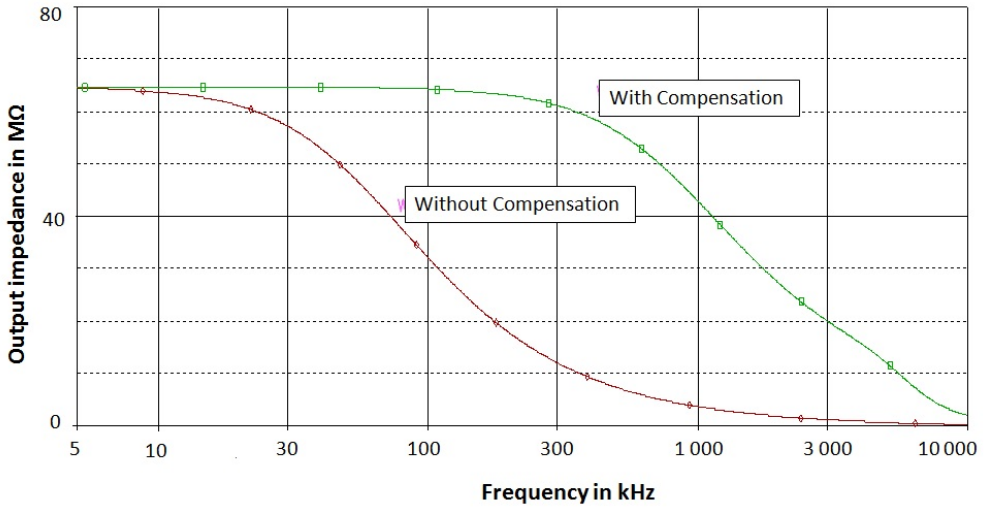

FIGURE 4.7: Inverting double configuration using AD8041

The second case is the inverting dual configuration (IDC) with negative feedback using AD8021 (Figure 4.7). At 5 kHz, the output impedance is around 60 MΩ and at 1 MHz, it is more than 1 MΩ.

The third case is the inverting dual configuration (IDC) with negative feedback using AD8041 (Figure 4.8). At 5 kHz, the output impedance is around 175 MΩ and at 1 MHz, it is more than 4 MΩ.

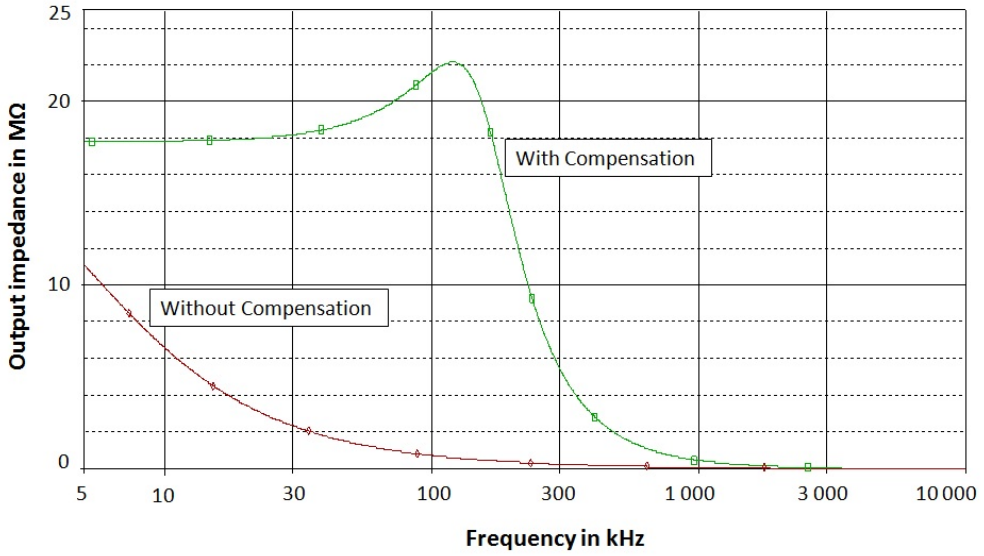

FIGURE 4.8: Inverting double configuration using AD8041

The fourth case and the last one is the Tietze circuit with a cascade configuration using AD8021 (Figure 4.9). Its output impedance has around 10 MΩ at 5 kHz and is higher than 1 MΩ at 1 MHz.
For all configurations, we observe a decrease of the output impedance at high frequencies due to the presence of stray capacitances. In the next chapter, the inverting dual configuration with negative feedback and Tietze are implemented with connection of a circuit minimizing the stray capacitance's effect.

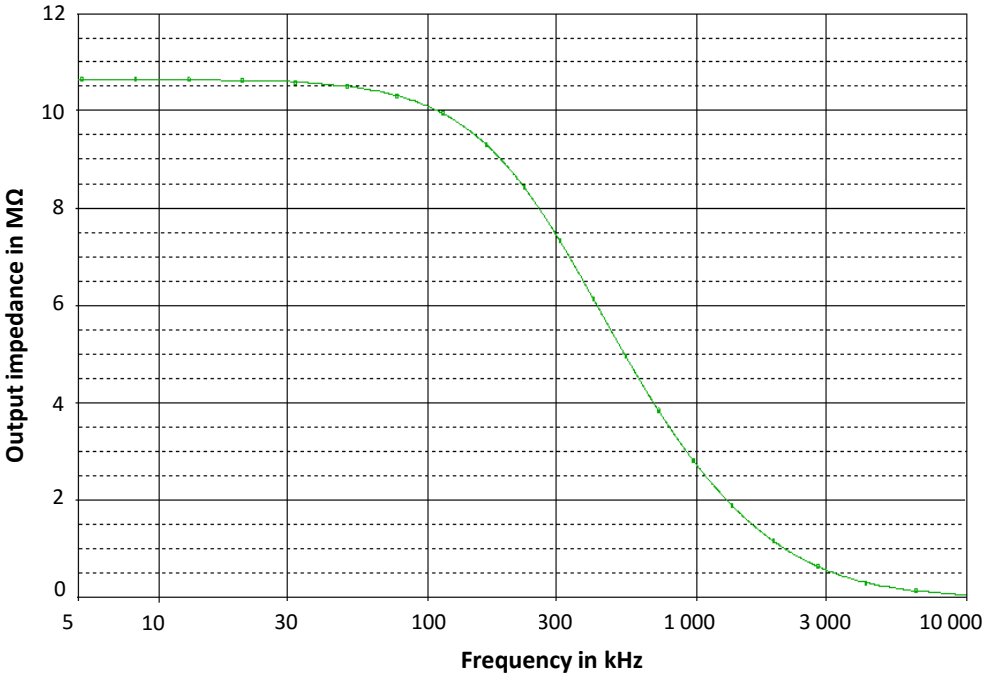

FIGURE 4.9: Tietze circuit using AD8021

5. Experimental investigations

In this chapter, experiments with a selection of simulated circuits from previous chapters are investigated and compared with investigations from literature. In experimental investigations, we deal with the high accuracy of the voltage controlled current source especially at a high frequency up to 1 MHz.

5.1 Analysis of the experimental results

In the experimental investigations, two aspects are mainly considered. The balance condition can be achieved only when the resistances are highly precise, even if as a matter of fact, all resistances have tolerances.

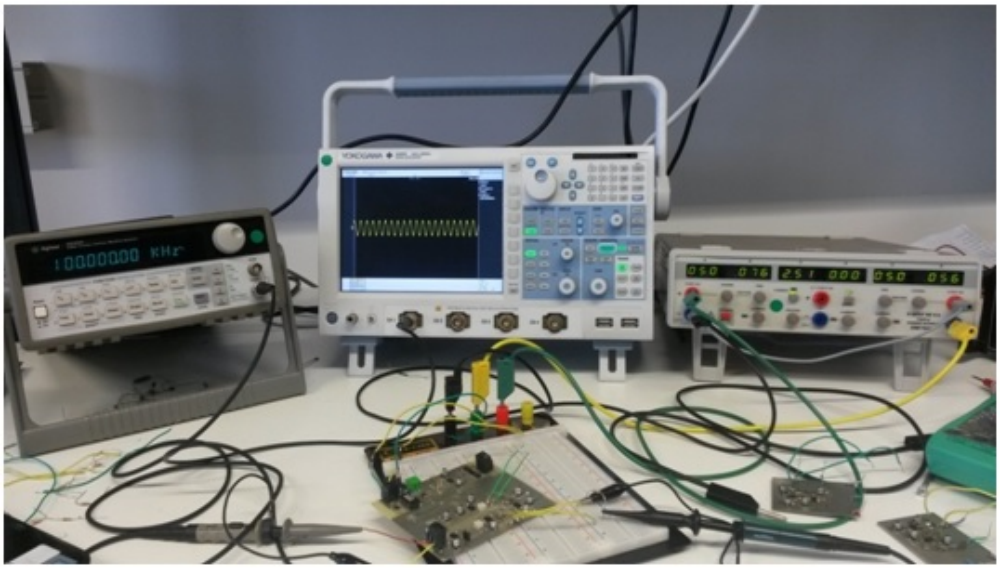

FIGURE 5.1: Experimental setup for voltage controlled current source measurement

The balance condition can therefore be fully achieved, but only can be approached. Using resistances with lower tolerances is a possible way to approach the condition. In the implementation, resistances with 0.1% tolerance are used (Figure 5.1).

5.1.1 Inverting dual configuration

The current source circuit is realized using an inverting double amplifiers configuration. The used amplifier from analog device is AD8041. The inverting dual configuration with negative feedback has small errors less than 1% both at low and high frequencies (Figure 5.2). At 1 kHz, the error is 0.54%, while the error at 1 MHz reaches 0.98%. Unfortunately, in this case the flatness is not quite good and achieves nearly 4% at the load 220 Ω.

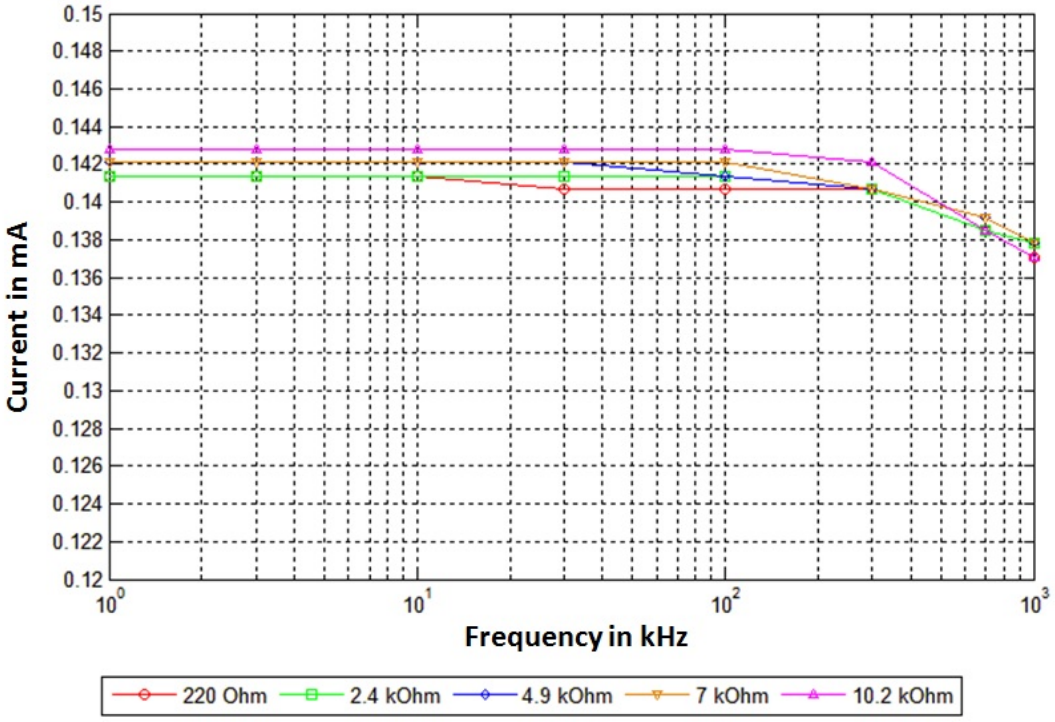

FIGURE 5.2: Inverting dual configurations with negative feedback [49]

With the high speed amplifier AD8041, the bandwidth of the current source has reached 1 MHz, which is hardly reported before.

5.1.2 Tietze circuit

Figure 5.3 depicts the output current of the Tietze circuit. The error at 1 kHz is approximately zero while the error at 1 MHz and the worst flatness are very high, more than 15%. This is due to the presence of the stray capacitances which affect decisively the circuit performances.

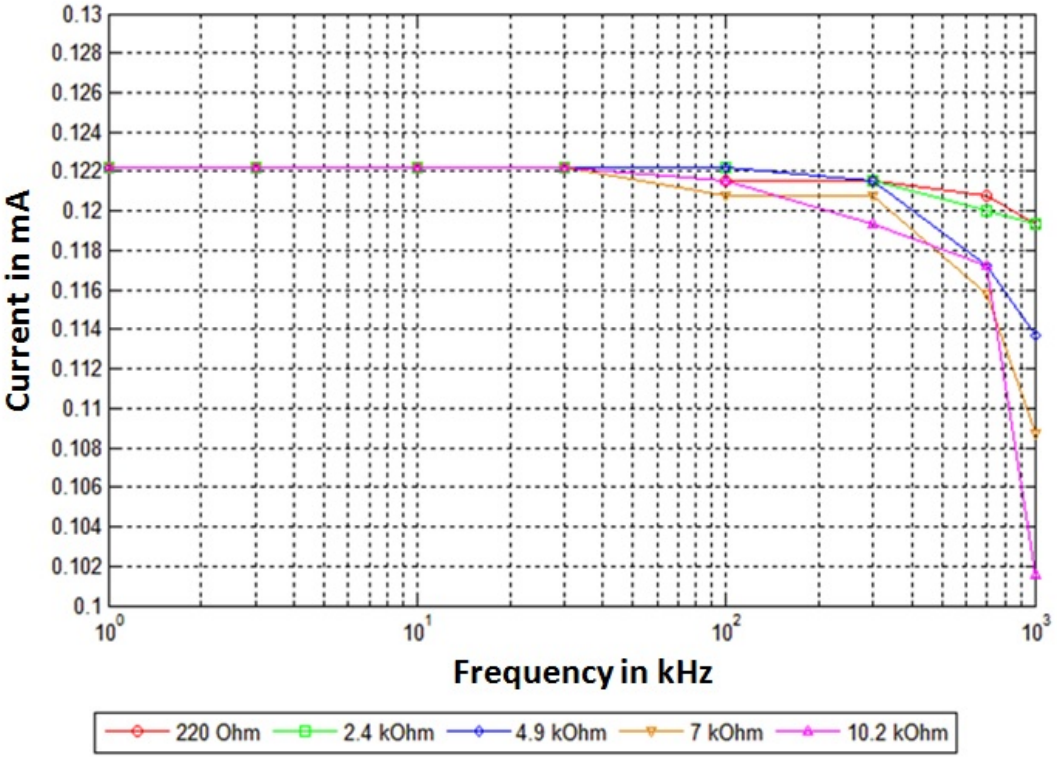

FIGURE 5.3: Tietze circuit [49]

Stray capacitances exist in leads, printed circuit board tracks and switches. The effect of stray capacitances could be minimized significantly with a careful circuit implementation, i.e. use of SMD components, short connections, avoid parallel tracks, etc. In the implementation, components with 0402 SMD packaging are used.

5.2 Compensation techniques for circuit stability at high frequencies

As reported in the previous section, in the real implementation of the circuit, the current magnitude can be degraded at high frequencies by stray capacitance C_S due to leads, printed circuit board tracks and switches [87]. The stray capacitances act in parallel with the output resistance of the current source.

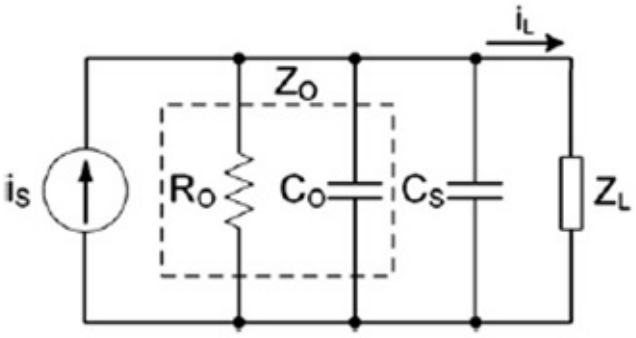

FIGURE 5.4: Norton equivalent circuit for real current sources with presence of stray capacitances [87]

Cancellation of stray capacitance is an effective way to keep the output current at a designed value at high frequencies. There are several methods, such as Wheatstone bridge (Figure 5.4) connected to Wagner ground, Generalized Impedance Converters (GIC) and Negative Impedance Converters (NIC) in order to minimize the influence of parasitic capacitance.

5.2.1 Wheatstone bridge

The Wheatstone bridge (Figure 5.5) consists of four resistances where three resistances are known and the fourth one is unknown. The unknown load is measured by exciting a constant current and measuring the voltage output.

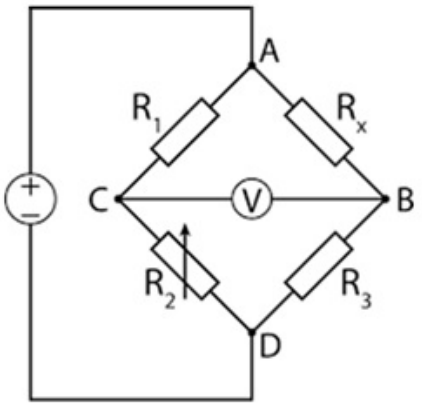

FIGURE 5.5: Wheatstone bridge [97]

To minimize the sensitivity to stray capacitances and maintain the bridge's stability, a Wagner ground is used. With low excitation's value, the sensitivity to noise is increasing; hence the circuit's stability is affected [97].

5.2.2 Generalized impedance converter

The Generalized Impedance Converter (GIC) contains two operational amplifiers and F_s [66][98]. The output of the GIC is:

$$Z_{GIC} = \frac{Z_1 Z_3 Z_5}{Z_2 Z_4} \tag{5.1}$$

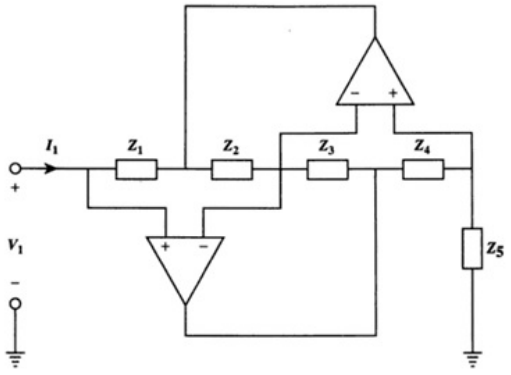

FIGURE 5.6: Generalized impedance converter circuit [98]

Depending on the components choice at the position 1 to 5 (Figure 5.6)), the Generalized Impedance converter can have many outputs, such as:

- Frequency-dependent-negative resistance defined by:

$$Z_{GIC} = -\frac{R_3}{C_1 C_5 R_2 R_4 \omega^2} \tag{5.2}$$

- Inductive behavior expressed by:

$$Z_{GIC} = \frac{R_1 R_3 R_5 j\omega\, C_2}{R_4} = j\omega\, L \tag{5.3}$$

In this investigation, we choose a structure generating an inductance behavior, due to its performance at high frequencies [36]. An inductive behavior can be realized using the topology given in (Figure 5.7):

$$L = \frac{R_1 R_3 R_5 C_4}{R_2} \tag{5.4}$$

In Norton equivalent circuit of real current source (Figure 5.7), the output current is associated with the output resistance, stray capacitance and inductance synthesized by GIC.

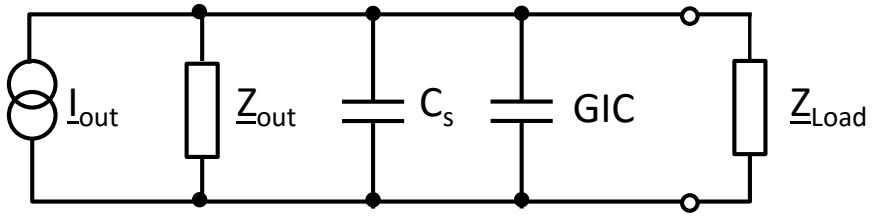

FIGURE 5.7: Norton equivalent circuit of real current source connected to GIC

When the imaginary part of parallel impedance is set to zero, the stray capacitance effects are completely cancelled.

$$Im(Z) = j\omega\, L + \frac{1}{j\omega\, C} \tag{5.5}$$

This condition can be fulfilled at:

$$\omega = \frac{1}{\sqrt{LC}} \tag{5.6}$$

The Generalized Impedance Converter (GIC) contains two operational amplifiers and five adjustable impedances. For multifrequency system, the inductance L must be adjusted at every frequency to fulfill the condition. To adjust the inductance, five resistors should be adjusted in the case of GIC. For this reason, this method is difficult to apply in order to cancel the stray capacitances.

5.2.3 Negative impedance converter

The Negative Impedance Converter (NIC) realizes in general negative impedances [99]. The topologies of Negative Impedance Converter (NIC) are:

- Negative resistance converter

$$Z_{NCC} = -R \tag{5.7}$$

- Negative capacitance converter

$$Z_{NCC} = -\frac{1}{j\omega\, C} \tag{5.8}$$

- Negative inductance converter

$$Z_{NCC} = -j\omega\, CR^2 = -j\omega\, L \tag{5.9}$$

The main interest in this work is to cancel the stray capacitance. Therefore, we focus on the Negative Capacitance Converter (NCC). NCC is composed of an amplifier, capacitance and two resistances (Figure 5.8).

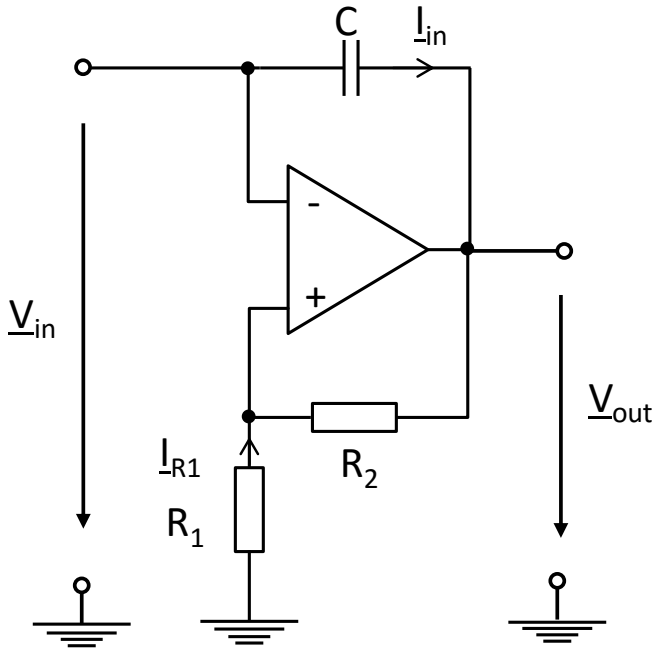

FIGURE 5.8: Negative capacitance converter circuit

The current through R_1 is equal to:

$$\underline{I}_{R_1} = \frac{\underline{V}_{in}}{R_1} \tag{5.10}$$

The output voltage of the amplifier is expressed by:

$$\underline{V}_{out} = \underline{V}_{in} + \underline{I}_{R1} R_2 = (1 + \frac{R_2}{R_1})\underline{V}_{in} \tag{5.11}$$

The current flowing through the capacitance is defined by:

$$\underline{I}_{in} = \frac{\underline{V}_{in} - \underline{V}_{out}}{Z_C} = -\frac{R_2}{R_1}\frac{\underline{V}_{in}}{Z_C} \tag{5.12}$$

Then, the impedance is the following:

$$Z_{NCC} = \frac{\underline{V}_{in}}{\underline{I}_{in}} = -\frac{R_1}{R_2} Z_C \tag{5.13}$$

When the condition $R_1 = R_2$ is fulfilled, we have:

$$Z_{NCC} = -Z_C \tag{5.14}$$

In the Norton equivalent circuit (Figure 5.9), the output current is associated with the output resistance, stray capacitance and capacitance synthesized by NCC.

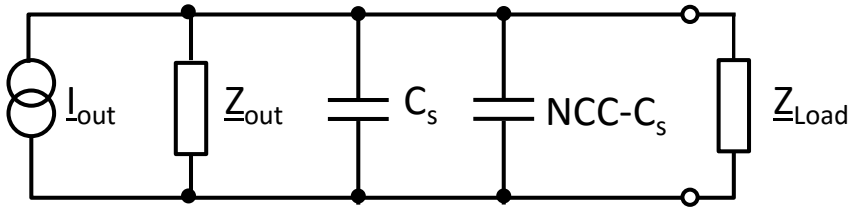

FIGURE 5.9: Norton equivalent circuit of real current source connected to NCC

When NCC capacitance is equal to stray capacitance, the imaginary part of the parallel impedance is zero.

$$Im(Z) = \frac{1}{j\omega C} - \frac{1}{j\omega C} = 0 \tag{5.15}$$

5.2.4 External compensation

Externally compensating operational amplifiers [95] reduce the effects of stray capacitance at the output; increase the gain bandwidth and the slew rate. The adjustable feedback capacitor compensation reduces the noise and provides a flat amplitude response, thereby increasing the performance of current source. In [96], external compensating operational amplifier AD8021 is used in basic Howland current source. In this work, we choose this amplifier for dual configuration Howland circuit in negative feedback which has good accuracy than the single configuration [50]. AD8021 is also compared with uncompensated amplifier AD8041.

5.3 Compensated circuits

The Tietze circuit and the inverting double amplifier are designed with connection to the negative capacitance circuit (Figure 5.10) in order to minimize the stray capacitances effect especially at high frequencies.

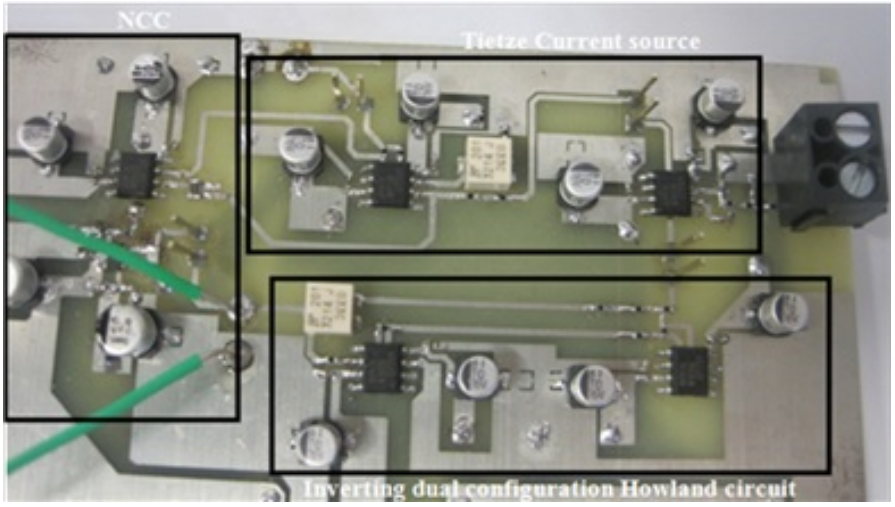

FIGURE 5.10: Current source design with compensation circuit

5.3.1 Tietze circuit with NCC

After connecting Tietze to NCC, the performance at high frequencies is greatly improved but still larger than the dual configuration.

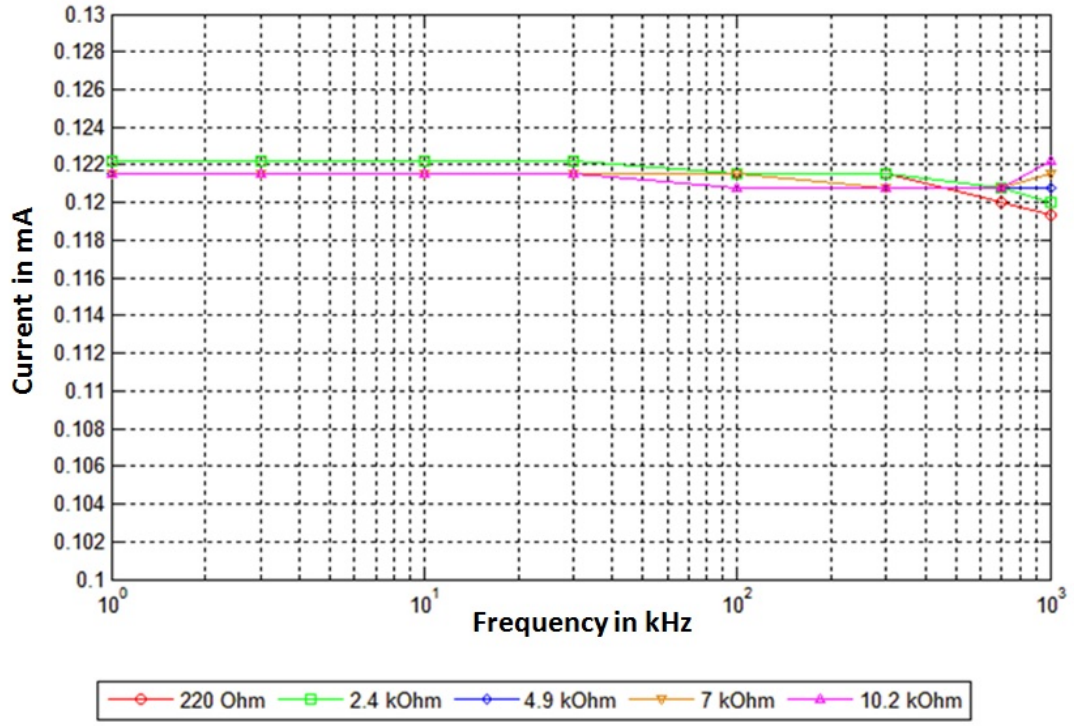

FIGURE 5.11: Experimental results: Tietze circuit connected to NCC [49]

Smallest values of the worst flatness and the error at 1 kHz are not enough to be in our highest rank. This is due to the complexity of the circuit and the high value of the error at 1 MHz which reaches more than 2% (Figure 5.11). The dual configuration with negative feedback is considered as a better current source than Tietze with NCC. It has small errors which are less than 1% both at low and high frequencies. But the flatness is not quite good, nearly 4%. Table 5.1 presents the comparison of the measured flatness and errors for the three tested circuits.

TABLE 5.1: Comparison of experimental results

Circuit	Error (1 kHz)	Error (1 MHz)	Worst Flatness
Inverting dual configuration	0.54%	0.98%	3.99% (220 Ω)
Tietze	0%	14.88%	16.86% (10 kΩ)
Tietze with NCC	0.57%	2.33%	2.33% (220 Ω)

5.3.2 Compensated inverting dual configuration

Using an externally compensated amplifier AD8021 (Figure 5.12), the error becomes slightly lower at 1 kHz around 0.9% than using uncompensated amplifier

AD8041 for which the error reaches 0.98%, while, the error is limited to 0.49% at 1 MHz.

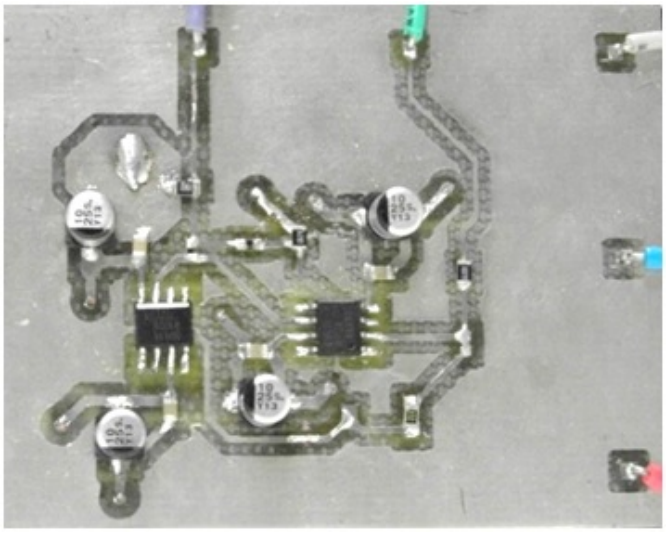

FIGURE 5.12: Experimental results: Tietze circuit connected to NCC [49]

In this study, a high performance Voltage Controlled Current Source (VCCS) for bioimpedance measurement has been estimated and designed. Comparing with previous designs, we have proven that the enhanced Howland circuit in dual configuration with negative feedback using an amplifier with external compensation enables to get better performance. It has the high efficiency with simple structure, accuracy and stability of injected current lower than 0.5 mA even at high frequencies up to 1 MHz with large load up to 10 kΩ which is challenging to get.

5.4 System design of portable bioimpedance device

The impedance measurement procedure consists of exciting the human tissue with a known ac-current, via the voltage controlled current source (VCCS), then measuring the voltage drop across the tissue and calculating the real and imaginary parts of the impedance (Figure 5.13). The advantage thereby is that the excitation signal can be maximized within the medically allowed limit of 0.5 mA [100] to reach a good signal to noise ratio without prior knowledge about the impedance. To get stable and safe injected current, the VCCS has been designed to have high

output impedance and current values within the medically allowed limits in the whole targeted frequency range.

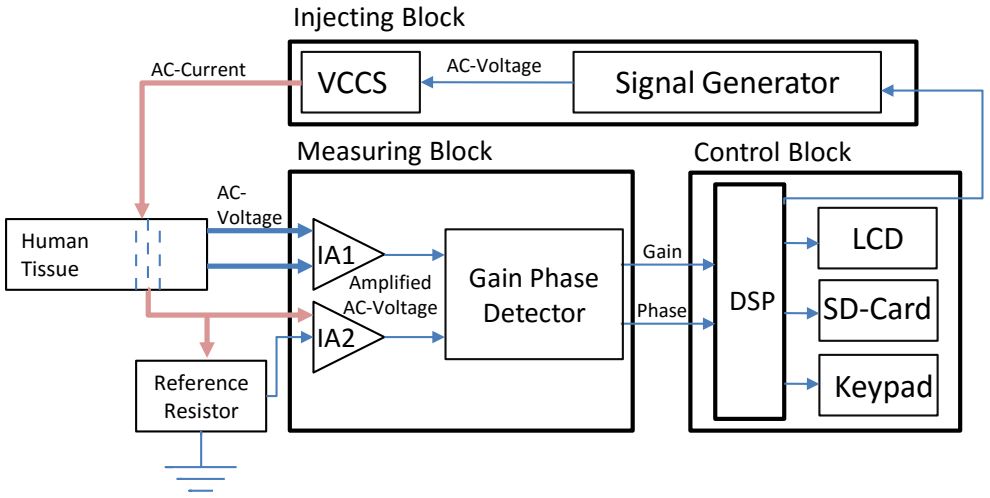

FIGURE 5.13: Block diagram of portable bioimpedance spectrometer [101]

In this section, we show a solution for a hand held bioimpedance spectrometer, which was developed to realize measurements in the frequency range 5 kHz-1 MHz in order to measure the whole range of the β-dispersion for the impedance range from 100 Ω to 10 kΩ. The designed portable bioimpedance spectrometer consists of three major excitation subsystems: excitation, gain and phase measurement and control.

5.4.1 Excitation subsystem

The excitation subsystem includes the designed voltage controlled current source and a multi-frequency signal generator (Figure 5.14). The sine wave is generated by low power programmable waveform generator from Analog Devices AD9834 direct digital synthesizer (DDS) in a frequency range between 1 kHz and 1 MHz with resolution of 0.28 Hz. The output signal from AD9834 is sinusoidal voltage of 600 mV. The output of DDS is sinusoidal AC voltage converted to sinusoidal AC current via VCCS with constant amplitude under 0.5 mA to ensure the patients safety.

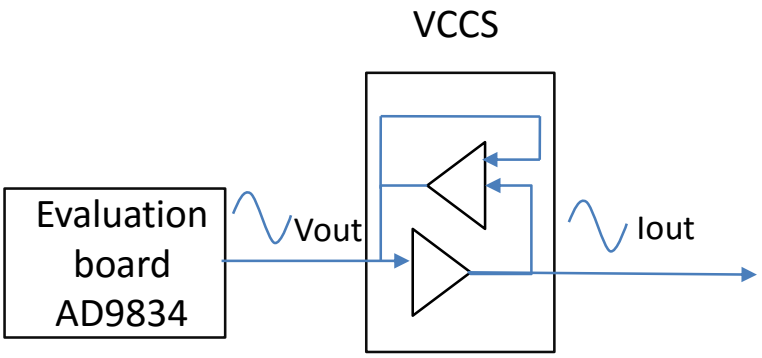

FIGURE 5.14: Block diagram of excitation subsystem [101]

The designed voltage controlled current source is the inverting dual configuration with negative feedback using a compensated amplifier from Analog devices AD8021. It has a low error less than 1% at both low and high frequencies.

5.4.2 Gain and phase measurement subsystem

The excitation signal and the response signals are amplified via two instrumentation amplifiers. To get accurate system and high signal-to-noise ratio, the instrumentation amplifier should have high CMRR and high input impedance. Among many instrumentation amplifiers, we choose INA 163 which has high input impedance (6 M Ω ‖2 pF) and wide frequency bandwidth (800 kHz ‖ G=100). Based on magnitude ratio and phase difference detection method using the integrated circuit AD8302, the impedance is calculated from the gain and the phase extracted by comparison of the amplified excitation and response signals. The output signals for gain and phase from the gain phase detector (AD8302) are sent to the control block for processing.

5.4.3 Control subsystem

The DSP is integrated in a control block, which includes an LCD-Display, keyboard and SD-card (Figure 5.15). It allows the user to select the necessary frequency range, tunes the sine waves generated by the frequency generator, calculates the impedance from the signals of the gain phase detector, displays the results and stores them on SD-card.

FIGURE 5.15: Block diagram of the control subsystem [101]

5.4.3.1 Interfacing the DSP to the sine wave generator AD9834

The AD9834 operates at clock rates up to 40 MHz and is compatible with DSP and microcontroller standards. Connection with external device is ensured using an internal serial interface block which has three inputs:
- SDATA Serial data input: 16-bit serial data-word is applied to this input
- SCLK Serial Clock Input: Data is shifted into the AD9834 on each falling SCLK edge
- FSYNC Active Low Control Input: When FSYNC is taken low, the internal logic is informed that a new word is being loaded into the device

These inputs are connected to any SPI module includes in the DSP such as SDATA connected to SPISIMO Slave In, Master Out, SCLK connected to SPICLK: Clock and FSYNC connected to SPISTE\: Transmissions enable.

The octal buffer 74HCT244 is a digital buffer ensures the interface between DSP and AD9834. In fact Serial Data applied, clock and the transmission enable signals should be buffered before being applied to the serial interface. This Interface between TMS320F2808 and AD9834 is shown in (Figure 5.16) .

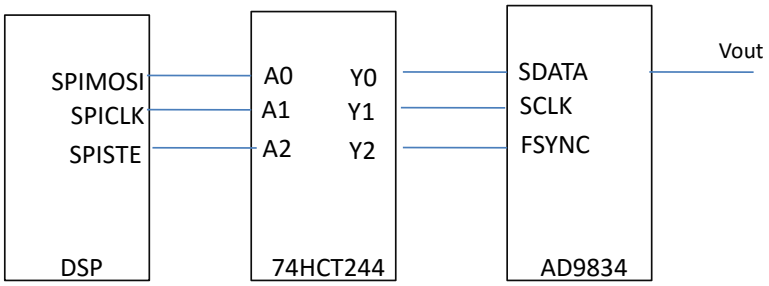

FIGURE 5.16: Interface between TMS320F2808 and AD9834 [101]

5.4.3.2 Interfacing the DSP to the gain phase detector AD8302

AD8302 provides the gain and the phase to the ADC block which converts them from analog to digital form then calculates the impedance value. Pins 13 and 9 of AD8302 output simultaneously the gain and the phase; these two pins are connected to two inputs pins of the ADC block: ADCINA0 and ADCINB0.

The keypad can be interfaced easily to our DSP TMS320F2808 as it doesn't need any particular protocol. Its pins are connected to general purpose GPIO pins. For LCD and SD card, they can use serial peripheral interface (SPI) or parallel (SD) interface to connect to the host. SPI mode is simpler than SD mode which is usually used for high capacity cards, for our application we use SPI mode [102].

At this stage, the portable bioimpedance device is designed and tested respecting the patient safety requirements. The amplitude of the output current of the designed voltage controlled current source (VCCS) is approximately constant in the whole β-dispersion with error low than 1%. For simulations and experiments, the VCCS is converting a sinusoidal AC-voltage to a sinusoidal AC-current.

For real-time application in the medical field, short measurement time and low power consumption are required. For that, a comparative study of different excitation signals and the sine wave signal is detailed in the next chapter.

6. Evaluation of excitation subsystem

The selection of excitation signals is decisive in the design of portable biomedical measurement system given the fact that a suitable signal enables accurate measurement within a given time frame. Different approaches for excitation signals can be considered in bio-impedance spectroscopy measurement systems. One common approach is the frequency sweep based on the measurement of impedance at single frequency and then sweeping defined frequencies over the interesting frequency range. The main advantage of this technique is high impedance measurement accuracy related to a high signal-to-noise ratio, but this takes place at the cost of long measurement time. Even tens of seconds are necessary for a complete sweep [103].

Another approach consists of applying broadband excitation signals to perform the measurement of the impedance at different frequencies simultaneously. This approach is more suitable in biomedical applications, where high real-time measurements are required, but this leads to accuracy losses.

The focus of this chapter is the investigation of excitation signal for portable bio-impedance devices. The excitation signal should provide a high signal-to-noise ratio for accurate measurements, while maintaining low injected currents all over the frequency range and at a short measurement time. In addition to that, the energy consumption of the hardware should be maintained as low as possible.

6.1 Study of the effect of signal's parameters

A detailed study is carried out in order to find suitable parameters that consider the trade-off between the quality of the reconstructed signal reflecting the accuracy of measurements, the time consumption and the hardware complexity related to the memory size of the hardware and the ADC clock.

The number of samples (N) is directly related to the memory's size of the hardware used in the measurement. The sampling frequency (F_s) is associated to the clock and the noise's level is affiliated to the algorithm or the measurement hardware.

In this investigation, a noise is applied to different selected signals, fitting only two variables which are the amplitude (A) and the phase of the signal (ϕ) by varying

in different ways the number of samples (N), the sampling frequency (F_s) and the noise's level in the working conditions. After that, the relative amplitude error is computed using the curve fitting algorithm (Figure 6.1).

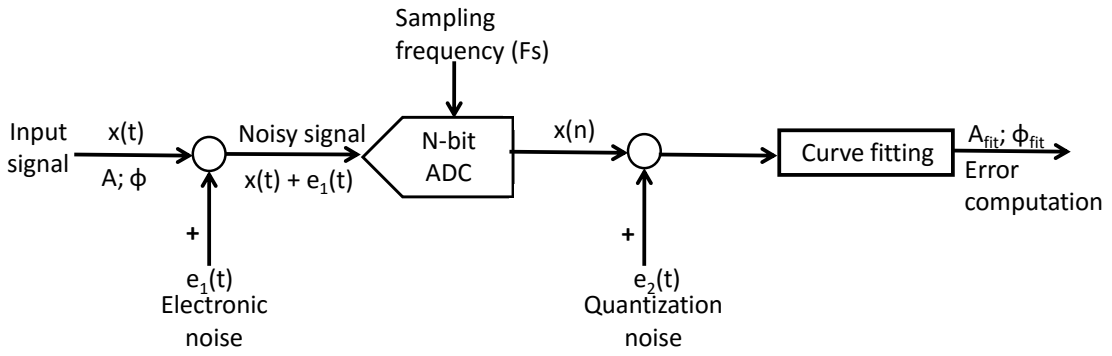

FIGURE 6.1: Relative errors computation

Curve fitting algorithms are used to extract the parameters of the investigated signals in the presence of additive noise and in case of coherent sampling to avoid the leakage effect in frequency domain. In this case, the number of samples M of the signal requires an integer number of cycles. So that, coherent sampling must satisfy the relation presented in equation 6.1:

$$\frac{F_s}{f} = \frac{N}{M} \tag{6.1}$$

where F_s, f, N and M represent respectively the sampling rate, the input frequency, the number of samples and the number of cycles.

The parameters should be carefully selected to fulfill several rules. N should be power of two, as it is necessary for a convenient FFT computation. Besides, the number of cycles M should be an odd integer number to avoid spectral leakage. Moreover, M and N should be mutually prime to achieve non repetitive number of cycles as it is non useful and produce processing overhead [104]. The M data points of a signal are given by equation 6.2.

$$y_i = \sum_{k=1}^{N} A_k \sin(2\pi\, f_k t + \varphi_k) \tag{6.2}$$

where N, A_i, f_i and ϕ_i denote respectively the number of signal components, the fundamental amplitudes, the frequencies and phases. Equation 6.2 can be rewritten as a sum of sine and cosine (equation 6.3)

$$y_i = \sum_{k=1}^{N} a_k \cos(2\pi\, f_k t_i) + b_k \sin(2\pi\, f_k t_i) \tag{6.3}$$

Thus, a_k and b_k are easily obtained by solving the formula 6.4 [105]:

$$X = (D^T D)^{-1} D^T Y \tag{6.4}$$

$$D = \begin{pmatrix} \cos(2\pi\, f_1 t_1) & \sin(2\pi\, f_1 t_1) & ... & \cos(2\pi\, f_N t_1) & \sin(2\pi\, f_N t_1) \\ \cos(2\pi\, f_1 t_2) & \sin(2\pi\, f_1 t_2) & ... & \cos(2\pi\, f_N t_2) & \sin(2\pi\, f_N t_2) \\ \vdots & \vdots & \vdots & \vdots & \vdots \\ \cos(2\pi\, f_1 t_n) & \sin(2\pi\, f_1 t_n) & ... & \cos(2\pi\, f_N t_n) & \sin(2\pi\, f_N t_n) \end{pmatrix} \tag{6.5}$$

The estimated amplitudes and the corresponding relative amplitude errors are defined as:

$$A_{kfit} = \sqrt{a_k^2 + b_k^2} \tag{6.6}$$

$$\epsilon_{A_k} = \frac{\|A_k - A_{kfit}\|}{A_k} \tag{6.7}$$

Simulations of the amplitude errors of different excitation signals are presented. The cases studies in this thesis are the sine wave, chirp and multisine signals. For that, the influence of the signal parameters are studied when only one parameter is fixed and the other parameters are variables. In this study, the maximum input frequency is fixed at 1 MHz.

6.1.1 Investigation of the influence of the sampling frequency versus the samples number

In the third investigation, the noise's level SNR is fixed at 100 dB and the sampling frequency and the number of samples are variable. The sampling frequency is varied from 2f to 10^6f as the lowest sampling frequency must be selected twice the bandwidth respecting to Shannon theorem. The number of samples is chosen between 32 and 16384.

6.1.1.1 Sine wave

For each number of samples and for every input signal, Figure 6.2 depicts that the amplitude error is almost constant until a threshold value of F_s/f, and then an increasing error level is obtained.

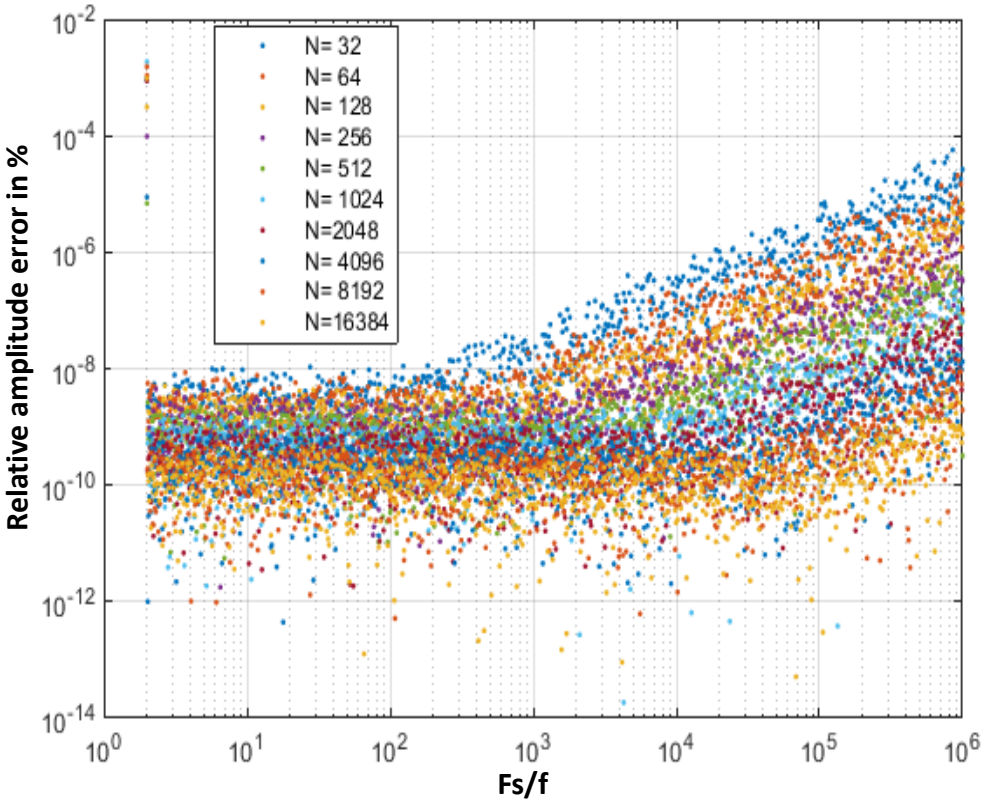

FIGURE 6.2: Relative amplitude error of sine signal depending upon number of samples and sampling rate

This is due to the fact that the acquisition time is too short to provide a sufficient excitation energy results with a bad signal-to-noise ratio. In this case, the acquisition time (T) is under 0.08192 μs. So that higher values of the sampling rate (oversampling) are not preferable as it leads to increase the amplitude error. In addition to that oversampling results in high energy consumption and requires more expensive ADC.
Regardless the value of the input frequency f varying from 1 kHz to 1 MHz, we obtain same results (Figure 6.2) which are summarized in Table 6.1.

TABLE 6.1: Number of samples N versus F_s/f and acquisition time T

Number of samples (N)	F_s/f	Acquisition time (μs)
32 <N<64	2 <F_s/f <100	0.32 <T <0.64
128 <N<512	2 <F_s/f<1000	0.13 <T <0.51
1024 <N<4096	2 <F_s/f <10000	0.10 <T <0.41
8192 <N<16384	2 <F_s/f <100000	0.08 <T<0.17

Choosing N that belongs to the interval [1024, 4096] is the adequate value as it represents the minimum number of samples permitting the coverage of the whole bandwidth. Adding to that, increasing the number of samples is too memory consuming resulting in high data acquisition time. For that reason, $N = 1024$ is sufficiently high in this study.
Consequently, taking the example of signal's frequency in the boundaries of the frequency range interval, we obtain the following relations:

$$If\ f = 1kHz,\ 2kHz < F_s < 10\,MHz \tag{6.8}$$

$$If\ f = 1\,MHz,\ 2\,MHz < F_s < 10\,GHz \tag{6.9}$$

From the above results, we can conclude that F_s equals to 10 MHz is sufficient for the both frequencies input. To avoid spectral leakage in the frequency domain, coherent sampling is required using equation 6.1. For f = 1 MHz and $N = 1024$, we obtain:

$$M = \frac{fN}{F_s} = 102.4 \tag{6.10}$$

Where M is not an odd integer. By forcing M to meet the rule given in the beginning of the section, M becomes equal to 101 which results in sampling rate (F_s) nearly equals to 10.139 f and an acquisition time $T = N/F_s = 0.101$ ms for one frequency measurement.

6.1.1.2 Chirp signal

Almost the same relative amplitude errors are provided for the sine and the chirp waveforms (Figure 6.3 in comparison to Figure 6.2). The difference is only restricted to the presence of higher errors at the Nyquist frequency in the sine wave that don't figure in the case of the chirp signal.

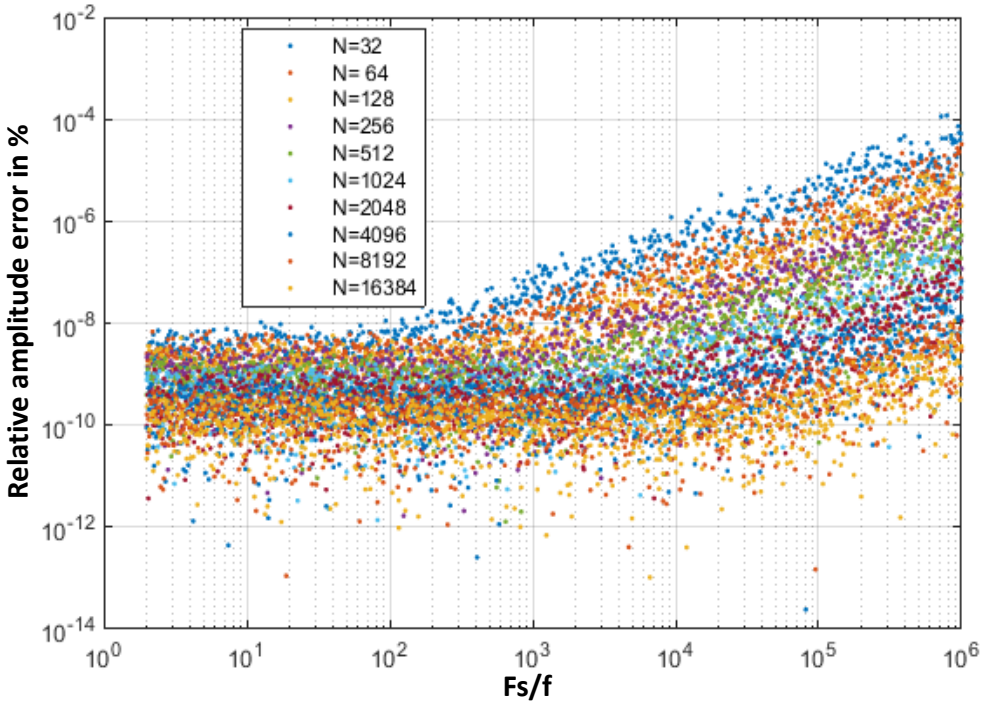

FIGURE 6.3: Relative amplitude error of the chirp signal depending upon the number of samples and the sampling rate

The errors are generally relative low. Taking the example of the worst case ($N = 32$), the error is typically the same nearly to 10^{-8} starting from the Nyquist frequency up to 100 times the signal's frequency after that the error increases which attains maximum amplitude error nearly equal to 10^{-4}. Taking into consideration that increasing the number of samples is memory consuming in addition to that high sampling rate needs more power consumption and costly ADC. Choosing $N = 1024$ and $F_s = 10.139f$ is convenient allowing a high accuracy of the measurement (amplitude error about 10^{-8}) as it is illustrated in Figure 6.5 and in a short acquisition time less than 2 ms ($T = N/F_s$ =0.101 ms) during the whole frequency band.

6.1.1.3 Multisine signal

The two previous signals are not very sensitive to noise compared to the multisine especially for higher sampling rate. Figure 6.4 shows that for $N = 32$ the amplitude error is constant nearly to 10^{-8} when the sampling rate is varying from the Nyquist frequency to 20 times the frequency's signal.

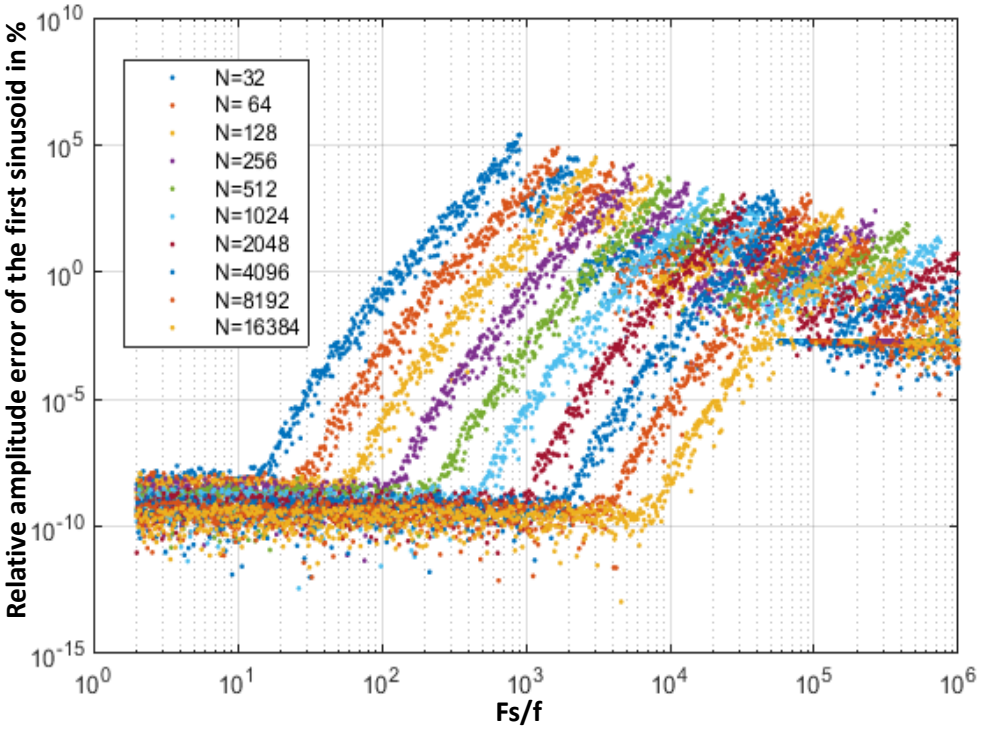

FIGURE 6.4: Relative amplitude error of multisine signal depending upon number of the samples and the sampling rate

The generation of multisine is based on the summation of four sine signals with zero phases and frequencies f_k = k f_{k-1} (k= 1...4), the fundamental frequency f_1 is set at 0.25 MHz. As well as in the sine signal and the chirp, the sampling rate (F_s) equals to 10.139 f_4 Hz is adequate for our application. Besides, based on coherent sampling F_s/f_4 =N/M and for the same number of cycles M (M=101), the number of samples (N) becomes equivalent to 4096. In this situation ($F_s = 10.139 x f_4$; N = 4096), accurate measurements can be achieved in a short time (T = 0.404 ms) since the amplitude error is around 10^{-9}.

6.1.2 Investigation of the influence of the samples

In this investigation, the sampling frequency is fixed and the number of samples and the noise level are variable. Same results are provided for the sine (Figure 6.5(a)) and the chirp (Figure 6.5(b)). However, the relative amplitude error considered in the multisine (Figure 6.5(c)) is high for too short number of samples (N<20). For higher number of samples, the multisine follows the same behavior illustrated in sine and chirp signal.

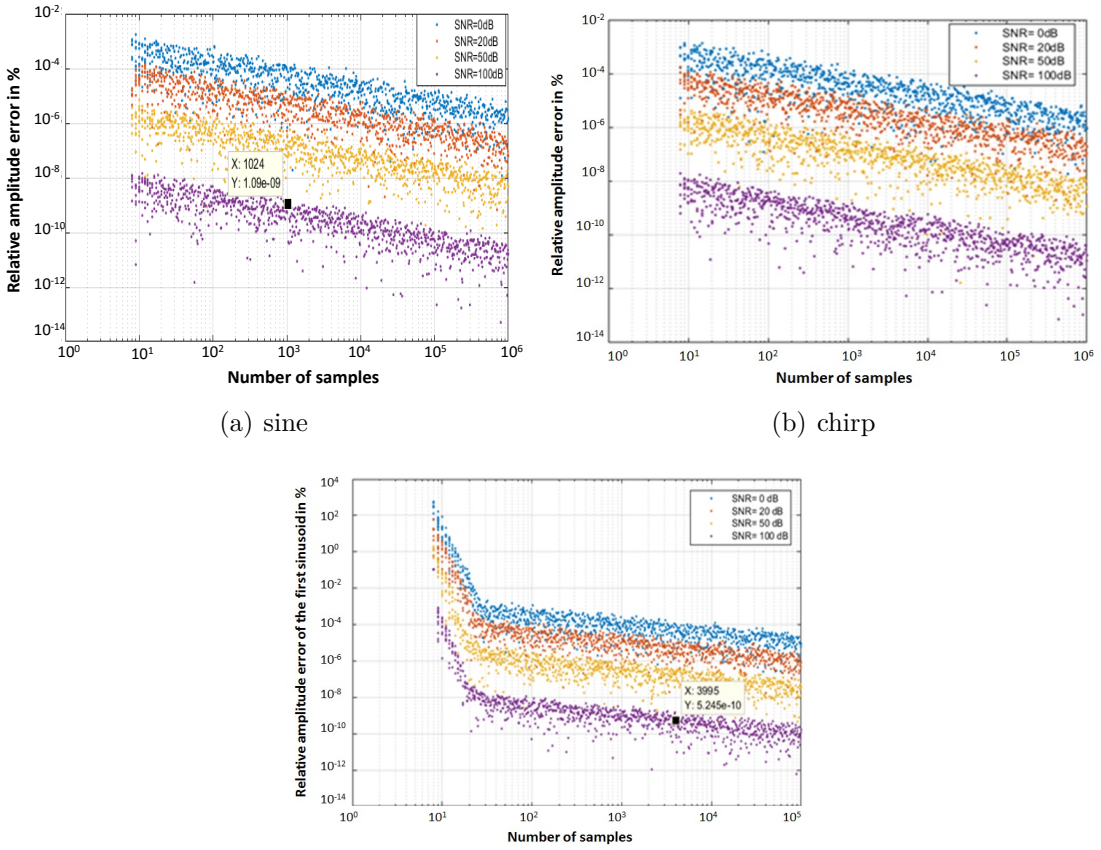

(a) sine

(b) chirp

(c) multisine

FIGURE 6.5: Relative amplitude error depending upon number of samples

Figure 6.5 shows that when increasing the number of samples, the relative error is minimized. Therefore, extending the number of samples is strongly recommended as it reduces the effect of noise resulting in high SNR output, necessary for high accuracy of measurement.

Concerning the measurement time, we fix the same SNR output for a relative error close to 10^{-9}, as an example. In this case, the measurement time at once frequency is approximately four times smaller ($N = 1024$) for the stepped sine compared with multisine measurement ($N = 3884$). However, for a single sine measurement, four measurements should be considered successively. Hence, the same measurement time is obtained. In contrast to the chirp signal in which all information are captured at once measurement, it provides the lowest measurement time, since the given SNR output is reached at $N = 1024$.

6.1.3 Investigation of the influence of the sampling frequency number

In this investigation, different levels of noise are applied to the sine, chirp and multisine signals, when varying the sampling rate and the number of samples is fixed at 1024. Figure 6.6 depicts that when increasing the SNR, the relative errors decreases. Therefore, higher SNR is preferred to obtain accurate impedance spectrum.

The relative amplitude error is approximately the same for each signal filled by the same level of noise at low sampling rate: errors are almost constant and become higher beyond a threshold value of F_s/f (Figure 6.6).

The threshold value corresponds to the lowest acquisition time allowing a high SNR. The acquisition time for the chirp and the multisine are equal to 0.1024 μs and 2.048 μs, respectively. Therefore, the chirp is considered the most appropriate signal that provides the high SNR output in a short measurement time.
In the next section, the signal's frequency f, the sampling frequency F_s and the number of samples N are fixed at 1 MHz, 10.14 x f and 1024, respectively.

6.2 Influence of noise in signals specifications

A comparative study of various kinds of periodic signals across a load of 1 kΩ is presented based on average power, energy efficiency and power spectral density spectrum permitting the evaluation of the amount of energy concentrated in the

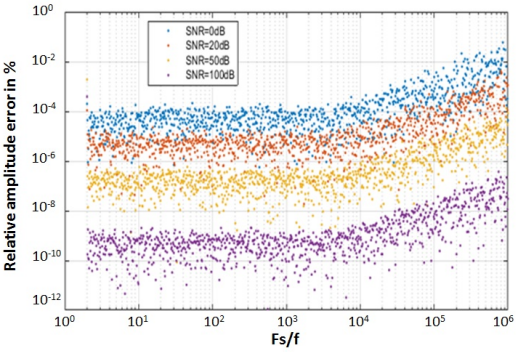

(a) sine

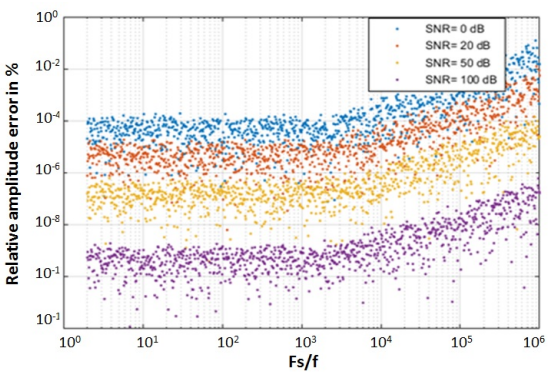

(b) chirp

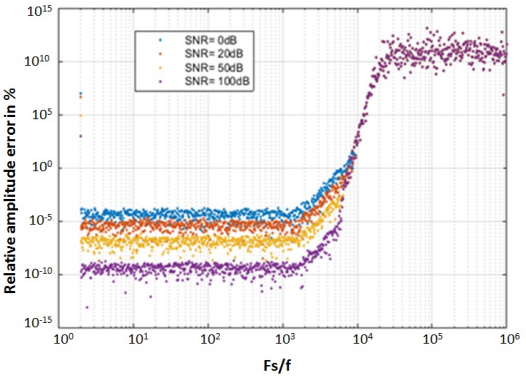

(c) multisine

FIGURE 6.6: Relative amplitude error depending upon sampling rate and various SNR

frequency band of interest and those fell outside. The power distributions of selected signals in the frequency domain are estimated by the Periodogram method. Analyses are made without and with an applied Gaussian white disturbance to study the sensitivity of selected signals to the noise. Three different levels of the noise have been taken into examination: SNR = 100 dB, SNR = 20 dB and SNR = 0 dB. For SNR = 100 dB, it is considered as no noise is applied and the worst case (very noisy signal) is given for SNR = 0 dB.

6.2.1 Sine wave

One of the most frequently applied techniques in impedance spectrum measurement is based on the sine wave signal. Its mathematical function used in our analysis is given by:

$$u(t) = A\sin(2\pi\, ft) \tag{6.11}$$

As the sine signal is a periodic signal with amplitude A = 600 mV and M=101 periods T, the total energy is given by:

$$E = \frac{1}{R}\int_{-MT}^{MT} |u(t)|^2\, dt = \frac{1}{2R}\int_{-MT}^{MT} |A\sin(2\pi\, ft)|^2 = \frac{A^2}{TR}\int_0^{MT} \frac{1-\cos(4\pi\, ft)}{2} \tag{6.12}$$

$$Thus, E = MT\frac{A^2}{2R} = 1.818\,10^{-8} J \tag{6.13}$$

The average power over 1 kΩ load is expressed as follow:

$$P_{avg} = \frac{E}{MT} = \frac{1}{2MTR}\int_{-MT}^{MT} |A\sin(2\pi\, ft)|^2 = \frac{A^2}{MT}\int_0^{MT} \frac{1-\cos(4\pi\, ft)}{2} = \frac{A^2}{2R} \tag{6.14}$$

$$P_{avg} = 1.8\,10^{-4}\, Watts \tag{6.15}$$

The PSD is calculated as:

$$PSD(f) = \frac{N|X(f)|^2}{RB_{FFT}} = \frac{MA^2}{2fR} = 0.0182\,\mu W/Hz \tag{6.16}$$

Where $|X(f)|$ is the Fourier transform of the signal; $B_{FFT} = \mathrm{N}\Delta\mathrm{f}$ is the bandwidth; N is the number of frequency bins, and $\Delta\mathrm{f} = F_s/\mathrm{N}$ is the frequency resolution. Figure 6.7 shows that the spectrum of the sine wave is discrete: the whole signal energy is concentrated in the frequency component f at 1 MHz. The amplitude of PSD is equal to 0.0182 μW/Hz (Figure 6.7) which coincides exactly with the calculated one (equation 6.13).

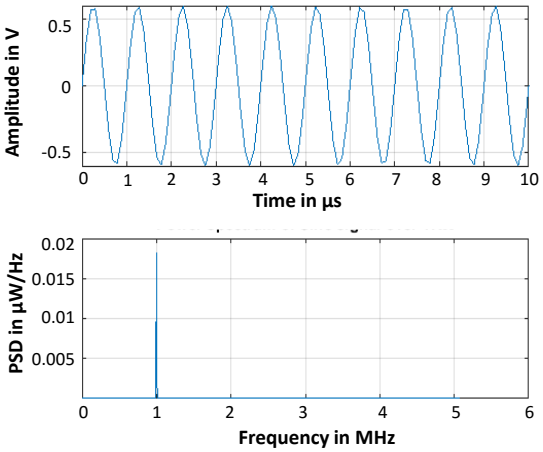

(a) without noise

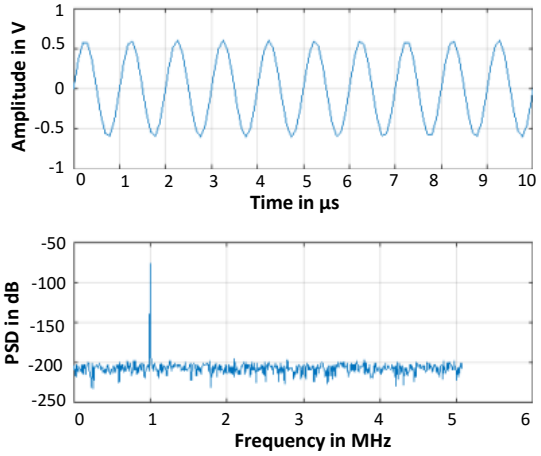

(b) $SNR = 100dB$

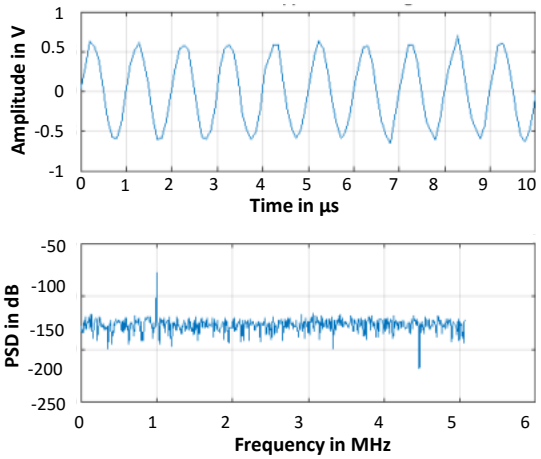

(c) $SNR = 20dB$

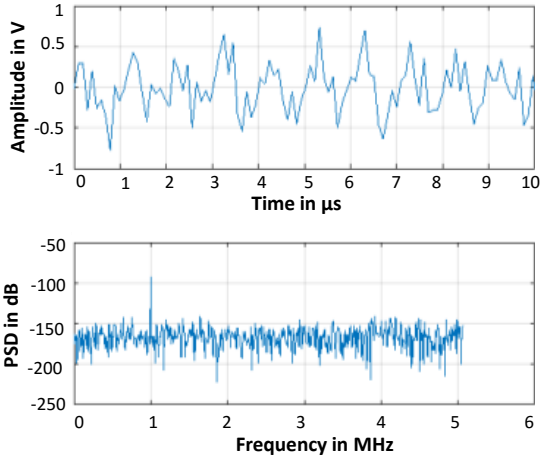

(d) $SNR = 0dB$

FIGURE 6.7: Sine wave signal and its power spectral density

Hence, the sine wave represents a high energy efficiency resulting in high accuracy impedance measurements. However, the main disadvantage of a sine wave is the long measurement time required when sweeping all over the frequency range. When the level of noise is decreasing (Figure 6.7 (b), (c), (d)), the spectrum becomes more fluctuated and less efficient; only 56% of the useful energy is focused on frequency range.

6.2.2 Binary signal

The binary signal is defined by the above mathematical function:

$$u(t) = \begin{cases} A, & 0 < t < \frac{T}{2} \\ -A, & \frac{T}{2} < t < T \end{cases} \tag{6.17}$$

The energy of binary signal wit M = 101 periods T is expressed as:

$$E = \frac{1}{R}\int_{-MT}^{MT} |u(t)|^2\, dt = \frac{1}{R}(\int_0^{\frac{MT}{2}} A^2 dt + \int_{\frac{MT}{2}}^{MT} (-A)^2 dt) = 0.03632\,\mu J \tag{6.18}$$

A periodic signal can be represented by a combination of sine and cosine functions as expressed in the trigonometric Fourier series:

$$u(t) = \sum_{n=-\infty}^{\infty} c_n e^{j2\pi\, ft} = a_0 + \sum_{n=1}^{\infty} a_n \cos(\omega_0 t) + b_n \sin(\omega_0 t) \tag{6.19}$$

$$a_n = \frac{2}{T}\int_0^T u(t)\cos(n\omega_0 t) \tag{6.20}$$

$$b_n = \frac{2}{T}\int_0^T u(t)\sin(n\omega_0 t) \tag{6.21}$$

Where T is the period, ω_0=2πf; f is the fundamental frequency and the average or DC component of the signal is:

$$a_0 = \frac{2}{T}\int_0^T u(t)dt \tag{6.22}$$

The binary signal is odd, then $a_0 = a_n = 0$

$$x(t) = \sum_{n=1}^{\infty} b_n \sin(n\omega_0 t) = \sum_{n=1}^{\infty} \frac{4A}{n\pi} \sin(n\omega_0 t) \tag{6.23}$$

Where n is odd According to Paserval's theorem, the average power of a periodic signal over 1 kΩ load R is the sum of the average power of its frequency components.

$$P_{avg} = \frac{1}{MTR} \int_T |u(t)|^2 \, dt = \frac{1}{R} \sum_{n=-\infty}^{\infty} |c_n|^2 \tag{6.24}$$

Hence, the average power for binary signal over 1 kΩ resistor R is given by:

$$P_{avg} = \frac{1}{R} \sum_{n=1}^{\infty} \frac{b_n^2}{2} = \frac{1}{R} \left(\frac{(\frac{4A}{n\pi})^2}{2} + \frac{(\frac{4A}{\pi})^2)}{2} + \frac{(\frac{4A}{3\pi})^2}{2} + \frac{(\frac{4A}{5\pi})^2}{2} + ... \right) \tag{6.25}$$

Equivalently to:

$$P_{avg} = \frac{1}{MTR} \left(\int_0^{\frac{MT}{2}} A^2 dt + \int_{\frac{MT}{2}}^{MT} (-A^2) dt \right) = \frac{A^2}{R} \tag{6.26}$$

The average power of the fundamental frequency harmonic is:

$$P_0 = \frac{(\frac{4A}{\pi})^2}{2R} \tag{6.27}$$

and for higher harmonics, it is given by:

$$P_n = \frac{(\frac{4A}{n\pi})^2}{2R} \tag{6.28}$$

Table 6.2 summarizes the value and the percentage of power distributed in each frequency component of binary signal.

TABLE 6.2: Power distribution of binary signal

Frequency components	Power(mW)	Percentage (%)
Fundamental	0.292	81.057
First harmonic	0.032	9.006
Second harmonic	0.011	3.242
Third Harmonic	0.006	1.654
Total power	0.341	95%

The PSD of the fundamental frequency is calculated as:

$$PSD_1(f) = \frac{MP_0}{f} = \frac{(\frac{4A}{\pi})^2}{2Rf} = 0.02929\,\mu W/Hz \tag{6.29}$$

The PSD of every nth higher odd harmonic (n=3, 5, 7, ...) is equal to:

$$PSD_n(f) = \frac{MP_n}{f} \tag{6.30}$$

In this study, the chosen amplitude A is 600 mV, which leads to an average power approximately equals to 0.36 mW. Table 6.2 shows that approximately 80% of the average power is concentrated in the desired frequency due to the higher harmonics. Binary signal has lower energy efficiency and higher power around 0.36 10^{-3}W can be injected in the system under test comparing to 0.18 10^{-3}W in case of sine wave signal.

Further advantage of binary signal is that it has unity crest factor allowing the generation of accurate impedance spectrum and the simplicity of generation. The same inconvenient of long measurement time of sine wave is presented also in binary signal.
Figure 6.8(b) shows that the energy is focused on the fundamental frequency and a part of it is spread between higher harmonics. The spectrum becomes more fluctuated when more level of noises are used (Figure 6.8(c)) especially in the worst case (Figure 6.8(d)). This leads to a poor impedance spectrum results.

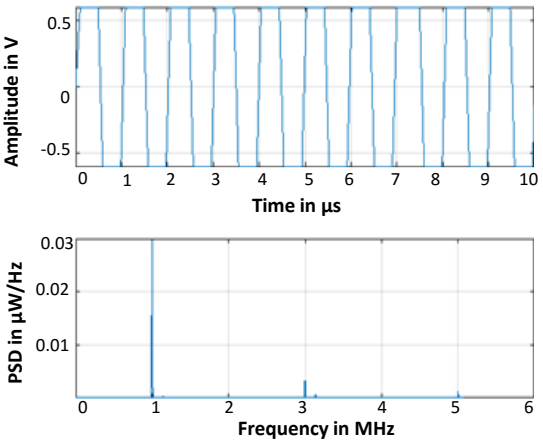

(a) without noise

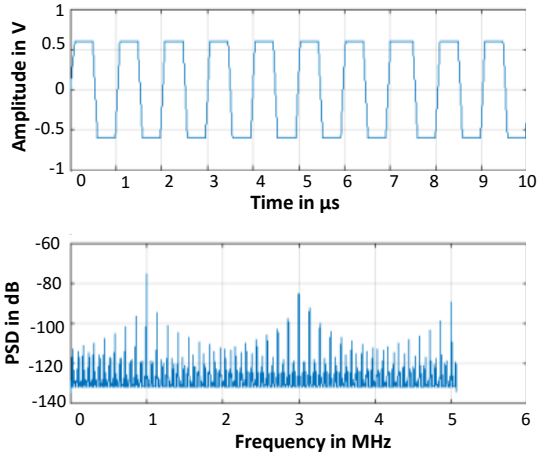

(b) $SNR = 100dB$

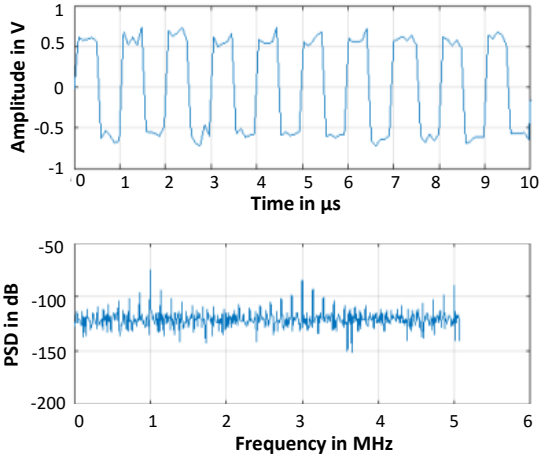

(c) $SNR = 20dB$

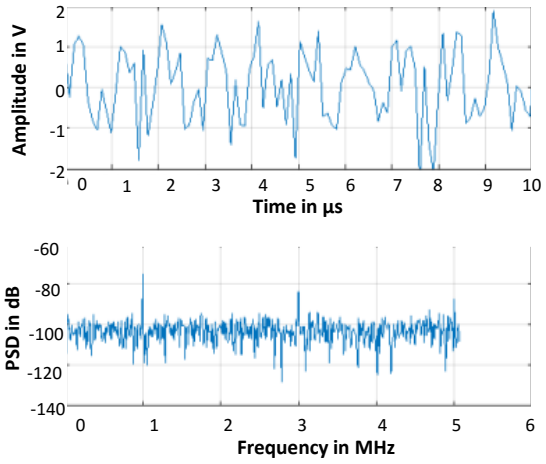

(d) $SNR = 0dB$

FIGURE 6.8: Binary signal and its power spectral density

6.2.3 Linear chirp

The linear chirp has an instantaneous frequency ω(t)= dθ(t)/dt, which changes linearly during the excitation interval T_{ch}. The mathematical model of linear sine chirp is as following:

$$u(t) = A\sin(2\pi(f_0 t + \frac{(f_{fin} - f_0)t^2}{2T_{ch}})) \tag{6.31}$$

Where f_0 and f_{fin} are the initial and the final frequency, respectively.
The energy E and the average power P_{avg} of linear chirp over 1 kΩ load R in the time domain can be written as:

$$E = \frac{1}{R}\int_0^{T_{ch}} u(t)^2 dt = \frac{1}{R}A^2 \int_0^{T_{ch}} \frac{1 - \cos(4\pi(f_0 t + \frac{(ff_{in} - f_0)t^2}{2T_{ch}}))}{2} dt = 0.017736\,\mu J \tag{6.32}$$

$$P_{avg} = \frac{1}{T_{ch}R}\int_0^{T_{ch}} u(t)^2 dt = \frac{A^2}{2R} = 0.18\,10^{-3} W \tag{6.33}$$

$$T_{ch} = \frac{2L}{f_0 + f_{fin}} = \frac{N}{F_s} \tag{6.34}$$

The energy efficiency of linear sine-wave chirp is computed based on equation (2.14), it is nearly equal to 98.85% The frequency bandwidth is fixed to B_{exc}=f_{fin} -f_0 = 0.999 MHz with f_{fin} = 1 MHz, f_0 = 1 kHz and the sampling frequency F_s is fixed at 10.14 x f_{fin}. Since the number of samples is chosen to be equal to 1024, the number of cycles L is set at 50.551, according to the coherent sampling formula.

Figure 6.9(a) depicts the spectral energy S focused in band of frequency. The spectrum is continuous: almost the entire energy remains in the frequency band of interest 0.999MHz. The level of PSD in the desired frequency is fluctuating around 1.8 10^{-4} μWHz which is almost the average power over the frequency bandwidth. In case of high SNR, the spectrum is flat and becomes more fluctuated as we increase the noise level. Despite of the high energy efficiency, this kind of signal presents several drawbacks. The poor flatness of the power spectrum may cause the loss of accuracy of the impedance measurements.

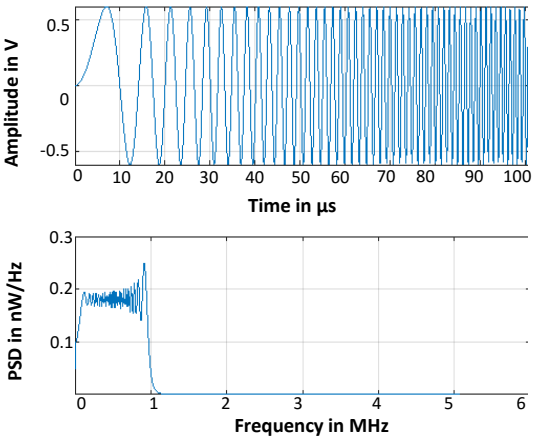

(a) without noise

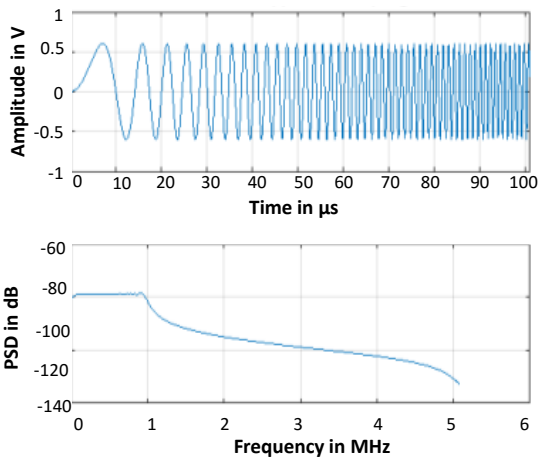

(b) $SNR = 100dB$

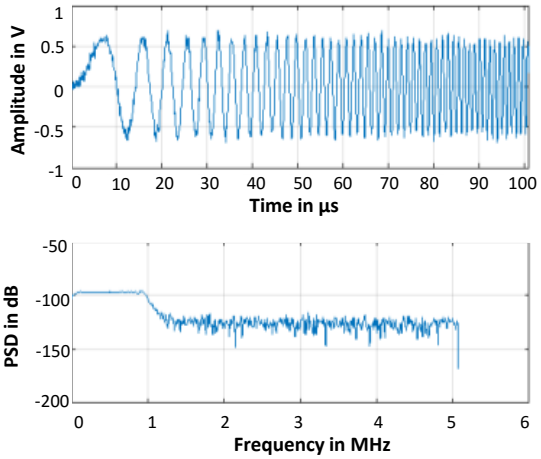

(c) $SNR = 20dB$

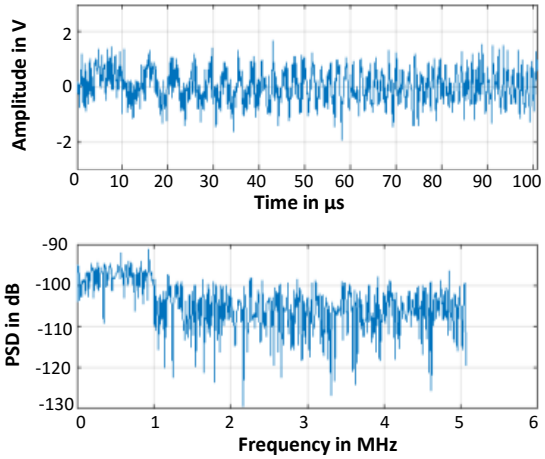

(d) $SNR = 0dB$

FIGURE 6.9: Linear chirp signal and its power spectral density

6.2.4 Signum chirp

As well as in the sine wave chirp, the frequency bandwidth Bexc is set at 0.999 MHz; the sampling rate F_s at 10.14 x f_{fin} MHz and L is equal to 50.551. The average power of the signum-chirp is given by:

$$P_{avg} = \frac{A^2}{R} \tag{6.35}$$

The power spectral density spectrum shows that the level of power is decreasing gradually by plateaus h (Figure 6.10), in fact the power of the fundamental harmonic of rectangular signal over 1 kΩ load as mentioned previously is:

$$P_0 = \frac{(\frac{4A}{\pi})^2}{2R} \tag{6.36}$$

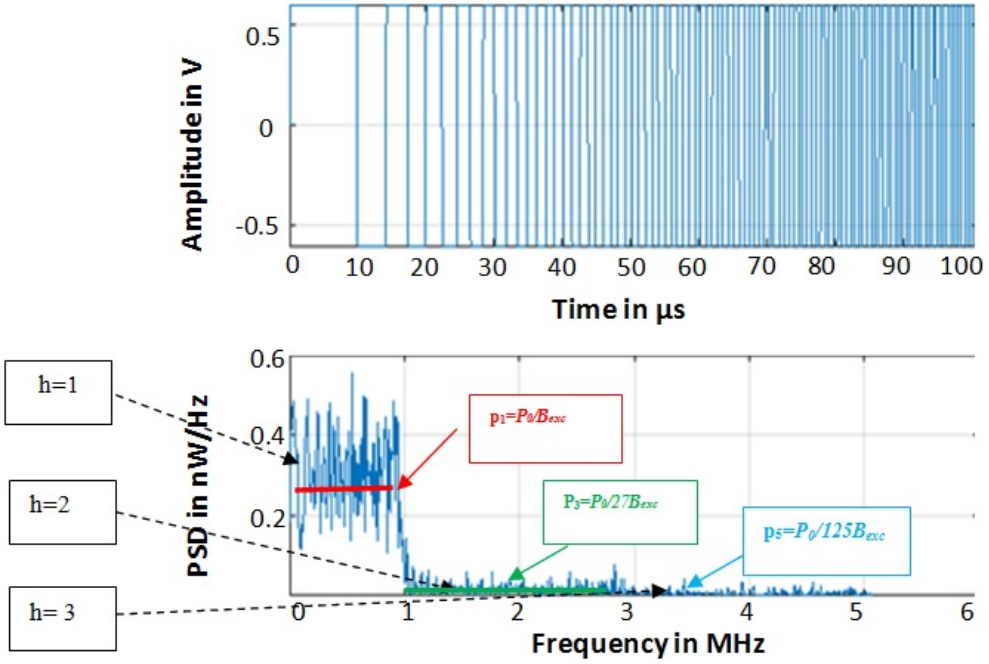

FIGURE 6.10: Signum-chirp wave and its power spectrum

Consequently the PSD of the fundamental harmonics of rectangular-wave chirps from f_0 to f_{fin} is $p_1 = P_1/B_{exc}$ W/Hz. The PSD of every k^{th} higher odd harmonic (k=3, 5, 7...) distributed in the frequency band B_{exc}= k x B_{exc} is defined as:

$$p_1 = \frac{P_0}{k^3 B_{exc}} \tag{6.37}$$

For the first plateau, the PSD is expressed as

$$P_{psd1} = \sum_{k=1}^{\infty} p_k = p_1 + p_3 + p_5 + p_7 + ... \tag{6.38}$$

For every next level (h>1), the PSD is expressed as:

$$P_{psdh} = \sum_{k=h}^{\infty} p_k = p_3 + p_5 + p_7 + ... \tag{6.39}$$

In addition to the simplicity of the signal processing, the binary chirp has the unity crest factor which leads to major power about 0.36 mW injected in the system compared to 0.18 mW for the sine wave chirp of the same length. By applying the formula (2.14), the energy efficiency is nearly equal to 82.52%. The major drawback is the poor aspects of power spectrum due to the higher harmonics.

For both cases where $SNR = 100dB$ (Figure 6.11(b)) and $SNR = 20\,dB$ (Figure 6.11(c)), the power spectrum is practically the same that differ from the linear chirp signal at additional harmonics out the desired frequency band. In case of low level of SNR (Figure 6.11(d)), the spectrum is not flat which reflects a high sensitivity to noise of this signal especially for lower values of SNR.

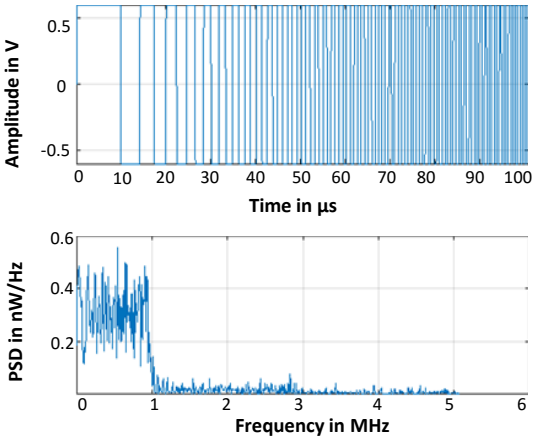

(a) without noise

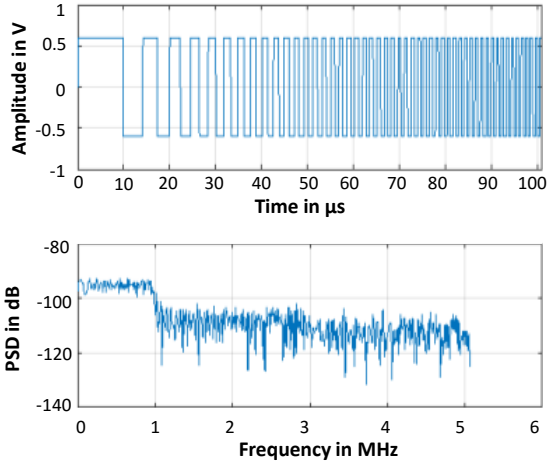

(b) $SNR = 100dB$

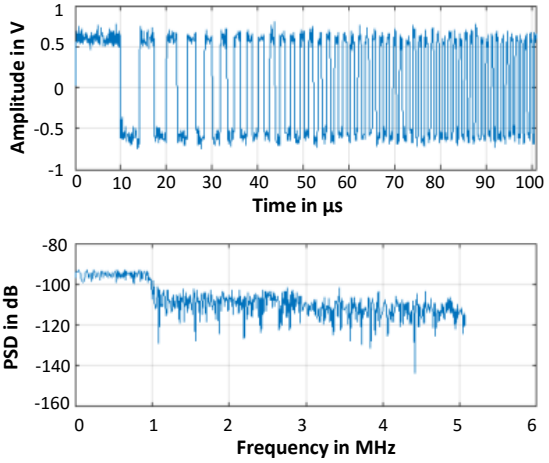

(c) $SNR = 20dB$

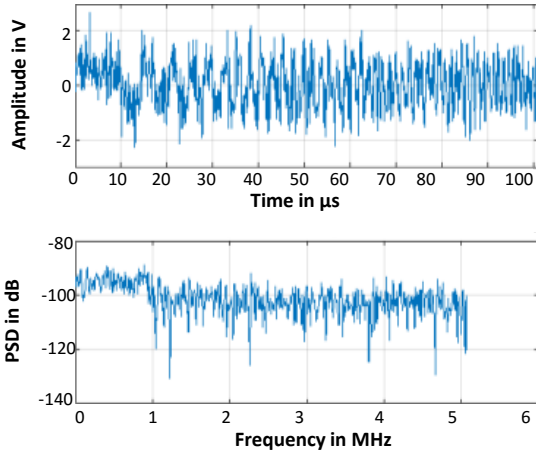

(d) $SNR = 0dB$

FIGURE 6.11: Signum chirp and its power spectral density

6.2.5 Multisine Signal

The multisine is defined as the addition of N sine waves with the same amplitude which leads to an increase of the excitation amplitude. Therefore, we multiply it by a factor of 1/N to obtain a resulting level limited to 600 mV (a threshold in this study).

The energy E of a periodic multisine signal [0, T] can be obtained by solving the following expression

$$E = \int_0^T \left| \sum_{n=0}^{N-1} A_n \sin(2\pi\, f_n t) \right|^2 dt = \int_0^T \sum_{n=0}^{N-1} A_n^2 \frac{(1 - \cos(4\pi\, f_n t))}{2} dt \tag{6.40}$$

The summation operator can be moved out of the integral operator

$$E = \sum_{n=0}^{N-1} A_n^2 [\frac{T}{2} - \int_0^T \frac{cos(4\pi\, f_n t))}{2} dt] = \sum_{n=0}^{N-1} A_n^2 [\frac{T}{2} - \frac{1}{\frac{4\pi\, f_n}{2}} \int_0^T \sin(4\pi\, f_n t) dt] \tag{6.41}$$

Finally, the energy of multisine waveform is obtained

$$E = \sum_{n=0}^{N-1} A_n^2 \frac{T}{2} \tag{6.42}$$

Hence, the average power (P_{avg}) across 1 kΩ load and the crest factor (CF) can be expressed respectively as:

$$P_{avg} = \sum_{n=0}^{N-1} A_n^2 \frac{T}{2R} \tag{6.43}$$

$$CF = \frac{t\epsilon[0\,T] max\,|u(t)|}{\sqrt{\int_0^T \sum_{n=0}^{N-1} \frac{A_n^2}{2}}} \tag{6.44}$$

Therefore, the energy E depends only on the number of frequency components N and the amplitude A_n. For that reason, several modifications of multisine parameters are applied such as the frequency distributions and the number of sine waves components N [106] to evaluate its effect on the multisine behavior.

The phase is set at zero, as it is the simplest case that gives acceptable results comparing to the optimized phase [37]. The sampling frequency is 10.1386 x f_k (f_k is the highest frequency) and we modify the distributions of frequencies as follows [107]:

- Equally spaced distributions of frequencies: f_1 =1 kHz; f_i = i x f_1; (i=1, 2, . . . , 8)
- Binary distributions of frequencies: f_i = i x f_1 with f_1 = 210 kHz; (i=1, 2, . . . , 8)
- Decimal distributions of frequencies:f_1 = 1000 kHz, f_i = i x f_1 (i=1, 10, 100, 1000)

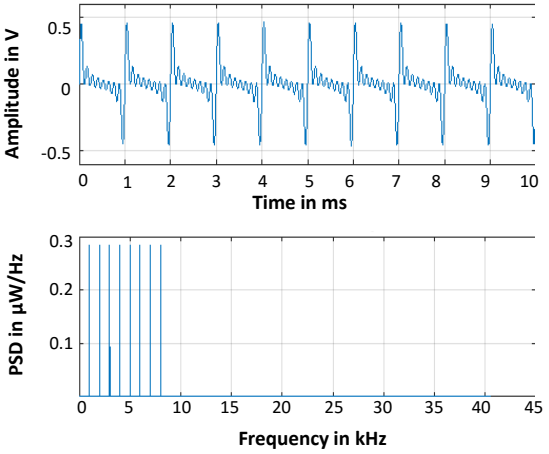

(a) Equally spaced distribution

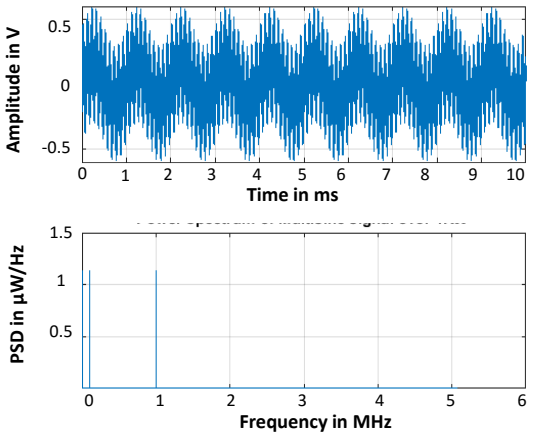

(b) Binary distribution

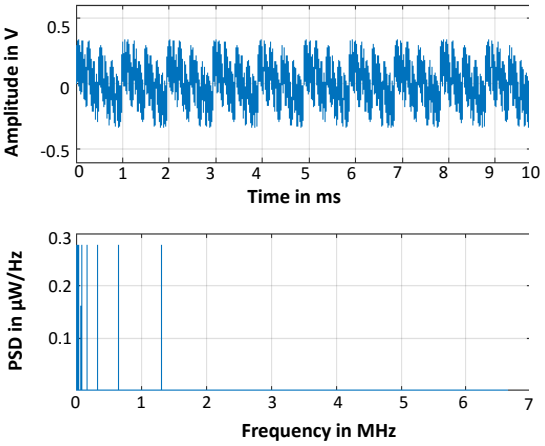

(c) Decimal distributions of frequencies

FIGURE 6.12: Multisine signal and its power spectral density

Figure 6.12 depicts the shape of the multisine signal and its PSD with different distributions of frequencies (equally spaced, binary and decimal).

The amplitude of PSD with equally spaced frequency components shows equal distributions of 8 components of multisine, nearly to 0.284 μW/Hz that it can be written as M x (0.8 xA_k)^2/2Rf_1 (Figure 6.12(a)). The same levels of PSD of binary rated frequency components of multisine (0.284 μW/Hz) (Figure 6.12(b)) and the same average power equals to 2.25 10^{-5}W are obtained.

The average power of decimal distributions of frequencies is 0.04 Watts which is approximately equal to 4x(0.4 xA_k)^2/2R: Only three frequency components (f_i=1000; 10000; 100000; 1000000) contain equal level of PSD (Figure 6.12(c)).

Table 6.3 summarizes various parameters that describe the energy spread of various multisine signals that differ from the type of frequency distributions.

TABLE 6.3: Comparison of multisine signals in terms of energy metrics and time

Frequency distribution	CF	Average power (μW)	Energy E (μJ)	Energy efficiency (%)	Time (ms)
Equally spaced	3.07	22.5	2.27	100	101
Binary	2.24	22.5	2.22	99.99	98.6
Decimal	2.79	45.0	4.54	99.93	101

Acceptable results could be obtained in case of less sparse frequency distributions as equally spaced one but it represents the drawback of no coverage the whole frequency bandwidth.

It is desirable to use reduced components number of sine waves to inject higher power into the system. We can conclude that generating a multisine with reduced number of sinusoidal components with decimal distributions of frequency components is the most appropriate as it allows high power in a wide frequency range .

Figure 6.13(a) shows that only a finite set of frequency are excited: there is no loss of energy between higher harmonics. A leakage effect is greatly appeared

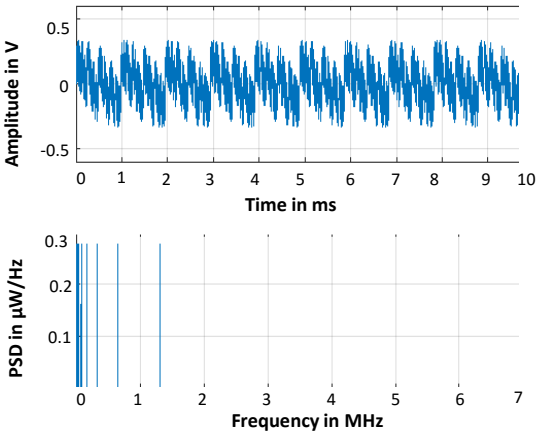

(a) without noise

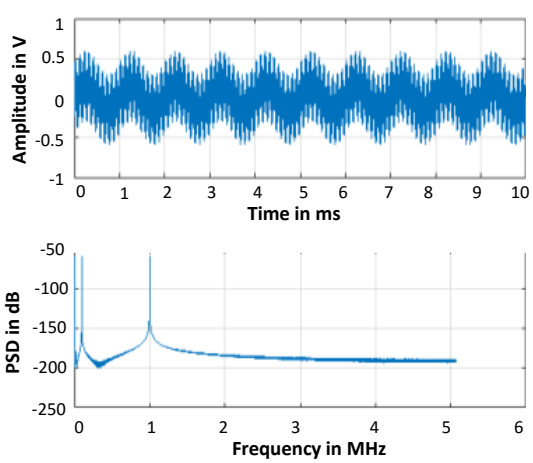

(b) $SNR = 100dB$

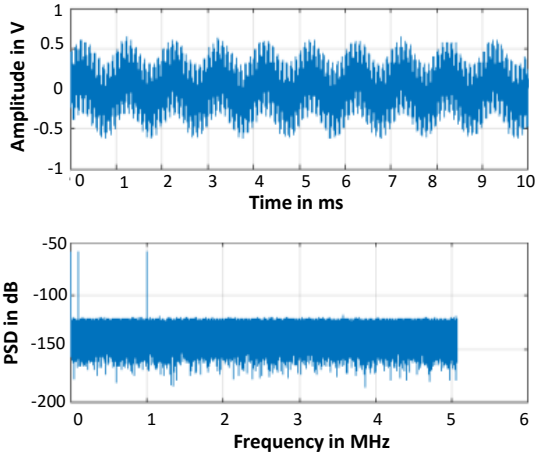

(c) $SNR = 20dB$

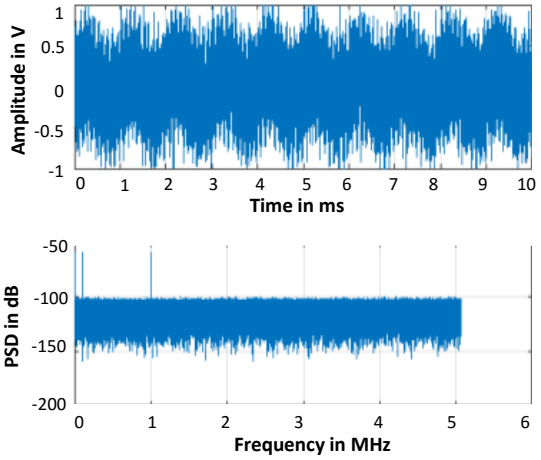

(d) $SNR = 0dB$

FIGURE 6.13: Multisine signal and its power spectral density

when increasing the applied noise level which deteriorates the measurement results (Figure 6.13(c), 6.13(d)).

6.2.6 Binary multifrequency

The binary multifrequency signal has a reduced time factor as the measurement process is running in parallel at several frequencies. Furthermore, it can be easier generated and results in a higher excitation power compared to multisine waveform [108].
The mathematical model of multifrequency binary signal is given by the expression below:

$$x(t) = sign(\sum_{k=1}^{N} A_k \sin(2\pi\, f_k t + \phi_k)) \tag{6.45}$$

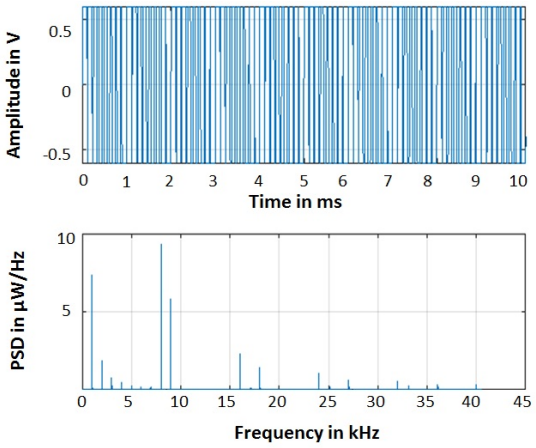

(a) Equally spaced distribution

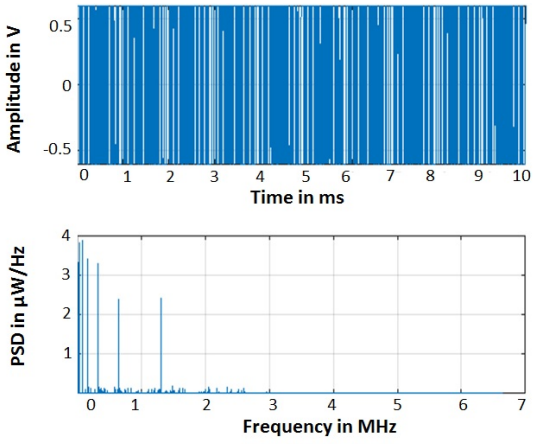

(b) Binary distribution

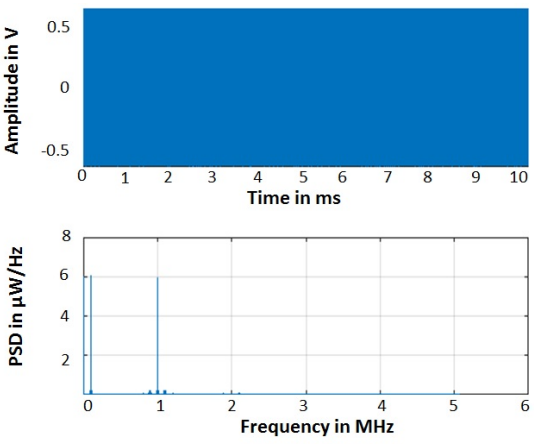

(c) Decimal distribution of frequencies

FIGURE 6.14: Binary-multifrequency signals with 4 sine wave components and its power spectral density

We proceed with the same steps mentioned on the previous section, only we define the mathematical model as the signum function of the multisine signal. The shape of binary-multifrequency signal consisting of four sine wave components and its PSD with different distributions of frequencies is shown in Figure 6.14.

Binary-multifrequency signal provides higher excitation power (around 0.36 mW) compared to the multisine with 4 components of sine waves. However, part of the power is wasted between higher harmonics. The level of PSD is variable and does not exceed 10μW/Hz in both equally spaced (Figure 6.14(a)) and binary distributions of frequencies (Figure 6.14(b)). On the other side, the PSD level is almost constant and presents less power losses in case of binary-multifrequency with decimal frequencies distributions (Figure 6.14(c)). As well as we noticed in

the case of multisine, it is more beneficial to use a low number of components since less wasted power are figured in higher harmonics (Figure 6.14(c)).

Table 6.4 summarizes the CF, energy, average power and energy efficiency of several binary-multifrequency signals in different frequencies distributions. Almost the same amount of the average power is delivered. The lowest energy efficiency is illustrated in case of equally spaced distribution of frequency.

TABLE 6.4: Comparison of Binary-multifrequency signals in terms of energy metrics and time

Frequency distribution	CF	Average power (mW)	Energy (μJ)	Energy efficiency (%)	Time (ms)
Equally spaced	1.00	0.359	36.65	57.34	101
Binary	1.00	0.360	36.35	82.67	98.6
Decimal	1.00	0.360	36.36	77.98	101

Figure 6.15 depicts that nearly the same power spectrum shape is provided for the three SNR values. It turned out that binary-multifrequency signal with decimal frequency distribution is preferable, although the spread of energy between the undesired frequency range. When decreasing the noise's level (Figure 6.15(b), 6.15(c) and 6.15(d)), the binary-multifrequency provides low error in a very noisy environment.

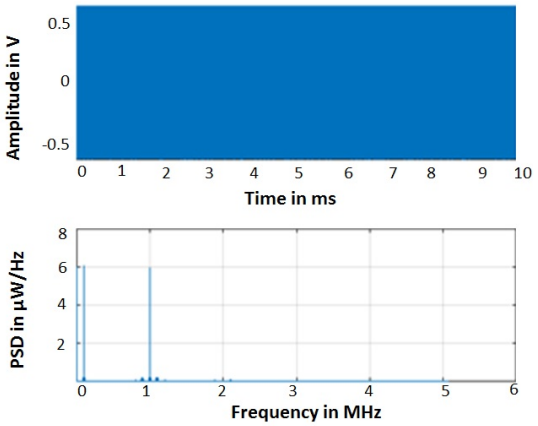

(a) without noise

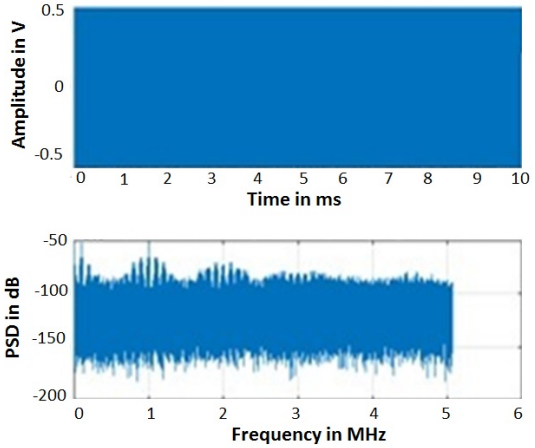

(b) $SNR = 100dB$

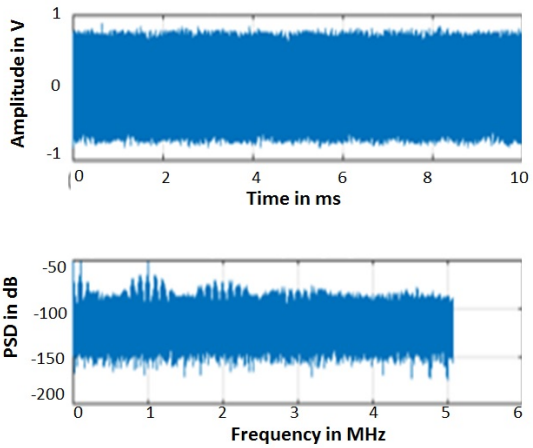

(c) $SNR = 20dB$

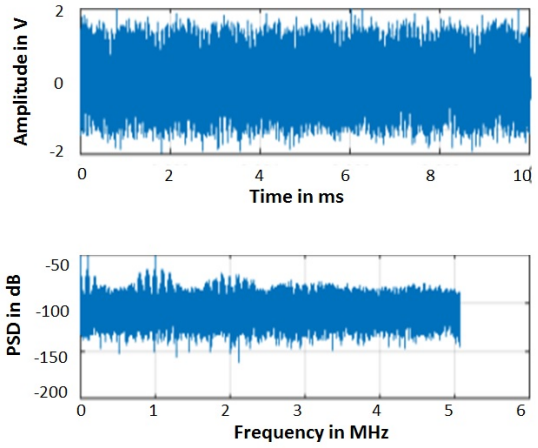

(d) $SNR = 0dB$

FIGURE 6.15: Binary multifrequency with decimal distribution and its power spectral density

6.2.7 Maximum length sequence (MLS)

The maximum length sequence (MLS) is generated using a shift register with n stages. The MLS is a periodic signal with the period of T_{MLS}=(2^n-1)T_s where T_s is the clock duration. The optimal value of the sampling frequency is F_s=0.44/f where f = 1 MHz is the maximum frequency of interest [40]. It is recommended to use high number of samples N=2^n-1 as the SNR is increased by a function of N leading to high measurement time. In this study, N is set at 1023. Hence, n is equal to 10 bits.

The MLS signal with amplitude "A" has an average power across 1 kΩ load: $P_{avg} = \frac{A^2}{R} = 0.36$ mW and a power spectral density (PSD) P = $\frac{A^2}{R}\ \frac{(N+1)}{N^2}\ \frac{sin(k\pi\, N)^2}{(k\pi\, N)^2}$

Figure 6.16(a) shows that the power spectrum follows the envelope of $\frac{sin(F)^2}{F^2}$. It reaches the maximum value at the first component given by $A^2\ \frac{(N+1)}{N^2R}$ and reduces to zero at f_k = kF_s for k = 1, 2, 3,. . . , n. Therefore, MLS spectrum presents a not flat spectrum. In addition, MLS signal has low energy efficiency which corresponds to only 67.23%. But we cannot neglect the fact that MLS has few advantages as any Binary signals such as simplicity of generation and unity crest factor.

The MLS signal has the shape of $sin(f)/f$ function. So that an important part of energy is distributed out of the frequency band of interest for the both cases (Figure 6.16(b), Figure 6.16(c)). The difference is that the second one is more disturbed by noise as higher level of error is introduced to the input signal. This characteristic of MLS power spectrum is tampered off in case of the lowest SNR (Figure 6.16(d)).

From these simulations, it can be concluded that deterministic signals are preferred to the noisy signals because they results in smaller measurement errors

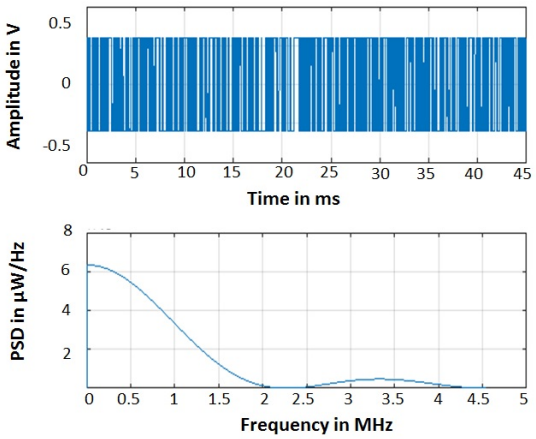

(a) Without noise

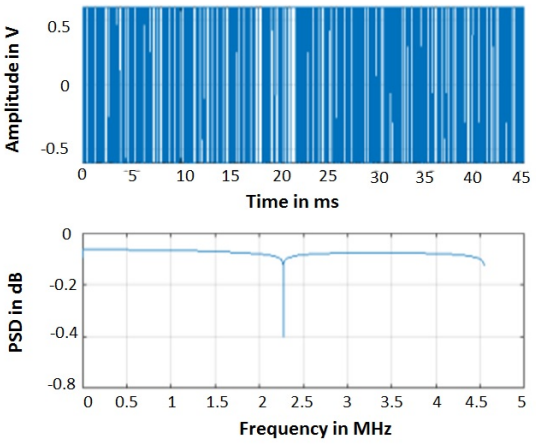

(b) $SNR = 100dB$

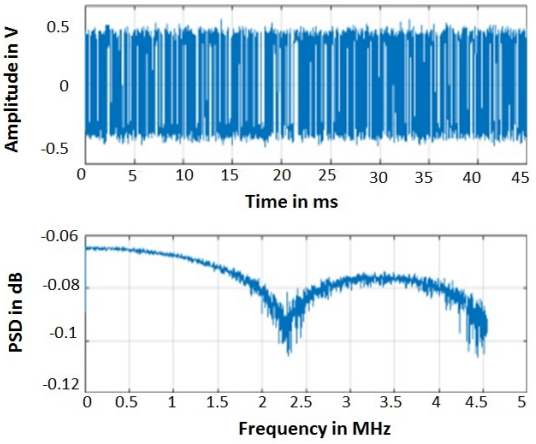

(c) $SNR = 20dB$

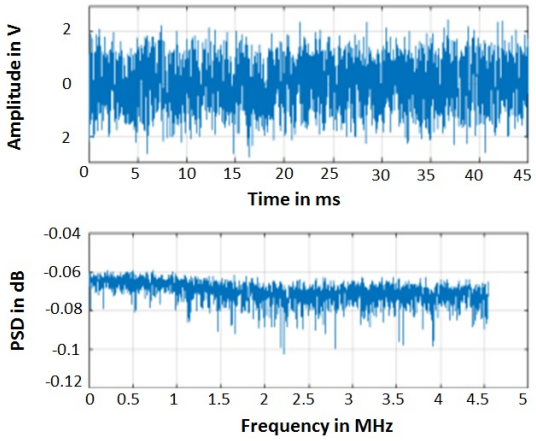

(d) $SNR = 0dB$

FIGURE 6.16: MLS signal generated by 10 bits shift register and its power spectrum

.

6.3 Comparative study of different excitation signals

A comparative study between different kinds of excitation signals in terms of various properties such as CF values, average power, total energy, energy efficiency, power spectrum shape, acquisition time and hardware complexity are summarized in Table 6.5.

TABLE 6.5: Comparison of selected excitation signals in term of energy metrics and time

Signal Type	SNR (dB)	Crest Factor	Average Power (mW)	Total Energy (μJ)	Energy Efficiency (%)	Power Spectrum Shape	Acquisition Time (ms)
Sine	100	1.41	0.18	0.02	100	Discrete	0.101 (one measurement time)
	20	1.62	0.18	0.02	99.2		
	0	2.91	0.36	0.04	56.26		
Binary Sine	100	1.00	0.36	0.04	82.07	Discrete	0.101 (one measurement time)
	20	1.19	0.36	0.04	81.78		
	0	2.79	0.73	0.07	43.79		
Multisine	100	2.79	0.01	4.54	99.93	Discrete	101
	20	3.06	0.04	4.59	99.14		
	0	4.68	0.09	9.07	59.80		
Binary Multi-frequency	100	1.00	0.36	36.35	82.67	Discrete	98.6
	20	1.40	0.36	35.85	82.13		
	0	4.25	0.72	71.19	51.09		
Linear Chirp	100	1.43	0.18	0.02	98.85	Continuous Fluctuating	0.101
	20	1.68	0.18	0.02	98.12		
	0	2.53	0.36	0.04	62.48		
Sigrum Chirp	100	1.00	0.36	0.04	85.20	Continuous Fluctuating	0.101
	20	1.27	0.37	0.04	84.75		
	0	2.75	0.73	0.07	54.67		
MLS	100	1.00	0.36	0.16	67.23	Continuous Fluctuating	0.45
	20	1.33	0.36	0.16	66.57		
	0	2.91	0.70	0.32	33.5		

Comparing the crest factor of studied excitation signals (Figure 6.17), the highest ones are given by the multisine (CF=4.68) and the binary multifrequency (CF=4.25), in the worst case of noise ($SNR = 0dB$).

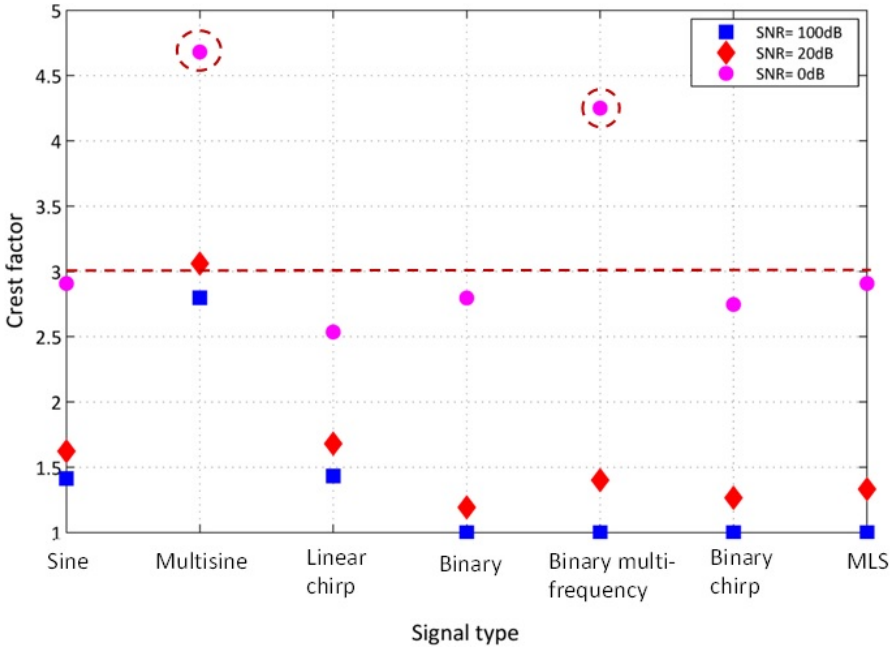

FIGURE 6.17: Crest factor variation for selected excitation signals

Figure 6.18 depicts the variation of the energy efficiency of selected excitation signals, when applying different levels of noise. When varying the SNR from 100 dB to 20 dB, the excitation signals have the same results. However, in the worst case of noise which corresponds to 0 dB, the energy efficiency deceases dramatically to approximately the half for all selected excitation signals. In particular, MLBS signal and Binary signal have the lowest energy efficiency $\delta_E = 33.5\%$ and $\delta_E = 43.5\%$, respectively.

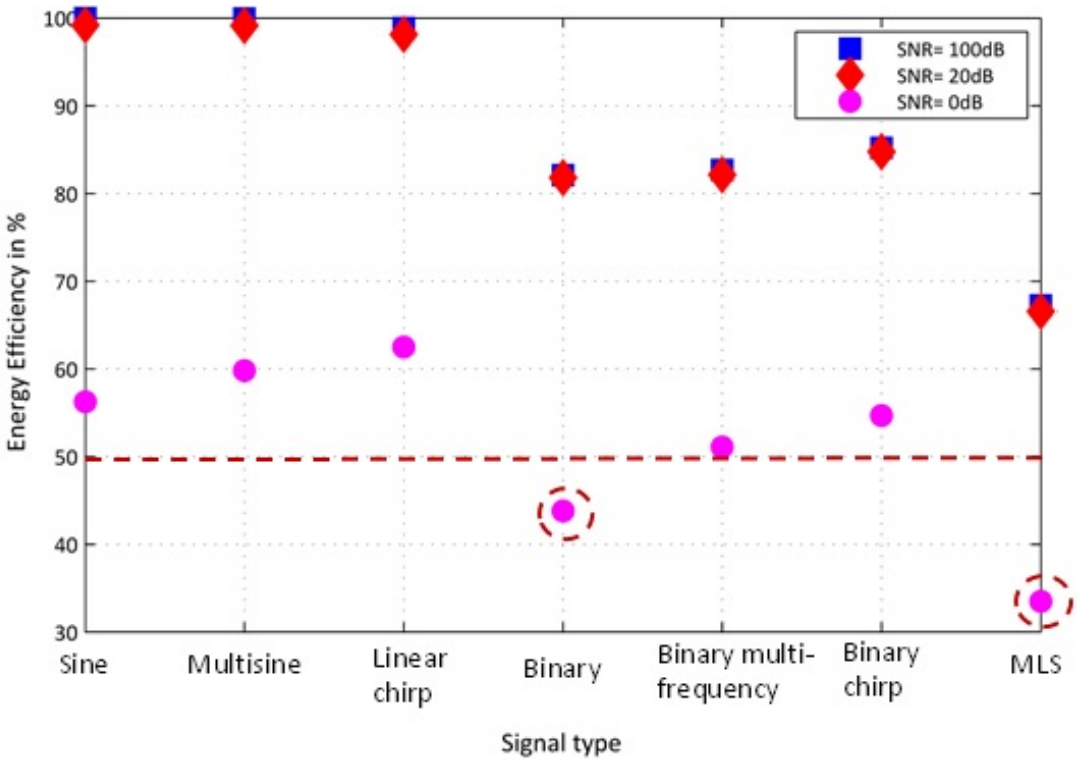

FIGURE 6.18: Energy efficiency variation for selected excitation signals

The comparative study of the influence of the noise on the energy efficiency and the crest factor has proven that the sine wave, the linear chirp and the binary chirp have the higher energy efficiency and the low crest factor. However, the sine wave requires long measurement time which is not preferable for real time systems (Table 6.5).

The requirements for a portable bioimpedance spectrometer are the high energy efficiency, low crest factor and short measurement time. The crest factor is better achieved in case of the signum chirp signal compared to the linear chirp (Table 6.5). As a conclusion, the most suitable excitation signals that fulfill the requirements of portable bio-impedance spectrometer is the binary chirp.

To validate the performance of the enhanced Howland current source selected in the chapter 3 connected to the studied excitation signals; we compute the flatness and the error which are defined in the third chapter. After varying the load from 100 Ω to 10 kΩ, in increment of 1 kΩ, errors of the enhanced Howland current source connected to various excitation signals are simulated (Figure 6.19).

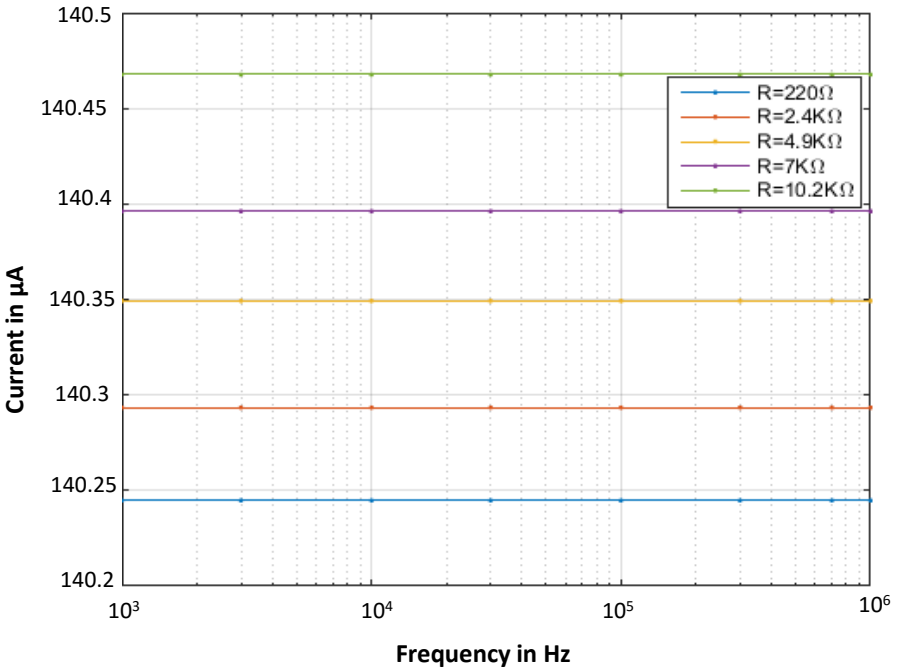

FIGURE 6.19: Output current variation for binary chirp

On the other side, flatness are given when we fix the load at 4004 Ω through a wide range of frequency between 1 kHz and 1 MHz. Simulation results show that errors at 1 kHz and at 1 MHz are respectively 0.023% and 0.018%. While the flatness is lower than 0.001%. Same low errors are provided in each excitation signal for both low and high frequencies. These results are nearly the same as experimental results obtained for the sine signal. The errors at 1 kHz and at 1MHz are respectively 0.021% and 0.017%, while the flatness is 0.043%.

As a conclusion, simulations of the VCCS connected to different excitation signals has been made and the computation of flatness and errors were carried out. From these simulations, we conclude that binary chirp input is the most pertinent signal as it provides also the lowest flatness of the Enhanced Howland current source circuit.

7. Conclusion

Bioimpedance spectroscopy is very useful as a safe and non-invasive technique. β -dispersion frequency range, from kHz up to 1MHz, is very important because it allows getting comprehensive information about the state of a biological tissue. This is why it is important to realize measurements in this full range with a high accuracy.

The accuracy of the excitation current can greatly affect the quality of the measurement results and the amplitude level should fulfill the safety requirements. Getting a stable and safe injected current below than 0.5 mA for load impedances changing from 100 Ω to 10 kΩ remains a challenge for the design of the current source. Stable and accurate excitation current requires a high output impedance, which is not fulfilled by a lot of current sources structures.

A big focus of this thesis is the design of a high accurate excitation current source with high output impedance fulfilling both technical for bioimpedance measurements and medical requirements for patient safety.

Different current source types in current-mode and voltage-mode approaches are compared for usability in bioimpedance measurement systems. As current-mode sources require custom fabrication and market available sources don't fulfill the requirements, the interest in this thesis remains on the voltage-mode approach.

The voltage-mode current source can be classified in two main types depending on the load connection: floating load and grounded load. Due to the instability and the accuracy losses of the floating load type, we conclude that the grounded load type is more suitable for biomedical measurements.

The most important structures for grounded load type are the Howland and the Tietze topologies. These circuits are evaluated by simulations after the choice of suitable configuration and components. The Tietze and dual configuration with negative feedback have the lowest error of the output current and the highest output impedance. The improved Howland circuit in dual configuration with a negative feedback has thereby a higher efficiency with its simple structure, higher accuracy and better stability than other configurations. Based on experimental investigations, we suggest an improved circuit in inverting dual configuration with

a negative feedback using compensated operational amplifiers. This allows realizing a current injection in the range lower than 0.5 mA even at higher frequencies up to 1 MHz with large load up to 10 kΩ. This is not easy to realize with other structures.

Nevertheless, the performance of the Howland circuit is strongly related to the performance of the chosen operational amplifiers. The resistors are required to be closely matched and the operational amplifier is chosen with a high common mode rejection ratio, high open loop gain, low input bias current and low input noise voltage density. At high frequencies, the main limitation is the presence of the stray capacitances. To cancel their effects, many solutions could be applied such as the generalized impedance converter, the negative impedance converter and the external compensation. The addition of gain compensation capacitor shows a good performance at high frequencies until 1 MHz.

The choice of suitable operational amplifiers is important for the performance of the current source in voltage mode. After a pre-selection of interesting operational amplifiers, a deep investigation was carried out. It included simulations and experimental investigations to show especially the behavior at the limits of the frequency and measurement range. At low frequencies, the compensated operational amplifier AD8021 has slightly larger error than uncompensated operational amplifier AD8041. For high frequencies up to 1 MHz, AD8021 has smaller error around 0.02% than 0.2% for AD8041. In addition, the flatness for the compensated amplifier (0.05%) is smaller than the uncompensated amplifier (0.2%). Thereby, the compensated operational amplifier AD8021 has the best performance, not only the errors at 1 MHz, but also the worst flatness.

With the realized accuracy of the designed voltage controlled current source, one decisive pre requisite for portable bioimpedance measurement system is achieved. The characterization and real time monitoring of biological materials and patient health state require also short measurement time and low power consumption. These requirements are directly related to the type of excitation signal for portable multi-frequency impedance device in the medical field.

In order to select the appropriate excitation signal for the bioimpedance system, a comparative study of the signal's parameters was carried out. In this study, we investigated different excitation signal types in order to select the suitable time saving excitation signals for a portable impedance measurement system. Only

periodic excitations were chosen, so that leakage problems can be avoided in frequency domain analysis and higher SNR can be obtained.

A comparison of different signals was carried out, while respecting the constraints on the system including time, energy efficiency, cost and ease of generation and at the same time guarantying the safety of the patient by limiting the current's magnitude. Thereby, it is important also to consider the influence of noise, because it is unavoidable in an electronic system.

To consider the trade-off between the reconstructed signal's quality, the time consumption and the hardware complexity, the signal's parameters (the number of samples and the sampling rate) are optimized when applying different levels of noise. Based on optimized parameters, a comparative study of the energy efficiency and measurement time of different excitation signals leads to the selection of binary chirp signal. It is a suitable excitation signal due to its short measurement time about 100 μs, low crest factor lower than 2.8 and higher energy efficiency higher.

To validate the performance of the designed voltage controlled current source with the studied excitation signals, the error and the flatness are simulated. Simulation results show that the designed enhanced Howland current source excited by the binary multifrequency signal has low error and flatness in the whole frequency range.

A. Apendix: Sine fitting algorithm

Considering the sinusoidal model defined by M data points

$$y_i = A\sin(2\pi\, ft_i + \phi) \tag{A.1}$$

Where ϕ is the initial phase and f is the frequency. We consider the phase ϕ to be a random variable uniformly distributed in an interval with length 2π.
This signal is affected by an additive Gaussian white noise assumed to be zero-mean with variance σ^2. Additionally, it is supposed that the noise is not correlated with the sine signal.

$$y_i = A\sin(2\pi\, ft_i + \phi) + e_i \tag{A.2}$$

The estimation of the noisy signal parameters is obtained by the following expression:

$$X = (D^T D)^{-1} D^T Y \tag{A.3}$$

Where: $X = [a\, b]^T$ is the estimated parameters vector, $Y = [y_1\, y_2 \ldots y_n]^T$ is the sample vector and D is a matrix given by:

$$D = \begin{pmatrix} \cos(\omega t_1) & \sin(\omega t_1) \\ \vdots & \vdots \\ \cos(\omega t_n) & \sin(\omega t_n) \end{pmatrix} \tag{A.4}$$

Consequently, the fitted amplitude and the relative amplitude error can be determined as:

$$A_{fit} = \sqrt{a^2 + b^2} \tag{A.5}$$

$$\epsilon_A = \frac{\|A - A_{fit}\|}{A} \tag{A.6}$$

The inverse matrix D^T D is given by:

$$D^T D = \begin{pmatrix} \sum_{i=0}^{n-1} \cos(\omega t_i)^2 & \sum_{i=0}^{n-1} \cos(\omega t_i) \sin(\omega t_i) \\ \vdots & \vdots \\ \sum_{i=0}^{n-1} \cos(\omega t_i) \sin(\omega t_i) & \sum_{i=0}^{n-1} \sin(\omega t_i)^2 \end{pmatrix} \tag{A.7}$$

Since the samples cover an integer number of signal periods the off-diagonal elements are zero leading to the following equation:

$$D^T D = \begin{pmatrix} \sum_{i=0}^{n-1} \cos(\omega t_i)^2 & 0 \\ 0 & \sum_{i=0}^{n-1} \sin(\omega t_i)^2 \end{pmatrix} \tag{A.8}$$

If the two summations in (A8) are null the matrix will be singular and thus non-invertible. To prevent this, the phase should satisfy the following expression:

$$wt_i \neq, k\pi \; with \; k = 1, 2 \ldots \tag{A.9}$$

For at least one sample with w= 2πf and using (14), we obtain:

$$\frac{F_s}{f} \neq \frac{2}{k} \tag{A.10}$$

This relation is always true since we respect Shannon theorem.

B. Apendix: Chirp fitting algorithm

We define the following noisy chirp signal model by

$$y_i = A\sin(2\pi(f_0 t_i + \frac{(f_{fin} - f_0)}{T_{ch}}\frac{t_i^2}{2}) + \phi) + e_i \tag{B.1}$$

where A is the amplitude, $K_{ch} = \frac{(f_fin - f_0)}{T_{ch}}$ is the rate chirp, f_0, f_{fin} and T_{ch} are respectively the initial frequency, the final frequency and the chirp duration, ϕ is the phase and the error e_i is a sequence of random variables with null mean and standard deviation σ. The noisy chirp can be also written as

$$u(t) = a\cos(\alpha_0 t_n + \beta_0 t_n^2) + b\sin(\alpha_0 t_n + \beta_0 t_n^2)) \tag{B.2}$$

where:

$$\alpha_0 = 2\pi\, f_0 \tag{B.3}$$

$$\beta_0 = \pi\,\frac{f_{fin} - f_0}{T_{ch}} \tag{B.4}$$

a and b can be obtained by solving the following expression:

$$X = (D^T D)^{-1} D^T Y \tag{B.5}$$

Where:
$Y = [y_1\, y_2 \ldots y_n]^T$ is the sample vector and the matrix D is defined as follow:

$$D = \begin{pmatrix} \cos(\alpha_0 t_1 + \beta_0 t_1^2) & \sin(\alpha_0 t_1 + \beta_0 t_1^2) \\ \vdots & \vdots \\ \cos(\alpha_0 t_n + \beta_0 t_n^2) & \sin(\alpha_0 t_n + \beta_0 t_n^2) \end{pmatrix} \tag{B.6}$$

As well as the previous work, the estimated amplitude and the relative amplitude error are given by:

$$A_{fit} = \sqrt{a^2 + b^2} \tag{B.7}$$

$$\epsilon_A = \frac{\|A - A_{fit}\|}{A} \tag{B.8}$$

C. Apendix: Multisine fitting algorithm

The M data points of the multisine signal is given by

$$y_i = \sum_{k=1}^{N} A_k \sin(2\pi\, f_k t + \phi_k) \tag{C.1}$$

Where N, A_i, f_i and ϕ_i denote respectively the number of multisine components, the fundamental amplitudes, the frequencies and phases Equation (A19) can be rewritten as a sum of sine and cosine as below:

$$y_i = \sum_{k=1}^{N} a_k \cos(2\pi\, f_k t_i) + \phi_k + b_k \sin(2\pi\, f_k t_i) \tag{C.2}$$

Thus, a_k and b_k are obtained by solving the following equation

$$X = (D^T D)^{-1} D^T Y \tag{C.3}$$

Where:

$$D = \begin{pmatrix} \cos(2\pi f_1 t_1) & \sin(2\pi f_1 t_1) & ... & \cos(2\pi f_N t_1) & \sin(2\pi f_N t_1) \\ \cos(2\pi f_1 t_2) & \sin(2\pi f_1 t_2) & ... & \cos(2\pi f_N t_2) & \sin(2\pi f_N t_2) \\ \vdots & \vdots & \vdots & \vdots & \\ \cos(2\pi f_1 t_n) & \sin(2\pi f_1 t_n) & ... & \cos(2\pi f_N t_n) & \sin(2\pi f_N t_n) \end{pmatrix} \tag{C.4}$$

The estimated amplitudes and the corresponding relative amplitude errors are defined as:

$$A_{kfit} = \sqrt{a_k^2 + b_k^2} \tag{C.5}$$

$$\epsilon_{A_k} = \frac{\|A_k - A_{kfit}\|}{A_k} \tag{C.6}$$

After presenting the main terms related to the thesis and the theoretical computations needed in the following sections. The next chapter reviews the features of different excitation signals established in bio-impedance measurement systems.

Bibliography

[1] H-R. Tränkler, O. Kanoun, M. Min, and M. Rist. Smart sensor systems using impedance spectroscopy. *Proc. Estonian Acad. Sci. Eng*, 13(4):455–478, 2007.

[2] M. Min. *Cardiac pacemakers-biological aspects, clinical applications and possible complications*. InTech, 2011.

[3] P. Hansma, H. Yu, D. Schultz, A. Rodriguez, E.A. Yurtsev, J. Orr, S. Tang, J. Miller, J. Wallace, F. Zok, et al. The tissue diagnostic instrument. *Review of Scientific Instruments*, 80(5):054303, 2009.

[4] D. Spelmezan, A. Schanowski, and J. Borchers. Rapid prototyping for wearable computing, media computing group. In *International Symposium on Werable Computing*, 2008.

[5] S. Kun, B. Ristić, R.A. Peura, and R.M Dunn. Algorithm for tissue ischemia estimation based on electrical impedance spectroscopy. *IEEE Transactions on Biomedical Engineering*, 50(12):1352–1359, 2003.

[6] M. Mayer, P. Brunner, R. Merwa, and H. Scharfetter. Monitoring of lung edema using focused impedance spectroscopy: a feasibility study. *Physiological measurement*, 26(3):185, 2005.

[7] P. Aberg, I. Nicander, J. Hansson, P. Geladi, U. Holmgren, and S. Ollmar. Skin cancer identification using multifrequency electrical impedance-a potential screening tool. *IEEE Transactions on Biomedical Engineering*, 51(12):2097–2102, 2004.

[8] C. Skourou, P.J. Hoopes, R.R. Strawbridge, and K.D. Paulsen. Feasibility studies of electrical impedance spectroscopy for early tumor detection in rats. *Physiological measurement*, 25(1):335, 2004.

[9] A. Ivorra. Bioimpedance monitoring for physicians: an overview. *Centrale Nationale de Microélectronique*, 2003.

[10] T. Sodolski and A. Kutarski. Impedance cardiography: A valuable method of evaluating haemodynamic parameters. *Cardiology Journal*, 14(2):115, 2007.

[11] O.G. Martinsen and S. Grimnes. *Bioimpedance and bioelectricity basics*. Academic press, 2011.

[12] A.O. Ragheb, L.A. Geddes, J.D. Bourland, and W.A. Tacker. Tetrapolar electrode system for measuring physiological events by impedance. *Medical and Biological Engineering and Computing*, 30(1):115–117, 1992.

[13] L.A. Geddes. Who introduced the tetrapolar method for measuring resistance and impedance? *IEEE Engineering in Medicine and Biology Magazine*, 15(5):133–134, 1996.

[14] S.B. Brown. Biological spectroscopy. *Biochemical Education*, 13(2):93–93, 1984.

[15] R. Pallas-Areny and J.G. Webster. Bioelectric impedance measurements using synchronous sampling. *IEEE transactions on Bio-medical Engineering*, 40(8):824–829, 1993.

[16] P. Steendijk, G. Mur, E.T. Van Der Velde, and J. Baan. The four electrode resistivity technique in anisotropic media: theoretical analysis and application on myocardial tissue in vivo. *IEEE Transactions on Biomedical Engineering*, 40(11):1138–1148, 1993.

[17] R. Casanella, O. Casas, et al. Differential synchronous demodulator for modulating sensors and impedance measurements. *Measurement Science and Technology*, 16(8):1637, 2005.

[18] Y. Yang, J. Wang, G. Yu, F. Niu, and P. He. Design and preliminary evaluation of a portable device for the measurement of bioimpedance spectroscopy. *Physiological Measurement*, 27(12):1293, 2006.

[19] D. Bouchaala, X. Chen, Q. Shi, O. Kanoun, and N. Derbel. Comparative study of voltage controlled current sources for biompedance measurements. In *9th International Multi-Conference on Systems, Signals and Devices*, pages 1–6, 2012.

[20] S. Grimnes and O.G. Martinsen. Bioimpedance and bioelectricity basics. *New York*, 2000.

[21] L.E. Baker. Applications of the impedance technique to the respiratory system. *IEEE Engineering in Medicine and Biology Magazine: the Quarterly Magazine of the Engineering in Medicine & Biology Society*, 8(1):50–52, 1988.

[22] K.S. Cole and R.H. Cole. Dispersion and absorption in dielectrics: Alternating current characteristics. *The Journal of Chemical Physics*, 9(4):341–351, 1941.

[23] M. Min, T. Parve, A. Ronk, P. Annus, and T. Paavle. Synchronous sampling and demodulation in an instrument for multifrequency bioimpedance measurement. *IEEE Transactions on Instrumentation and Measurement*, 56(4):1365–1372, 2007.

[24] T. Schlebusch, L. Röthlingshöfer, S. Kim, M. Köny, and S. Leonhardt. On the road to a textile integrated bioimpedance early warning system for lung edema. In *International Conference on Body Sensor Networks*, pages 302–307, 2010.

[25] L. Beckmann, A. Cordes, E. Saygili, A. Schmeink, P. Schauerte, M. Walter, and S. Leonhardt. Monitoring of body fluid in patients with chronic heart failure using bioimpedance-spectroscopy. In *World Congress on Medical Physics and Biomedical Engineering*, pages 532–535. Springer, 2009.

[26] A. Fein, R.F. Grossman, J.G. Jones, P.C. Goodman, and J.F. Murray. Evaluation of transthoracic electrical impedance in the diagnosis of pulmonary edema. *Circulation*, 60(5):1156–1160, 1979.

[27] I. Marinova and V. Mateev. Determination of electromagnetic properties of human tissue. *World Acad Sci Eng Tech*, 42(4):591–595, 2010.

[28] H.P. Schwan. Electrical properties of tissues and cell suspensions: mechanisms and models. In *Engineering in Medicine and Biology Society*, pages A70–A71, 1994.

[29] J.J. Ackmann and M.A. Seitz. Methods of complex impedance measurements in biologic tissue. *Critical Reviews in Biomedical Engineering*, 11(4):281–311, 1983.

[30] R.E. Dodde. *Bioimpedance of soft tissue under compression and applications to electrosurgery.* PhD thesis, The University of Michigan, 2011.

[31] J. Rosell, J. Colominas, P. Riu, R. Pallas-Areny, and J.G. Webster. Skin impedance from 1 hz to 1 mhz. *IEEE Transactions on Biomedical Engineering*, 35(8):649–651, 1988.

[32] B. Rigaud, L. Hamzaoui, M.R. Frikha, N. Chauveau, and J.P. Morucci. In vitro tissue characterization and modelling using electrical impedance measurements in the 100 hz-10 mhz frequency range. *Physiological measurement*, 16(3A):A15, 1995.

[33] J.P. Morucci and B. Rigaud. Bioelectrical impedance techniques in medicine. part iii: Impedance imaging. third section: medical applications. *Critical Reviews in Biomedical Engineering*, 24(4-6):655–677, 1995.

[34] B.H. Brown, J.A. Tidy, K. Boston, A.D. Blackett, R.H. Smallwood, and F. Sharp. Relation between tissue structure and imposed electrical current flow in cervical neoplasia. *The Lancet*, 355(9207):892–895, 2000.

[35] N. Tleis. *Power systems modelling and fault analysis: theory and practice*. 2007.

[36] P. Bertemes-Filho, V. Coelho Vincence, M.S. Santos, and I.X. Zanatta. Low power current sources for bioimpedance measurements: A comparison between howland and integrated cmos ota circuits. *Journal of Electrical Bioimpedance*, 3(1):66–73, 2012.

[37] J. Schoukens, R. Pintelon, Edwin Van Der Ouderaa, and J. Renneboog. Survey of excitation signals for fft based signal analyzers. *IEEE Transactions on Instrumentation Measurement*, 37:342–352, 1988.

[38] R. Pintelon and J. Schoukens. *System identification: a frequency domain approach*. John Wiley & Sons, 2012.

[39] Fourier series and gibbs phenomenon overview. http://www.seas.ucla.edu/dsplab/fgp/over.html, Accessed 12 02 2016.

[40] J. Ojarand, M. Min, and P. Annus. Crest factor optimization of the multisine waveform for bioimpedance spectroscopy. *Physiological measurement*, 35(6):1019, 2014.

[41] Gaussian waves. http://www.gaussianwaves.com/2011/01/fft-and-spectral-leakage-2/, Accessed 09 02 2016.

[42] U. Lee. *Spectral element method in structural dynamics*. John Wiley & Sons, 2009.

[43] J. Ojarand and M. Min. Efficient excitation signals for the fast impedance spectroscopy. *Elektronika ir Elektrotechnika*, 20(5):144–149, 2014.

[44] R. Bragos, R. Blanco-Enrich, O. Casas, and J. Rosell. Characterisation of dynamic biologic systems using multisine based impedance spectroscopy. In *Proceedings of the 18th IEEE Instrumentation and Measurement Technology Conference*, volume 1, pages 44–47, 2001.

[45] T. Paavle, M. Min, and T. Parve. *Aspects of using chirp excitation for estimation of bioimpedance spectrum*. INTECH Open Access, 2012.

[46] T. Paavle. Short-time chirp excitation for wideband identification of dynamic objects. *Estonian Journal of Engineering*, 17(2):169–179, 2011.

[47] P. Stoica and R.L. Moses. *Spectral analysis of signals*. Pearson/Prentice Hall Upper Saddle River, NJ, 2005.

[48] C. Schenk, U. Tietze, and E. Gamm. Electronic circuits: Handbook for design and application, 2008.

[49] D. Bouchaala, O. Kanoun, and N. Derbel. High accurate and wideband current excitation for bioimpedance health monitoring systems. *Measurement*, 79:339–348, 2016.

[50] F. Seoane Martinez. Electrical bioimpedance cerebral monitoring: Fundamental steps towards clinical application. *Department of Signals and Systems. Göteborg, Chalmers University of Technology. PhD*, page 137, 2007.

[51] C. Toumazou and F.J. Lidgey. Novel current-mode instrumentation amplifier. *Electronics Letters*, 25(3):228–230, 1989.

[52] W.K. Chen. *Feedback, nonlinear, and distributed circuits*. CRC Press, 2009.

[53] H. Hong, M. Rahal, A. Demosthenous, and R.H. Bayford. Floating voltage-controlled current sources for electrical impedance tomography. In *18th European Conference on Circuit Theory and Design*, pages 208–211, 2007.

[54] H. Hong, A. Demosthenous, I.F. Triantis, P. Langlois, and R. Bayford. A high output impedance cmos current driver for bioimpedance measurements.

In *IEEE Biomedical Circuits and Systems Conference (BioCAS)*, pages 230–233, 2010.

[55] E.A. Vittoz and X. Arreguit. Cmos integration of herault-jutten cells for separation of sources. In *Analog VLSI implementation of neural systems*, pages 57–83. Springer, 1989.

[56] J.G. Graeme. *Applications of operational amplifiers*. McGraw-hill, 1973.

[57] J.G. Graeme, G.E. Tobey, and L.P. Huelsman. *Operational amplifiers: Design and applications*, volume 1. McGraw-Hill, Burr-Brown Research Corporation, 1971.

[58] B. Wilson. A low-distortion bipolar feedback current amplifier technique. *Proceedings of the IEEE*, 69(11):1514–1515, 1981.

[59] C.W. Denyer, F.J. Lidgey, Q.S. Zhu, and C.N. McLeod. A high output impedance current source. *Physiological measurement*, 15(2A):A79, 1994.

[60] H.T.L. Leung, R.J. Williams, H. Griffiths, and T.J. Hames. A wide-band current source for electrical impedance tomography. In *Proc. of a Meeting on Electrical Impedance Tomography*, 1990.

[61] P. Record, R. Gadd, and P. Rolfe. A signal conditioning electrode for use in electrical impedance tomography. In *Proc. of a Meeting on Electrical Impedance Tomography*, pages 168–74, 1990.

[62] K. Boone, D. Barber, and B. Brown. Imaging with electricity: report of the european concerted action on impedance tomography. *Journal of Medical Engineering & Technology*, 2009.

[63] AOCCA Network and E Cherry. A second-generation current conveyor and its applications. *IEEE Transactions on Circuit Theory*, 1970.

[64] P. Eloranta and C. Toumazou. Current conveyors. *History, Theory, Applications and Implementation*, 4, 2004.

[65] S Natarajan. *Microelectronics analysis and design*. New Delhi: Tata McGraw-Hill, 2005.

[66] R. Bragos, J. Rosell, and P. Riu. A wide-band ac-coupled current source for electrical impedance tomography. *Physiological measurement*, 15(2A):A91, 1994.

[67] A. Kaewpoonsuk, V. Riewruja, A. Rerkratn, and T. Kamsri. An accurate ccii-based voltage controlled current source. In *International Conference on Control, Automation and Systems*, pages 1816–1819, 2008.

[68] I. Jivet and B. Dragoi. On-electrode autonomous current generator for multi-frequency eit. *Physiological measurement*, 29(6):S193, 2008.

[69] N. Terzopoulos, K. Hayatleh, B. Hart, F.J. Lidgey, and C. McLeod. A novel bipolar-drive circuit for medical applications. *Physiological measurement*, 26(5):N21, 2005.

[70] C.W. Denyer, F.J. Lidgey, Q.S. Zhu, and C.N. McLeod. High output impedance voltage controlled current source for bio-impedance instrumentation. In *Proceedings of the 15th Annual International Conference of the IEEE Engineering in Medicine and Biology Society*, pages 1026–1027, 1993.

[71] D. Sheingold. Impedance & admittance transformations using operational amplifiers. *The Lightning Empiricist*, 12(1):4, 1964.

[72] F. Seoane, R. Macias, R. Bragós, and K. Lindecrantz. Simple voltage-controlled current source for wideband electrical bioimpedance spectroscopy: circuit dependences and limitations. *Measurement Science and Technology*, 22(11):115801, 2011.

[73] P. Bertemes Filho. *Tissue characterisation using an impedance spectrosopy probe*. PhD thesis, University of Sheffield, 2002.

[74] H. Hong, M. Rahal, A. Demosthenous, and R.H. Bayford. Comparison of a new integrated current source with the modified howland circuit for eit applications. *Physiological measurement*, 30(10):999, 2009.

[75] D. Gómez Abad. *Development of a capacitive bioimpedance measurement system*. Universitat Politècnica de Catalunya, 2009.

[76] P. Bertemes-Filho, B.H. Brown, and A.J. Wilson. A comparison of modified howland circuits as current generators with current mirror type circuits. *Physiological Measurement*, 21(1):1, 2000.

[77] G.D. Hammond, C.C. Speake, and M. Stiff. Noise analysis of a howland current source. *International Journal of Electronics*, 95(4):351–359, 2008.

[78] D.X. Chen, X. Deng, and W.Q. Yang. Comparison of three current sources for single-electrode capacitance measurement. *Review of Scientific Instruments*, 81(3):034704, 2010.

[79] S. Franco. *Design with operational amplifiers and analog integrated circuits*. McGraw-Hill, 2001.

[80] K.S. Cheng, C.Y. Chen, M.W. Huang, and C.H. Chen. A multi-frequency current source for bioimpedance application. In *5th International IEEE Conference on Information Technology in Biomedicine*, 2006.

[81] S.M.M. Islam, M.A.R. Reza, and M.A. Kiber. Development of multi-frequency electrical impedance spectroscopy (eis) system for early detection of breast cancer. *International Journal of Electronics & Informatics*, 2013.

[82] D. Zhao. High output-impedance current source for electrical impedance tomography. In *4th International Conference on Biomedical Engineering and Informatics*, volume 2, pages 1106–1109, 2011.

[83] J.W. Lee, T.I. Oh, S.M. Paek, J.S. Lee, and E.J. Woo. Precision constant current source for electrical impedance tomography. In *Proceedings of the 25th Annual International Conference of the IEEE Engineering in Medicine and Biology Society*, volume 2, pages 1066–1069, 2003.

[84] I.M. Pandiev. Analysis and design of voltage-controlled current sources for a grounded load. *International Journal of Circuit Theory and Applications*, 43(6):756–775, 2015.

[85] J. Jossinet, C. Tourtel, and R. Jarry. Active current electrodes for in vivo electrical impedance tomography. *Physiological measurement*, 15(2A):A83, 1994.

[86] L. Zhangyong, X. Zhui, R. Chaoshi, W. Wei, Z. Dechun, and Z. Huiquan. Study of voltage control current source in electrical impedance tomography system. In *4th International Conference on Bioinformatics and Biomedical Engineering*, pages 1–4, 2010.

[87] M. Rafiei-Naeini and H. McCann. Low-noise current excitation sub-system for medical eit. *Physiological measurement*, 29(6):S173, 2008.

[88] J. Garcia Tabuenca. Multichannel bioimpedance measurement. Master's thesis, Tampere University of Technology, 2009.

[89] A.S. Tucker, R.M. Fox, and R.J. Sadleir. Biocompatible, high precision, wideband, improved howland current source with lead-lag compensation. *IEEE Transactions on Biomedical Circuits and Systems*, 7(1):63–70, 2013.

[90] L.T. Harrison. *Current Sources and Voltage References: A Design Reference for Electronics Engineers*. 2005.

[91] R.S. Radhakrishnan, K. Shah, H. Xue, S.D. Moore-Olufemi, F.A. Moore, N.W. Weisbrodt, S.J. Allen, B. Gill, and C.S. Cox. Measurement of intestinal edema using an impedance analyzer circuit. *Journal of Surgical Research*, 138(1):106–110, 2007.

[92] Z. Shuai, X. Guizhi, W. Huanli, G. Duyan, and Y. Weili. Multi-frequency eit hardware system based on dsp. In *28th IEEE Annual international conference*. Citeseer, 2006.

[93] M. Khalighi, B.V. Vahdat, M. Mortazavi, W. Hy, and M. Soleimani. Practical design of low-cost instrumentation for industrial electrical impedance tomography (eit). In *IEEE International Instrumentation and Measurement Technology Conference (I2MTC)*, pages 1259–1263, 2012.

[94] P. Pouliquen, J. Vogelstein, and R. Etienne-Cummings. Practical considerations for the use of a howland current source for neuro-stimulation. In *IEEE Biomedical Circuits and Systems Conference*, pages 33–36, 2008.

[95] J. Steele and T. Green. Proper compensation techniques will let the improved-howland and floating-load current sources perform up to par. *Electronic Design*, 1992.

[96] S.M.M. Islam, M.A.R. Reza, and M.A. Kiber. Performances of multi-frequency voltage to current converters for bioimpedance spectroscopy. *Bangladesh Journal of Medical Physics*, 5(1):71–76, 2013.

[97] W. Kester. *Practical design techniques for sensor signal conditioning*. Analog devices, 1999.

[98] A.S. Ross, G.J. Saulnier, J.C. Newell, and D. Isaacson. Current source design for electrical impedance tomography. *Physiological measurement*, 24(2):509, 2003.

[99] C. Schenk and U. Tietze. *Halbleiter-schaltungstechnik*. Springer, 1985.

[100] C. Gabriel, S. Gabriel, and E. Corthout. The dielectric properties of biological tissues: 1. literature survey phys. *Phy. Med. Biol.*, 41:2231–2249, 1996.

[101] D. Bouchaala, O. Kanoun, and N. Derbel. Portable bioimpedance spectrometer for total frequency range of β-dispersion. *tm–Technisches Messen*, 80(11):373–378, 2013.

[102] D. Bouchaala, A. Fendri, and O. Kanoun. Handheld bioimpedance spectrometer for the total frequency range of the e-dispersion. 2013.

[103] B. Sanchez, R. Bragos, and G. Vandersteen. Influence of the multisine excitation amplitude design for biomedical applications using impedance spectroscopy. In *Annual International Conference of the IEE Engineering in Medicine and Biology Society, EMBC*, pages 3975–3978, 2011.

[104] C. Pearson. High-speed, analog-to-digital converter basics. *Texas Instruments Application Report, SLAA510*, 2011.

[105] B.V. Venn. Estimation of the amplitude and phase of sinusoids. Available: http://allsignalprocessing.com/estimation-amplitude-phase-sinusoids, Accessed 09 02 2016.

[106] J. Ojarand, R. Land, and M. Min. Comparison of spectrally sparse excitation signals for fast bioimpedance spectroscopy: In the context of cytometry. In *IEEE International Symposium on Medical Measurements and Applications Proceedings (MeMeA)*, pages 1–5, 2012.

[107] U. Pliquett. Time-domain based impedance measurement: strengths and drawbacks. In *Journal of Physics: Conference Series*, volume 434, page 012092. IOP Publishing, 2013.

[108] P. Annus, M. Min, J. Ojarand, T. Paavle, R. Land, P. Ellervee, and T. Parve. Multisine and binary multifrequency waveforms in impedance spectrum measurementa comparative study. In *5th European Conference of the International Federation for Medical and Biological Engineering*, pages 1265–1268. Springer, 2011.

List of Figures

List of Tables

Publications list

- **Journal papers**

  1. **D. Bouchaala**, M. Guermazi, O. Kanoun, N. Derbel "Portable device design based on bioimpedance laboratory experiments for in-vitro biological tissue monitoring ", tm–Technisches Messen, volume 82, issue 10, pp. 485–494, October 2015

  2. **D. Bouchaala**, O. Kanoun, N. Derbel "High accurate and wideband current excitation for bioimpedance health monitoring systems", Measurement, August 2015

  3. **D. Bouchaala**, O. Kanoun, N. Derbel "Portable Bioimpedance Spectrometer for Total Frequency Range of ß-Dispersion", tm – Technisches Messen, volume 80, issue 11, pp. 373–378, ISSN (Online) 2196-7113, ISSN (Print) 0171-8096, November 2013

- **Conference papers**

  1. **D. Bouchaala**, A. Shrivastava, A. Fendri, M. Guermazi, O. Kanoun, N. Derbel " Specifications of mobile bioimpedance system for in-vitro Rectus Abdominus muscle characterization", 8th International Workshop on Impedance Spectroscopy, Chemnitz , Germany, 23-25 September 2015

  2. **D. Bouchaala**, E. Mekki, T. Guenther, P. Bueschel, O. Kanoun, N. Derbel "Study of Excitation Signals Parameters for Portable Biomedical Devices" IEEE International Instrumentation and Measurement Technology Conference, Pisa, Italy, 11-14 May 2015

  3. **D. Bouchaala**, M. Guermazi, O. Kanoun "Design of a portable device for in-vitro biological tissue diagnostic by impedance spectroscopy" IEEE Workshop Medizinische Messtechnik, Mülheim, Germany, 17 April 2015

  4. E. Mekki, **D. Bouchaala**, T. Guenther, P. Bueschel, O. Kanoun, N. Derbel " Study of the suitable excitation signal for portable impedance spectrometer", 7th International Workshop on Impedance Spectroscopy, Chemnitz , Germany, 24-26 September 2014

5. **D. Bouchaala**, O. Kanoun, N. Derbel " Minimization of Stray Capacitances in Howland Current Source ", 3rd IMEKO TC13 Symposium on Measurements in Biology and Medicine, Lecce , Italy, 17-18 April 2014

6. **D. Bouchaala**, A. Fendri, O. Kanoun "Handheld Bioimpedance Spectrometer for the Total Frequency Range of the beta-Dispersion", 16th International Conference on Sensors and Measurement Technology (SENSOR+TEST), Nürnberg , Germany, 14-16 May 2013

7. **D. Bouchaala**, Q. Shi, X. Chen, O. Kanoun, N. Derbel "Enhanced Howland Current Source for Medical Applications" the XV. International Conference on Electrical Bio-Impedance (ICEBI), Heiligenstadt, Germany, 22-25 April 2013

8. **D. Bouchaala**, A. Fendri, O. Kanoun "Portable Bioimpedance Measurement System for Medical Applications" IEEE Workshop Medizinische Messtechnik, Mülheim, Germany, 19 April 2013

9. **D. Bouchaala**, Q. Shi, X. Chen, O. Kanoun, N. Derbel "A High Accuracy Voltage Controlled Current Source for Handheld Bioimpedance Measurement", 10th international Multi-conference on systems, Signals and Devices (SSD), Hammamet, Tunisia, 18-21 March 2013

10. **D. Bouchaala**, Q. Shi, X. Chen, O. Kanoun, N. Derbel "Comparative study of voltage controlled current sources for biompedance measurements", 9th International Multi-conference on Systems, Signals and Devices (SSD), Chemnitz, Germany, March 2012

Thesen

- In order to fulfill the requirements for different bioimpedance applications in the medical field, an excitation signal in the frequency range covering the beta dispersion range should be provided by the measurement system.

- The use of a current excitation is very important to guaranty patient safety during bioimpedance measurement, even if the tissue impedance changes in a big range. This is because current range is critical for patient safety.

- Challenging features of high accurate voltage controlled current source are stable output current and high output impedance independently of the load changes in the whole *beta*-dispersion range.

- Current sources in "voltage mode approach" are more suitable than current sources in "current mode approach" for bioimpedance measurement with variable impedance values.

- Grounded load type is more safe for use in biomedical field and provides a better circuit's stability than the floating load type.

- Howland topology has the advantage of structure simplicity and some limitations because of its sensitivity to resistor mismatching.

- For a high quality of VCCS both circuit structure and component's choice are critical. The components should have with small tolerance and op-amps should fulfill a high common mode rejection ratio, low input bias current, low input offset voltage and wide bandwidth.

- By addition of gain compensation capacitors, the influence of stray capacitances can be compensated. The results show a good performance at high frequencies until 1 MHz.

- The influence of noise should be considered in the design of the measurement system in both electronic design and selection of excitation signals. This is because different signals show different sensitivity to noise.

- To consider the trade-off between the reconstructed signal's quality, the time consumption and hardware complexity, the signal's parameters which are the number of samples and the sampling rate should be optimized.

- Binary mutifrequency signals are suitable for bioimpedance spectroscopy due to the simplicity of generation, the low crest factor equal to one and the higher average power which is about 0.36 mW.